Porous carbon nanofibers containing silica-coated iron oxide nanoparticles by carbonisation of electrospun amphiphilic copolymer nanocomposites

by

Marthinus van Niekerk

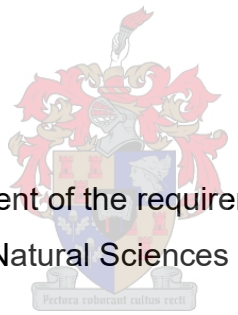

Thesis presented in partial fulfilment of the requirements for the degree of Master of Science in the Faculty of Natural Sciences at Stellenbosch University

Supervisor: Prof. P.E. Mallon

April 2019

Declaration

By submitting this thesis/dissertation electronically, I declare that the entirety of the work contained therein is my own, original work, that I am the sole author thereof (save to the extent explicitly otherwise stated), that reproduction and publication thereof by Stellenbosch University will not infringe any third party rights and that I have not previously in its entirety or in part submitted it for obtaining any qualification.

March 2019

Abstract

Amphiphilic PAN-g-PDMS copolymers were synthesized by conventional free radical polymerization of acrylonitrile monomer and PDMS macromonomer. Three chain lengths of PDMS macromonomer grafts were employed, each forming a series for which the monomer:macromonomer feed ratio was varied. SEC results showed a wide range of molar masses of the synthesized copolymers. This is to be expected given the uncontrolled nature of conventional free radical polymerization reactions. ^{1}H NMR measurements proved that a direct proportionality exists between the PDMS macromonomer feed and the incorporation thereof. Electrospinning of the synthesized PAN-g-PDMS copolymers from DMF was done at three different TCD's. In some cases, the fiber diameters could be explained by considering the PDMS graft content in conjunction with the molar mass, though in many cases the reasons for patterns in fiber diameters could not be clarified. A possible reason for this is that the expected phase segregation was, to some extent, inhibited by the method of solution preparation that entailed stirring at 50 °C for an hour followed by sonication for an hour. It is noteworthy that copolymers containing 5 kDa PDMS grafts showed severe gelation of the polymer solution. DSC analysis performed on the as-synthesized powders as well as on the electrospun fibers revealed that the current samples do not follow any clear trends w.r.t. PDMS graft content. When considering the cyclization exotherm which is a necessary process in order to convert the precursor fibers into carbon fibers, an interesting observation was made for the three series of copolymers containing 5 kDa grafts: as the PDMS graft content is increased a shoulder forms which ultimately separates into a double peak in the thermogram. This is presumably due to severe phase separation of domains rich in PAN homopolymer and domains rich in PDMS grafts undergoing the cyclization reaction at different temperatures. Co-precipitation of IONPs yielded nanoparticles with a diameter of 10.2 ± 2.4 nm as determined by TEM analysis. Silica coating of the IONPs initially produced multi-core nanoparticles with a diameter of 62.6 ± 12.5 nm containing 72.2 wt.% silica determined gravimetrically. The amount of TEOS added as reagent was decreased in order to form single-core nanoparticles of 22.2 ± 4.3 nm containing 29.6 wt.% silica and thus a thinner shell thickness. Thermal pre-treatment of single-core nanoparticles at 800 °C produced nanoparticles that appear very similar to untreated single-core nanoparticles. Electrospun fiber-particle nanocomposites showed nanoparticle agglomeration in the case of multi-core nanoparticles and good dispersion in the case of single-core nanoparticles and thermally treated single-core nanoparticles. Fiber-particle nanocomposites containing thermally treated single-core particles electrospun after 18 h of solution ageing showed some particle agglomeration. Carbonisation of the fiber-particle nanocomposites containing thermally treated nanoparticles produced intact carbon fiber-particle nanocomposites that showed very little fiber breakage. Sorption capacity measurements revealed hydrophilic behavior which was substantiated by the presence of an absorption peak associated with silica in the ATR-FTIR spectrum of the carbon fiber membrane.

Opsomming

Amfifiliese PAN-ent-PDMS kopolimere was gesintetiseer deur konvensionele vrye radikaal polimerisasie reaksies van akrilonitriel monomere en PDMS makromonomere. Drie ketting lengtes van PDMS makromonomeer ente was gebruik waarvan elk ‘n reeks vorm waarvoor die monomer:makromonomeer verhouding varieer was. SEC resultate het ‘n wye verskeidenheid van molêre massas van die gesintetiseerde kopolimere getoon. Hierdie resultaat is te verstaande, gegewe die onbeheerde natuur van konvensionele vrye radikaal polimerisasie reaksies. ^{1}H KMR metings het bewys dat ‘n direkte eweredigheid bestaan tussen die PDMS makromonomeer ente en die inkorporasie daarvan. Gesintetiseerde PAN-ent-PDMS kopolimere was ge-elektrospin vanaf DMF teen drie verskillende TCD’s. In sommige gevalle kon die vesel diameters verklaar word deur die PDMS ent inhoud tesame met die molêre massa te in ag te neem, alhoewel die vesel diameters in vele gevalle nie verklaar kon word nie. ‘n Moontlike rede hiervoor is dat die verwagte fase-segregasie tot ‘n mate inhibeer was deur die metode van voorbereiding van die oplossing wat roering teen 50 °C vir ‘n uur gevolg deur sonikasie vir ‘n uur behels. Dit is noemenswaardig dat kopolimere wat 5 kDa PDMS ente bevat hewige jellering van die polimeer oplossing getoon het. DSC analise wat op die voorbereide poeiers asook op die ge-elektrospinde vesels uitgevoer was, het gedui dat die huidige monsters geen duidelike tendens met betrekking tot PDMS ent inhoud het nie. Deur die sikliserings reaksie eksoterm, ‘n nodige proses om die voorloper vesels in koolstof vesels om te skakel, te analiseer was ‘n interessante observasie was gemaak vir die drie reekse van kopolimere bevattende 5 kDa ente: soos die PDMS ent inhoud vermeerder vorm ‘n skouer wat uiteindelik skei en ‘n dubbel-piek in die termogram vorm. Dit is vermoedelik die gevolg van hewige fase-segregasie van domeine ryk in PAN homopolimeer en domeine ryk in PDMS entpolimere wat die sikliserings reaksie by verskillende temperature ondergaan. Ko-presipitasie van IONPs het nanoparticles met ‘n diameter van 10.2 ± 2.4 nm gelewer soos bepaal deur TEM analise. Silika bedekking van die IONPs het aanvanklik multi-kern nanopartikels met ‘n diameter van 62.6 ± 12.5 nm en ‘n silica inhoud van 72.2 wt.%, gravimetries bepaal, geproduseer. Die aantal TEOS bygevoeg as reagent was verminder om sodoende enkel-kern nanopartikels van 22.2 ± 4.3 nm bevattende 29.6 wt.% silika, en dus ‘n dunner omhulsel, te produseer. Termiese voor-behandeling van die enkel-kern nanopartikels teen 800 °C het nanopartikels gelewer wat baie eenders voorkom as die onbehandelde enkel-kern nanopartikels. Geëlektrospinde vesel-partikel nanokomposiete het nanopartikel agglomerasie getoon in die geval van die multi-kern nanoparticles en goeie verspreiding in die geval van die enkel-kern nanopartikels en die termies voor-behandelde enkel-kern nanopartikels. Vesel-partikel nanokomposiete bevattende termies behandelde enkel-kern partikels ge-elektrospin na 18 h van oplossingsveroudering het weinig partikel agglomerasie getoon. Verkoling van die vesel-partikel nanokomposiete bevattende termies behandelde nanopartikels het ongeskonde koolstof vesel-partikel nanokomposiete gelewer wat baie min vesel verbreking getoon het. Metings van sorbsie kapasiteit het hidrofiliese gedrag ontbloot wat gestaaf was deur die teenwoordigheid van ‘n absorpsie piek geassosieer met silika in die ATR-FTIR spektrum van die koolstof vesel membraan.

Acknowledgements

The author would like to express his sincere gratitude to the following persons or entities for their contribution to this project:

Prof. P.E. Mallon for guidance, patience and insight

The Physical Group of Lab 1006

Students and staff of the Chemistry and Polymer Science Department for constant willingness to be of help when needed

Sasol for funding

Mohamed Jaffer for assistance with TEM analysis

Madeleine Fraserburg for assistance with SEM analysis

My parents for their unfailing financial support, time and effort invested in me throughout the course of my studies

Table of Contents

Table of Contents

Table of Contents

List of figures

Chapter 2

List of tables

Chapter 4

List of schemes

Chapter 3

Glossary

List of abbreviations

ATR-FTIR	Attenuated Total Reflectance Fourier Transform Infrared Spectroscopy
AIBN	2,2'-Azobisisobutyronitrile
AN	Acrylonitrile
ATRP	Atom Transfer Radical Polymerization
a.u.	Arbitrary units
BuOH	1-butanol
Chloroform-*d*	Deuterated chloroform
DLS	Dynamic Light Scattering
DMF	N,N-Dimethylformamide
DMSO	Dimethyl sulfoxide
DMSO-d_6	Deuterated dimethyl sulfoxide
DSC	Differential Scanning Calorimetry
EtOH	Ethanol
FTIR	Fourier Transform Infrared Spectroscopy
g/g, $g.g^{-1}$	Gram per gram
GO	Graphene oxide
^{1}H NMR	Proton Nuclear Magnetic Resonance
HPLC	High-Performance Liquid Chromatography
IONPs	Iron oxide nanoparticles
LCST	Lower Critical Solution Temperature
M_n	Number average molar mass
MEHQ	Monomethyl ether hydroquinone
MCH	Cyclohexane
MW	Molecular weight
MWCNT	Multi-walled carbon nanotubes
NPs	Nanoparticles
SANS	Small Angle Neutron Scattering
SEC	Size Exclusion Chromatography
SEM	Scanning Electron Microscope
TCD	Tip-to-collector distance
TEM	Transmission Electron Microscope
TEOS	Tetraethyl orthosilicate
PAN	Poly(acrylonitrile)
PAN-*co*-PyMMP	Poly(acrylonitrile)-*co*-(*1*-pyrene)methyl-*2*-methyl-*2*-propenoate

PAN-g-PDMS	Poly(acrylonitrile)-*graft*-poly(dimethylsiloxane)
PBA	Poly(*n*-butyl acrylate)
PBA-*b*-PS	Poly(*n*-butyl acrylate)-*block*-polystyrene
PDMAA	Poly(N,N'-dimethyl acrylamide)
PDMS	Poly(dimethylsiloxane)
PEO	Poly(ethylene glycol)
PHEMA	Poly(2-hydroxyethyl methacrylate)
PNIPAM	Poly(N-isopropylacrylamide)
PS	Polystyrene
PVP	Poly(vinylpyrrolidone)
TGA	Thermal Gravimetric Analysis
THF	Tetrahydrofuran
wt.%	Weight percentage
WAXD	Wide-Angle X-ray Diffraction
XRD	X-ray Diffraction

Introduction and Objectives

The motivation for the current study is stated along with a brief introduction to the relevant processes used. The objectives of the study are stated.

1.1. Introduction

Carbon nanofibers have proven to be highly versatile, finding use in various applications such as semi-conductors, capacitors and load-bearing devices.[1,2,3] Their high mechanical strength and excellent thermal and electrical conductivities have attracted great research interest.[4] It has been demonstrated that carbon nanofiber sponges and carbon nanofiber membranes have a high sorption capacity toward oils and can be used to selectively remove oil from water.[5,6]

Porous carbon nanofibers, having hydrophobic and oleophilic properties, have proven to be capable of selectively removing organic pollutants from water.[6] Online methods of use can be developed if such a sorbent could be added to a wastewater line and removed via a permanent magnet. Iron oxide nanoparticles, being easily synthesized and well-researched, are prime candidates for inducing magnetism.[7,8,9,10,11,12,13] The goal of the current study is to produce a porous magnetic carbon nanofiber membrane by carbonization of electrospun, porous magnetic nanofiber-nanoparticle precursor composites.

Synthesis of amphiphilic PAN-g-PDMS copolymers by a conventional free radical polymerization of acrylonitrile monomer and PDMS macromonomer in a suitable solvent with the use of a thermal initiator have been reported.[6,14,15,16] When the copolymers are dissolved in DMF, solution phase separation takes place in order to minimize unfavourable interactions between the hydrophobic PDMS sections and the solvent as well as maximize favourable interactions between the hydrophilic PAN sections and the solvent.[6,15,16]

Upon electrospinning, the mentioned phase separation is transferred to the fibers in the form of a porous surface morphology.[6,16] Porosity of the fibers increases the surface area and thereby enhances any surface interactions with the environment. Solution phase separation is a time-dependent process whereby the surface roughness of the electrospun nanofibers increases with increasing solution ageing time.[6] Therefore, it is beneficial to allow the polymer solution to age before electrospinning ensues.

Carbonisation of electrospun nanofiber precursors can be carried out by following a suitable thermal program. At temperatures of 200-300 °C under oxidizing conditions, nitrile pendant groups on the PAN sections of polymer chains undergo a cyclization reaction to form ladder-type structures.[17,18] This is the stabilization process. Further heating of the fibers in an inert atmosphere is carried out to produce carbon fibers.[17,18] Even though PAN sections are involved in the mentioned process of carbonization, various PAN-based copolymers that do not restrain the stabilization process have successfully been synthesized.[19,20] PAN-g-PDMS copolymers is such a class of copolymers.[6,16] Porous carbon nanofibers, produced by carbonization of the mentioned electrospun PAN-g-PDMS

porous nanofiber precursors, have shown excellent sorption capacity of various oils and solvents as well as a very low sorption capacity of water.[5,6]

Iron oxide nanoparticles can be synthesized using a range of possible methods of which the simplest is the co-precipitation method.[8] Co-precipitation of iron precursors is a quick and low-cost synthetic method yielding magnetic nanoparticles.[7,8,9,11,12,13] Hydroxyl groups on the surfaces of synthesized IONPs make surface functionalization possible. In the current study, surface functionalization is a necessity due to unfavorable reactions between the surfaces of IONPs and the carbon matrix during carbonization that leads to the release of oxygen through the formation of iron carbide.[21] A well-established and simple method of surface functionalization entails the formation of a silica shell of controllable thickness around the IONPs.[8,9,22,23,24] Silica provides a barrier between the encompassed IONP and the surrounding carbon matrix. Dispersion of the nanoparticles is not trivial. Attractive Van der Waals forces and repulsive electrostatic surface potential are in competition to induce either agglomeration or dispersion of the nanoparticles.[25] In addition to providing a barrier between IONPs and the surrounding carbon matrix, the encompassing silica shell will also provide a surface with a stable electrostatic potential. Therefore, the silica coating provides stability to IONPs and prevents agglomeration.[8]

Incorporation of nanoparticles into nanofibers can be achieved by co-electrospinning, i.e.: adding nanoparticles to the electrospinning solution. Since the nanoparticles will be present in the electrospinning solution of which the solvent evaporates in order to form fibers, the nanoparticles become incorporated into the nanofibers.

Carbonization of the fiber-particle nanocomposite precursors to yield a porous magnetic carbon nanofiber membrane is the final step in obtaining the intended product. Oxygen release from the iron oxide cores at high temperatures is a major concern. Silica shells around IONPs have been proven to be permeable to acids.[24] Therefore it is implausible that the silica shells will be impermeable to oxygen gas emitted from the iron oxide cores of nanoparticles. At the high temperatures employed during carbonization, carbon material surrounding the nanoparticles will be oxidized and form gaseous decomposition products such as carbon monoxide and carbon dioxide. Even though nanoparticle agglomerates, if present, may not affect the total magnetization of the fiber-particle nanocomposites, fiber breakage might become more prevalent either due to stress induced by shrinkage of the nanofibers or by oxygen released by the iron oxide cores. This is to be avoided due to decreased structural integrity of the fiber membrane brought about by fiber breakage and loss of magnetic nanoparticles.

The intended final product, porous magnetic carbon nanofibers, contains magnetic nanoparticles incorporated into porous carbon nanofibers.

1.2. Objectives

The specific objectives of the current study are summarised below.

1. Synthesis of various series of PAN-g-PDMS copolymers utilizing different molecular weights of PDMS macromonomers and by varying the feed ratio for each series. The synthesised copolymers will be analysed to identify any trends w.r.t. molar mass, PDMS macromonomer incorporation and gravimetric yield.

2. Electrospinning of the synthesised copolymers. Investigation of the effects of PDMS graft incorporation as well as TCD on the fiber diameter will be conducted.

3. Investigation of the effects of electrospinning solution ageing on the resultant fiber morphology.

4. Thermal analysis on the as-synthesised powders and electrospun nanofibers. The effects of PDMS graft incorporation on the exothermic cyclization reaction, a crucial step in the carbonization procedure, will be studied.

5. Carbonisation of the electrospun nanofibers and analysis of the carbon nanofibers to observe changes in surface morphology and fiber diameter.

6. Synthesis of IONPs by means of co-precipitation.

7. Silica coating of IONPs employing a procedure based on that developed by Stöber.[26] The process requires optimization to yield a thin silica shell to obtain nanoparticles containing a high percentage of magnetic iron oxide.

8. Electrospinning of fiber-particle nanocomposites. Nanoparticle agglomeration will be investigated.

9. Carbonisation of fiber-particle nanocomposites. Fiber breakage around incorporated nanoparticles is of concern.

10. Evaluation of the sorption capacity of the resultant carbon fiber membrane.

References

1. Jost, K. *et al.* Knitted and screen printed carbon-fiber supercapacitors for applications in wearable electronics. *Energy Environ. Sci.* **6**, 2698–2705 (2013).
2. Karaipekli, A., Sari, A. & Kaygusuz, K. Thermal conductivity improvement of stearic acid using expanded graphite and carbon fiber for energy storage applications. *Renew. Energy* **32**, 2201–2210 (2007).
3. Luo, H. *et al.* Preparation of three-dimensional braided carbon fiber-reinforced PEEK composites for potential load-bearing bone fixations. Part I. Mechanical properties and cytocompatibility. *J. Mech. Behav. Biomed. Mater.* **29**, 103–113 (2014).
4. Zhu, J. *et al.* Magnetic polyacrylonitrile-Fe@FeO nanocomposite fibers - Electrospinning, stabilization and carbonization. *Polymer (Guildf).* **52**, 2947–2955 (2011).
5. Tai, M. H., Tan, B. Y. L., Juay, J., Sun, D. D. & Leckie, J. O. A Self-Assembled Superhydrophobic Electrospun Carbon-Silica Nanofiber Sponge for Selective Removal and Recovery of Oils and Organic Solvents. *Chem. - A Eur. J.* **21**, 5395–5402 (2015).
6. Human, C. Facile method for producing silicon containing porous carbon nanofibres from amphiphilic copolymers and controlling precursor fibre morphology, MSc Thesis. (Stellenbosch University, 2015).
7. Massart, R. Preparation of Aqueous Magnetic Liquids in Alkaline and Acidic Media. *IEEE Trans. Magn.* **17**, 1247–1248 (1981).
8. Wu, W., He, Q. & Jiang, C. Magnetic Iron Oxide Nanoparticles: Synthesis and Surface Functionalization Strategies. *Nanoscale Res. Lett.* **3**, 397–415 (2008).
9. Lakay, E. M. Superparamagnetic iron-oxide based nanoparticles for the separation and recovery of precious metals from solution, MSc Thesis. (Stellenbosch University, 2009).
10. Fortuin, L. Modified chitosan nano-substrates for mycobacterial capture, MSc Thesis. (Stellenbosch University, 2015).
11. Bumb, A. *et al.* Synthesis and characterization of ultra-small superparamagnetic iron oxide nanoparticles thinly coated with silica. *Nanotechnology* **19**, 335601 (2008).
12. Kim, D. K., Zhang, Y., Voit, W., Rao, K. V. & Muhammed, M. Synthesis and characterization of surfactant-coated superparamagnetic monodispersed iron oxide nanoparticles. *J. Magn. Magn. Mater.* **225**, 30–36 (2001).
13. Sun, Y., Ma, M., Zhang, Y. & Gu, N. Synthesis of nanometer-size maghemite particles from magnetite. *Colloids Surfaces A Physicochem. Eng. Asp.* **245**, 15–19 (2004).
14. Bayley, G. M., Hedenqvist, M. & Mallon, P. E. Large strain and toughness enhancement of poly(dimethyl siloxane) composite films filled with electrospun polyacrylonitrile-graft-poly(dimethyl siloxane) fibres and multi-walled carbon nanotubes. *Polym. (United Kingdom)* **52**, 4061–4072 (2011).

15. Basson, N. Free volume of electrospun organic-inorganic copolymers, MSc Thesis. (Stellenbosch University, 2014).
16. Bayley, G. M. & Mallon, P. E. Porous microfibers by the electrospinning of amphiphilic graft copolymer solutions with multi-walled carbon nanotubes. *Polym. (United Kingdom)* **53**, 5523–5539 (2012).
17. Fitzer, E. *et al. Ullmann's Encyclopeida of Industrial Chemistry*. (Wiley-VCH Verlag GmbH & Co. KGaA, 2011).
18. Avilés, M. A. *et al.* Thermal analysis of acrylonitrile polymerization and cyclization in the presence of N,N-dimethylformamide. *J. Therm. Anal. Calorim.* **67**, 177–188 (2002).
19. Catta Preta, I. F. *et al.* Thermal behavior of polyacrylonitrile polymers synthesized under different conditions and comonomer compositions. *J. Therm. Anal. Calorim.* **87**, 657–659 (2007).
20. Jamil, S. N. A., Daik, R. & Ahmad, I. Redox Synthesis and Thermal Behavior of Acrylonitrile-Methyl Acrylate-Fumaronitrile Terpolymer as Precursor for Carbon Fiber. *Int. J. Chem. Eng. Appl.* **3**, 416–420 (2012).
21. Wojcik, M., Chmist, J., Przewoznik, J., Figiel, H. & Blazewicz, S. Magnetic properties of PAN-based carbon fibres modified with magnetite nanoparticles. *Carbon N. Y.* **50**, 1604–1613 (2012).
22. Tadyszak, K. *et al.* Spectroscopic and magnetic studies of highly dispersible superparamagnetic silica coated magnetite nanoparticles. *J. Magn. Magn. Mater.* **433**, 254–261 (2017).
23. Deng, Y. H., Wang, C., Hu, J., Yang, W. & Fu, S. Investigation of formation of silica-coated magnetite nanoparticles via sol-gel approach. *Colloids Surfaces A Physicochem. Eng. Asp.* **262**, 87–93 (2005).
24. Vatta, L. L., Kramer, J. & Koch, K. R. Diethylenetriamine Functionalized Silica Coated Magnetite Nanoparticles for Selective Palladium Ion Extraction from Aqueous Solutions. *Sep. Sci. Technol.* **42**, 1985–2002 (2007).
25. Verwey, E. J. W. Theory of the stability of lyophobic colloids. *J. Phys. Colloid Chem.* **51**, 631–636 (1947).
26. Stöber, W., Fink, A. & Bohn, E. Controlled Growth of Monodisperse Silica Spheres in the Micron Size Range. *J. Colloid Interface Sci.* **26**, 62–69 (1968).

Historical and Literature Overview

An overview of the literature reported relevant to the current study is given.

2.1 Oleophilic carbon nanofiber membranes

It has been demonstrated that porous carbon nanofibers can be used for purification of water by extraction of various oils and organic solvents.[1] This unique property is due to the highly oleophilic and hydrophobic nature of carbon nanofibers, as is evident from *Figure 2.1*. A porous morphology can be induced by electrospinning of phase separated polymer solutions of PAN-g-PDMS copolymers from DMF.[1,2] The amphiphilic nature of the copolymers leads to solution morphologies that are transferred into the solid state nanofibers during evaporation of the solvent inherent in the electrospinning process. Carbon nanofibers formed by the carbonization of the aforementioned porous nanofiber precursors were proven to have significantly higher surface areas than their PAN homopolymer nanofiber precursor counterparts.[1] Increasing the PDMS content leads to an increased hydrophobicity as demonstrated by the greater surface contact angle measured when placing a drop of water on a carbon nanofiber mat as in *Figure 2.1*.[1]

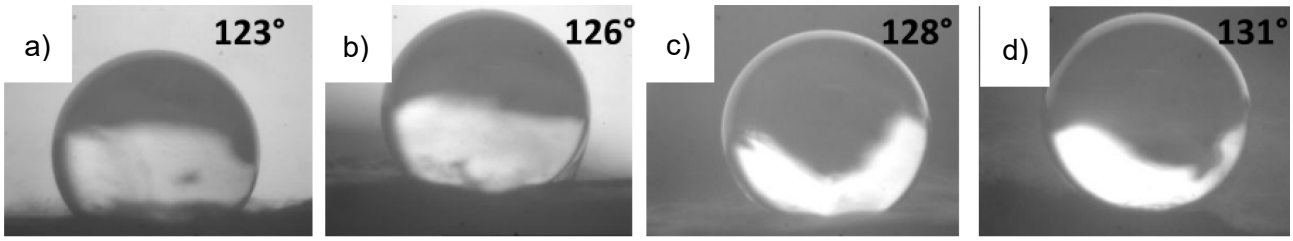

Figure 2.1: Digital images of surface contact angle measurements of a water droplet on a carbon nanofiber mat produced from a) PAN precursor nanofibers and PAN-g-PDMS precursor nanofibers containing b) 12.1 wt.% PDMS grafts, 15.7 wt.% PDMS grafts and 18.3 wt.% PDMS grafts [1]

This result is due to the change in surface chemistry, surface roughness and fiber density and should not be taken as an absolute measurement if these parameters vary between samples.[1] *Figure 2.2* shows the sorption capacity towards various substances as well as recyclability of the fiber membrane. The porous carbon nanofiber mats have shown high sorption capacities towards oils such as silicon oil, mineral oil and olive oil with a sorption capacity of more than 48 $g.g^{-1}$ for olive oil.[1]

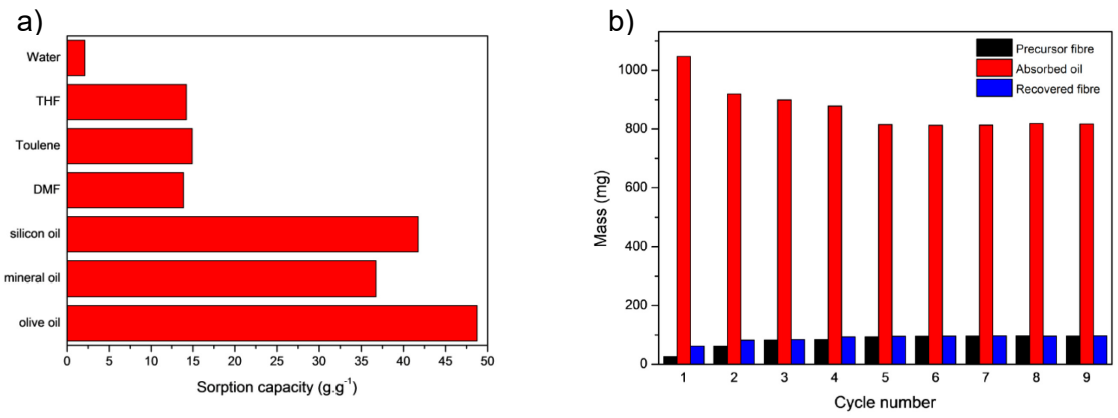

Figure 2.2: a) Sorption capacity on a mass/mass basis of porous carbon nanofibers for various liquids and b) its recyclability over nine cycles of use [1]

This result is, however, dependent on the densities and viscosities of the tested solvents and oils.[1] The high sorption capacity of the porous carbon nanofibers is due to their highly oleophilic nature and a porous structure that can induce capillary action.[1] Lesser sorption capacities are shown for THF, DMF and toluene with a sorption capacity between 10 and 15 $g.g^{-1}$.[1] A sorption capacity of about 2 $g.g^{-1}$ was shown towards water.[1] The low sorption capacity towards water is an important property of the membranes; a high sorption capacity towards water will lead to saturation of the membrane and possibly decrease the sorption capacity towards oils.

Carbon-silica sponges, shown in *Figure 2.3*, are essentially the product of the upscaling of a process that produces carbon-silica membranes.[3] Tai *et al*. reported the synthetic procedure which entails the electrospinning of PAN, TEOS and acetic acid from DMF in a nitrogen atmosphere followed by stabilization in air at 280 °C for 2 h and subsequent carbonization in nitrogen at 900 °C.[3] A nitrogen atmosphere was required for electrospinning due to the rapidly hydrolyzed spinning solution.[3] In terms of DMF absorption, the carbon-silica sponge had superior capacity to that of the carbon-silica membrane, at 64.9 $g.g^{-1}$ and 11.6 $g.g^{-1}$ respectively.[3] Both Human and Tai *et al*. reported a mirror-reflection on the surface of the carbon-silica membranes and carbon-silica sponges, respectively, due to air trapped between the superhydrophobic surface and the surrounding water.[1,3] Tai *et al*. summarized the requirements for an adsorbent to meet the practical demand for selectivity, recyclability, uptake rate and sorption capacity as follows:

- Superhydrophobicity and superoleophilicity
- Mechanical stability under deformation
- High porosity
- High oil uptake amount.

Figure 2.3: a) Water droplets on a carbon-silica sponge with inset of a surface contact angle measurement and b) carbon-silica sponge immersed in water showing mirror reflection caused by its hydrophobicity [3]

Polyacrylonitrile (PAN) is a commonly used as a precursor material for the production of carbon materials and, specifically, carbon nanofibers.[1,4,5] The carbonization process will be discussed in the section *2.12 Carbonisation*, but since in the current project PAN-based graft copolymers are used as the precursor material, a brief review of copolymers and other relevant aspects of these materials is first provided.

2.2 Polymer solution phase separation

Homopolymers, of which each inserted monomer unit is identical, have singular chemical constituents. Copolymers, in contrast, have at least two unique monomer units inserted into the synthesized polymer product. Though synthesis of copolymers with very distinctive monomer constituents can be challenging, it is possible to synthesise copolymers containing monomer units with entirely different solubilities. The simplest copolymer to consider is a diblock copolymer: generally a homopolymer section, consisting of the first monomer, is synthesized with a reactive end-group from which another section of polymer, consisting of the second monomer, is polymerized. Diblock copolymers have been extensively researched due to their wide applications.[6] Amphiphilic block copolymers consist of two blocks that are incompatible and interact with the environment in very different ways.[6] In a selective solvent, one of the blocks will be soluble and be oriented towards the solvent medium.[6] The insoluble block will be shielded from the medium.[6] Micellization can occur in this manner with the soluble block forming the 'corona' and the insoluble block forming the 'core' of the micelle.[6] Micelles are, however, merely the simplest structures that can be formed by phase separation of block copolymers; many other morphologies are possible. The morphology can be tweaked by changing the environment containing the diblock copolymers to procure other morphologies such as vesicles, inverse micelles, lamellar structures and tubular micelles.[6] The synthesis of amphiphilic diblock copolymers are, however, challenging: addition of the second block is not always a trivial endeavour. Among other copolymer architectures that can be used for phase separation is graft copolymers. Though controlled synthesis of graft copolymers forming predetermined chain structures is possible, this type of synthesis is not as simple as conventional free radical copolymerization.[7] Graft copolymers with a low grafting density of evenly spaced grafts with low molar mass have been shown to assume micellar morphologies according to solubility of either the backbone or grafts with the backbone and grafts.[8]

2.3 Conventional free radical copolymerization

In a conventional free radical copolymerization reaction employing the *grafting through* technique, a random graft copolymer will be synthesized.[1,2,9,10,11] Such a polymer architecture, when subjected to the appropriate environment, will undergo phase separation leading to a range of morphologies. Differences between synthesized polymer chains arise from the uncontrolled nature of conventional free radical polymerization. A range of morphologies assumed by phase separated copolymers can be found in the same solution due to the unique nature of each synthesized polymer. Differences in reactivity of the constituent monomers can lead to compositional drift that might, if the extent is sufficient, lead to a block-type copolymer or even the formation of homopolymers.[2,9,11] As mentioned, *grafting through* is the simplest technique to when synthesizing graft copolymers.

2.3.1 Grafting through

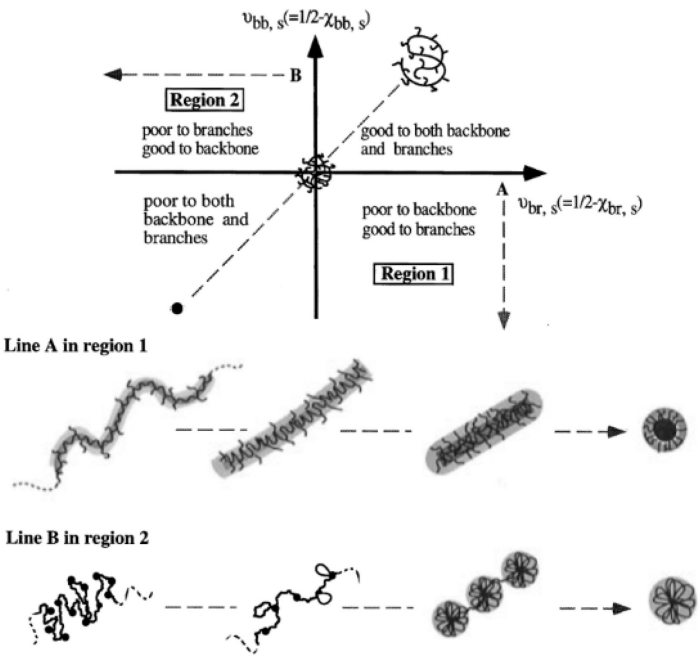

Figure 2.4: Schematic of morphologies achievable by graft copolymers with evenly spaced grafts of low grafting density and low molar mass [6]

*Figure 2.*4 shows different solution morphologies that can be assumed by graft copolymers in solution. In addition to using low molar mass monomers, high molar mass macromonomers are used in a *grafting through* copolymerization reaction.[1,2,9,10,11] During this technique, a macromonomer fulfils a similar role to that of a low molar mass monomer. Functional macromonomers can be polymers themselves. As in the case of low molar mass monomers, macromonomers require a reactive group to be used in free radical polymerization reactions. Generally a double bond will be at the chain-end of the macromonomer due to the ease of synthesizing polymers with functional chain-ends as opposed to the difficulties of synthesizing polymers with mid-chain functionalities. Both monomers are bound to undergo the same chain insertion reactions while a large difference in reactivity ratios will lead to the formation of homopolymers.[11]

2.3.2 Grafting from

If a functional group is used as an initiation site for polymerization, *grafting from* the said reactive site takes place. Song *et al*. designed and synthesized a grafted copolymer with thermo-responsive side-chains by performing a controlled polymerization from reactive pendant groups on the precursor polymer backbone, as seen in *Figure 2.5*.[7] Micelles formed using these polymers had a narrow size distribution; an expected result considering the controlled nature of the synthetic procedure used to form the constituent polymers.[7] Micelles formed using these polymers show promising results in terms of biocompatibility and cellular uptake and are therefore suitable for controlled drug delivery applications.[7]

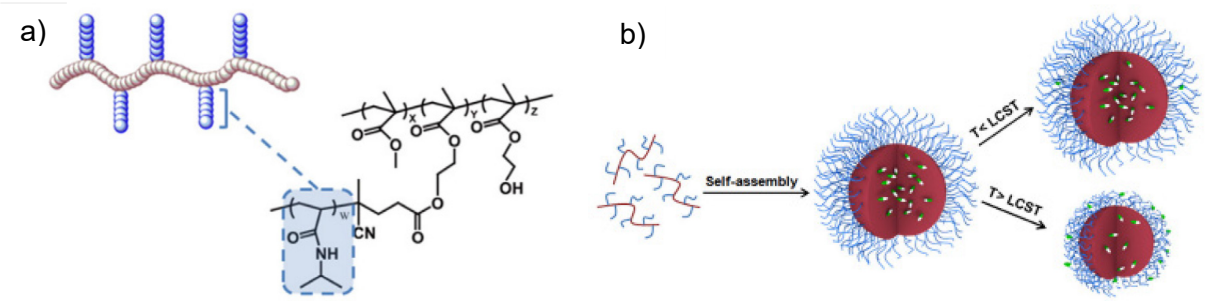

Figure 2.5: a) Model and structure of thermo-responsive polymer containing PNIPAM grafts and b) schematic self-assembly of synthesized polymers depicting guest release when passing through LCST [7]

The initiation site does not need to be attached to a polymer. Siebert has demonstrated the use of 1-pyrenemethanol and 1-pyrenebutanol as initiation sites for a cerium initiated polymerization.[12] The reaction scheme and demonstration of the dispersability effects are seen in *Figure 2.6*. The synthesised end-functionalized PAN polymers were used to disperse MWCNTs in DMF by taking advantage of pi-stacking interactions between the surfaces of the MWCNTs and the pyrene-terminated soluble polymers.[12] It was also demonstrated that dispersion can be achieved by using PAN-based copolymers containing comonomers with pyrene pendant groups synthesized using the grafting through method.[12]

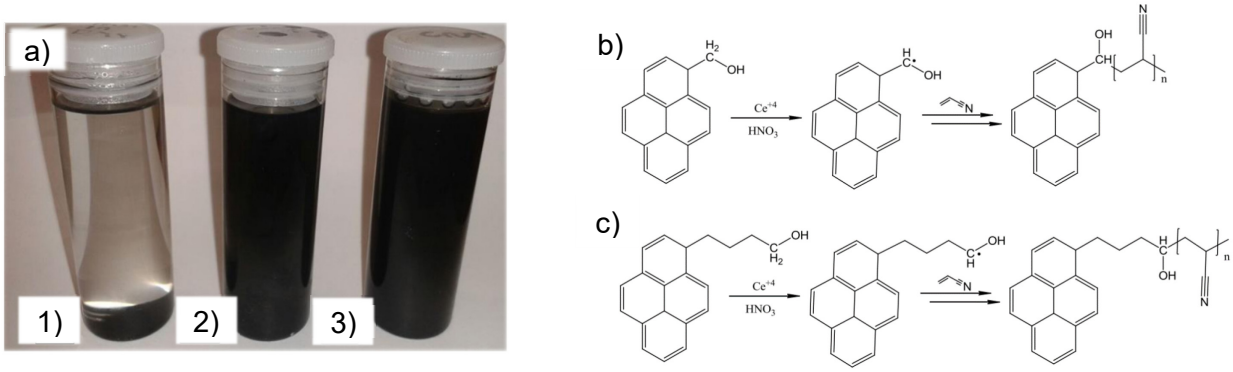

Figure 2.6: a) Demonstration of dispersability of 1) nascent MWCNTs, 2) MWCNTs functionalized with PAN-co-PyMMP and 3) MWCNTs functionalized with Py-PAN in DMF with accompanying reaction schemes of cerium initiated polymerizations from b) 1-pyrenemethanol and c) 1-pyrenebutanol [12]

Ma *et al*. have demonstrated that a cerium initiated PAN polymerization can be performed from the surface of graphene oxide to enhance dispersability in DMF, as shown in the schematic in *Figure 2.7*. Using XRD, it was proved that a high grafting ratio of PAN polymer will lead to an exfoliated structure confirmed by the absence of a graphite peak in the diffraction pattern.[13] The proposed reaction is shown in *Figure 2.7.c*.

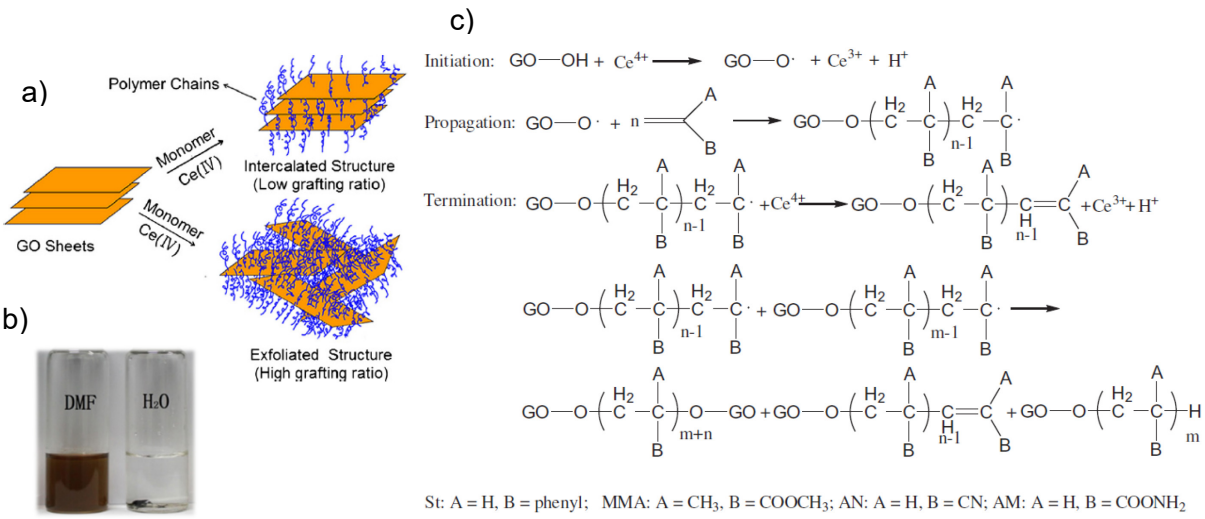

Figure 2.7: a) Schematic illustration of dispersion of graphene oxide sheets grafted with polymers, b) demonstration of dispersability of exfoliated graphene grafted with PAN polymers in DMF and water and c) proposed reaction scheme of cerium initiated polymerization from graphene oxide (GO) [13]

2.3.3 Grafting onto

This method is a post-polymerization method that entails the process of attaching a synthesized polymer to a functional group. Gao *et al*. employed a "click" reaction, shown in *Figure 2.8*, between the pendant groups of a PHEMA-alkyne and azido-terminated polymers, both synthesized by ATRP.[14]

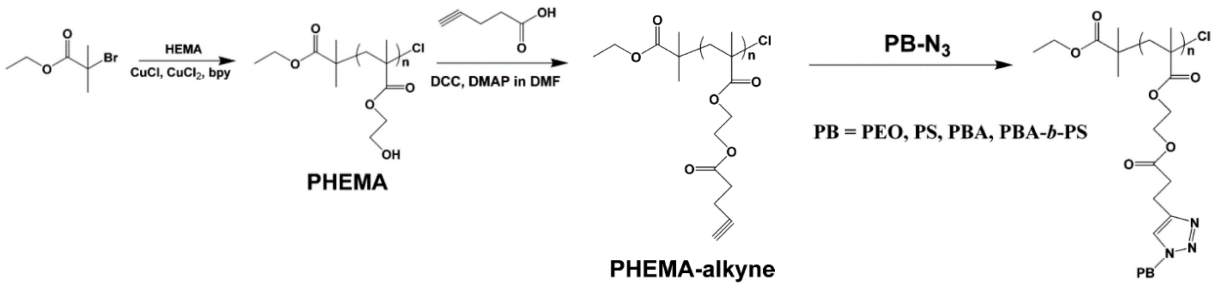

Figure 2.8: Reaction scheme for the synthesis of polymer grafted PHEMA where both the backbone and the polymer grafts were synthesized by controlled polymerization reactions [14]

Lien *et al*. demonstrated the grafting of thermo-responsive NIPAM-based polymers onto the surface of silica-coated IONPs, which is schematically shown in *Figure 2.9*. 3-(trimethoxysilyl)propyl methacrylate was used as a comonomer as to carry out a post-polymerization reaction to covalently attach the polymers to the surface of silica-coated IONPs by means of hydrolysis of the methoxy groups.[15]

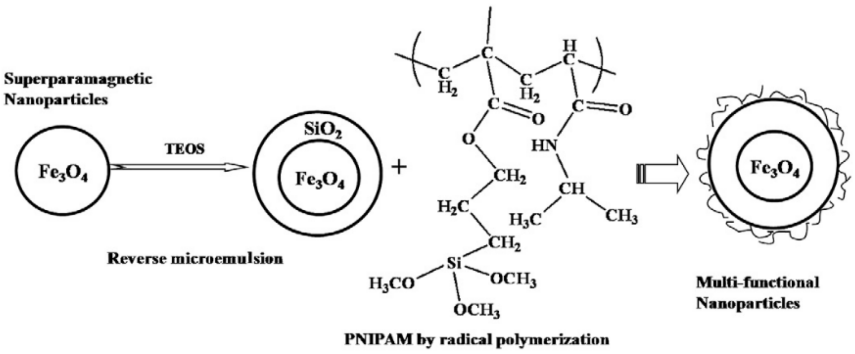

Figure 2.9: Schematic representation of grafting of PNIPAM-based polymers onto silica-coated IONPs [15]

2.4 Copolymer composition of PAN-g-PDMS copolymers

The reaction scheme for conventional free radical copolymerization of acrylonitrile and PDMS graft macromonomers is shown in *Figure 2.10*. This reaction generally leads to a mixture of PAN homopolymer and PAN-g-PDMS copolymers of which the copolymer content is proportional to the monomer feed ratio as proved by chromatographic methods.[2] From the mentioned chromatographic studies it is clear that a higher feed of the PDMS macromonomer will decrease the amount of PAN homopolymer formed in the reaction for 1 kDa and 5 kDa PDMS graft macromonomers used.[2]

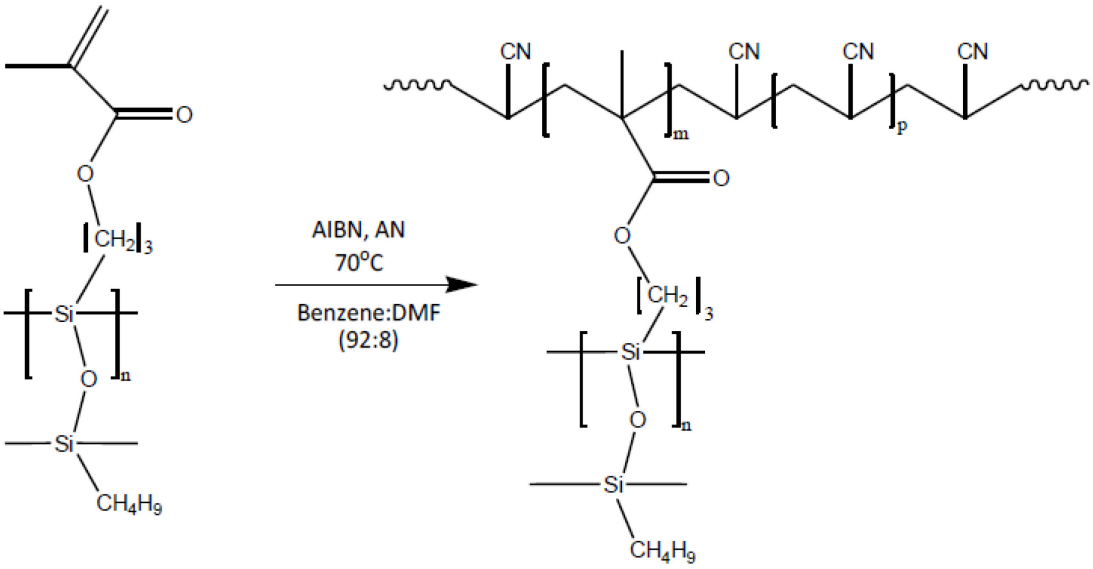

Figure 2.10: Reaction scheme of PAN-g-PDMS copolymerization initiated by thermal initiation of AIBN in a solvent mixture of benzene and DMF at 70 °C [2]

By means of *in* situ H^1 NMR, Wagenaar found that a difference in reactivity ratio, caused by more effective stabilization of a radical on a tertiary carbon as opposed to a secondary carbon, led to poly(N,N'-dimethyl acrylamide) (PDMAA) homopolymerization in a PDMAA-g-PDMS copolymerization reaction after depletion of the more reactive PDMS macromonomers.[11] By using gradient elution chromatography, it was found that a lower PDMS feed led to a larger amount of PDMAA homopolymer being formed.[11] This was ascribed to the slow diffusion rate of the residual

macromonomer during homopolymerization of the monomer of which the effects are offset by a higher feed ratio of PDMS macromonomer.[11] Clearly an observable compositional drift takes place.

In the proposed PAN-g-PDMS copolymerization reaction as depicted in *Figure 2.10*, there are two possible routes leading to the formation of PAN homopolymers of which the presence is proved by HPLC in *Figure 2.11*. The first possibility is that the PDMS macromonomer, as in the case of PDMAA-g-PDMS copolymerization, has a higher reactivity ratio than the AN monomer due to better stabilization of the radical. This will lead to rapid polymerization and consequent depletion of the PDMS macromonomers and thereby cause compositional drift which will, if sufficiently severe, possibly bring about the formation of PAN homopolymers. The second possibility is that the PDMS macromonomer, in contrast to the case of PDMAA-g-PDMS copolymerization, has a lower reactivity ratio than the AN monomer due to limited solubility in the solvent mixture used. This will lead to delayed polymerization of the PDMS macromonomer only after a fair amount of AN, which reacted to form the homopolymer, has reacted. At this stage the viscosity of the reaction would have increased, further impairing polymerization of the PDMS macromonomer due to its lower mobility compared to the AN monomer. This will lead to a low incorporation of PDMS macromonomer.

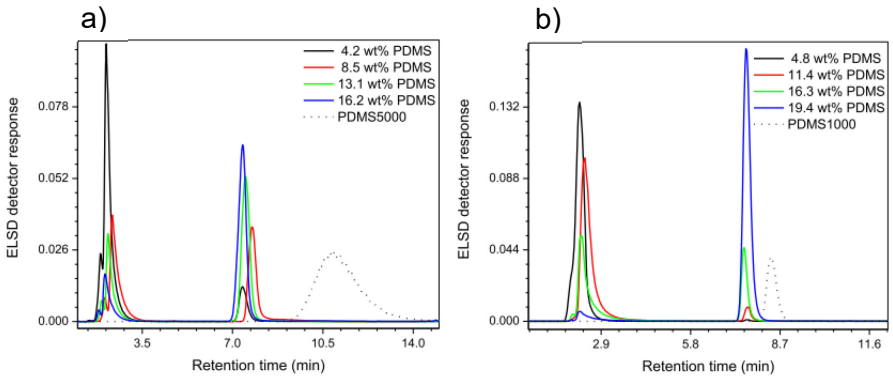

Figure 2.11: HPLC chromatograms of reaction products of PAN-g-PDMS copolymerizations using a) 5kDa and b) 1kDa PDMS macromonomer feeds (traces are of PDMS macromonomer samples) [2]

2.5 Physical properties of PAN-g-PDMS copolymer solutions

The incorporation of PDMS graft macromonomers leads to copolymers with physical properties distinct from that of homopolymers of PAN. Bayley *et al.* reported an overall increase in shear viscosity in DMF solutions containing PAN-g-PDMS copolymers when comparing samples containing 4.8 wt.% PDMS to samples containing 19.4 wt.% PDMS grafts of 1 kDa.[2] This increase in viscosity, along with a shift in inflection point of shear thinning to higher shear rates, was attributed to the self-assembly of the amphiphilic copolymers used of which the PDMS grafts are not completely dissolved in DMF leading to the formation of aggregates that increase the hydrodynamic volume of the constituent copolymers.[2]

2.6 Thermal behaviour of PAN-g-PDMS copolymers

Thermal analysis is a useful tool to investigate the exothermic enthalpy associated with the cyclization reaction of PAN-based polymers; a reaction that leads to ladder-type polymeric structures as a precursor to the carbonization process. It has been found that incorporation of comonomers into the PAN polymer backbone will alter the thermal behaviour of the polymer.[1,16,17] Preta *et al*. found that the incorporation of methyl methacrylate and itaconic acid shifts the onset point of the cyclization reaction to a lower temperature.[16] Jamil *et al*. found that the incorporation of methyl acrylate increased the onset point of the cyclization reaction to a higher temperature.[17] Both these groups reported a decrease in the exothermic enthalpy of the cyclization reaction.[16,17] The results were, however, published as-is without correcting for the fact that the inserted comonomers will not contribute to the exothermic heat enthalpy inherent in the cyclization reaction of PAN.

Human conducted thermal analysis on PAN-g-PDMS copolymers, of which the thermograms are shown in *Figure 2.12*, and found that, in both films and fibers consisting of PAN-g-PDMS copolymers, an increase in the amount of PDMS grafts increased the exotherm peak temperature and decreased the fraction of PAN that undergo the cyclization reaction.[1] This means that with an increase in PDMS grafts the exotherm enthalpy decreased per mass of the analysed copolymer, as expected when fewer nitrile groups are present, as well as per mass of the PAN polymer sections contained in the analysed copolymer. This suggests that the cyclization reaction takes place to a lesser extent in the PAN-g-PDMS copolymers than in the PAN homopolymers, implying that there are more non-cyclized nitrile groups present after the cyclization reaction took place.

a)

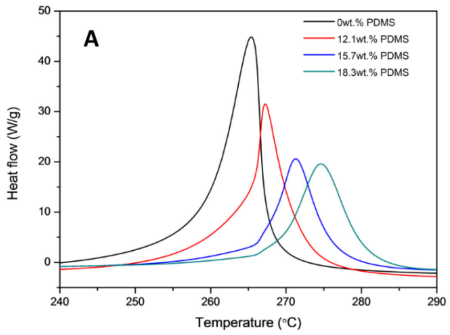

b)

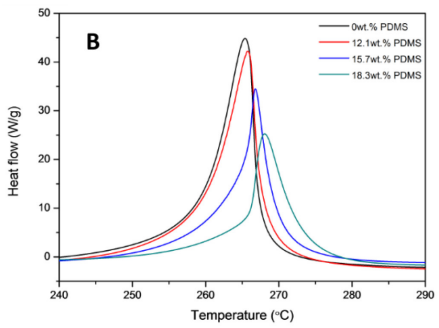

c)

Table
DSC peak maxima and peak area (determined from nitrogen atmosphere thermograms) for different PDMS wt. % for the grafted polymers

	PDMS (wt. %)	Peak maxima (°C)	Peak area (J/g)	Corrected[a] peak area (J/g)
Films	0%	265.1	358.9	358.9
	12.1%	267.9	266.1	233.9
	15.7%	272.0	251.5	212.0
	18.3%	275.5	249.3	203.7
Fibres	0%	265.4	367.4	367.4
	12.1%	265.5	344.8	303.1
	15.7%	267.4	306.1	258.0
	18.3%	268.7	289.1	236.2

[a] Corrected for PDMS content

Figure 2.12: DSC thermograms for a) films and b) fibers in nitrogen atmosphere with c) accompanying table containing peak maxima, peak areas and corrected peak areas [1]

2.7 Electrospinning of polymer nanofibers

The electrospinning method is used to produce a highly porous mesh consisting nanofibers with very large surface-to-volume ratios by using a relatively simple setup.[18] During electrospinning, a polymer solution is presented at the tip of a spinneret under the application of an electric field.[19] Once the charge repulsion exceeds the surface tension of the polymer solution, a jet of solution is ejected towards a grounded collector plate.[19] By changing various parameters, porous nanofibers can be formed by exploiting the solubilities of electrospun polymers.[1,2,20,21]

There are various parameters inherent in the process of electrospinning. The following list contains only a few such parameters:

- Concentration and molar mass of polymers
- Spinning solvent
- Solution ageing
- Polymer composition
- Tip-to-collector distance

2.7.1 Concentration and molar mass of polymers

For a given polymer solution, the concentration of the polymer in a solution must be above a critical value for chain overlapping and subsequent entanglement, accompanied by a sharp increase in viscosity, to occur.[19] *Figure 2.13* shows results by Shenoy *et al*. that demonstrated that each polymer chain must have at least two points of entanglement with other polymer chains for initiation of fiber formation to occur during electrospinning.[19] Essentially this means that all polymers in the solution must be connected in a network by chain entanglements. It was found that above a solution entanglement number of 3.5 (that is 2.5 entanglements per polymer chain), fibers are formed during electrospinning.[19] The molar mass as well as the concentration of the polymers in solution determine

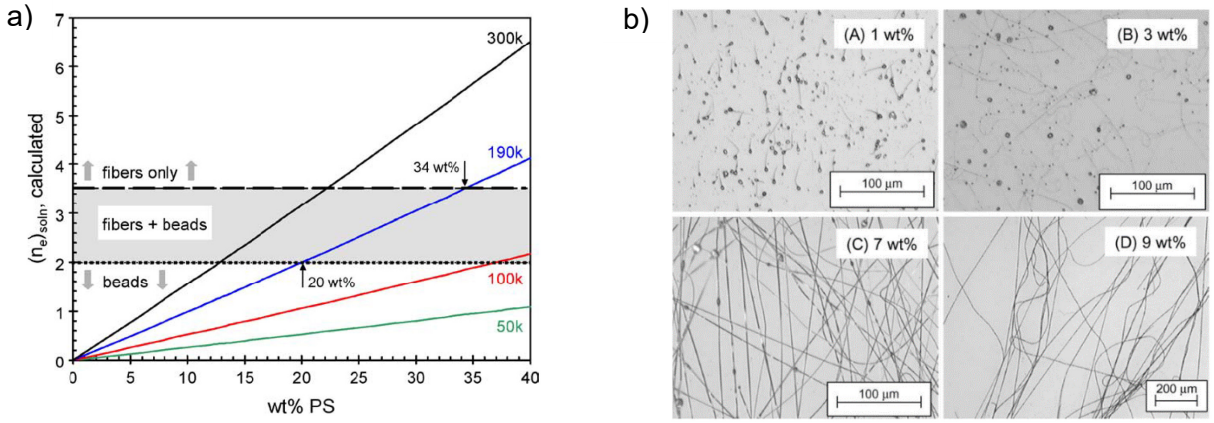

Figure 2.13: a) Plot of calculated entanglement number per polymer chain as a function of polymer concentration for different molar masses of PS/THF polymer solution where the dashed line indicates the estimated transition to fibers and the dotted line indicates the estimated transition to fibers and beads supplemented by b) optical microscopy images of electrospun PVP/EtOH showing the transition from beads to fibers as the polymer solution concentration is increased [19]

the amount of chain entanglements.[19] They developed an equation to calculate the amount of chain entanglements in order to predict the concentrations at which beadless fibers form.[19] The predictions showed good correspondence with experimental values.[19]

2.7.2 Spinning solvent

Figure 2.14 demonstrates the effects of the spinning solvent. Liu *et al*. have reported the formation of a porous fiber morphology by using *in situ* mixing microfluidics that enabled mixing and simultaneous electrospinning.[20] They concluded that incomplete mixing coupled with nonsolvent-induced phase separation leads to the formation of a porous fiber morphology.[20] Human investigated the effect of the addition of chloroform to a PAN-g-PDMS electrospinning solution.[1] An initial decrease of fiber diameter resulted from the addition of 5 % chloroform to the solvent.[1] This was explained by considering the increased solubility of PDMS in the solvent mixture that led to the dissipation of aggregates formed by insoluble PDMS grafts.[1] Fiber diameters increased again as the chloroform content was increased to 7.5 % and 10 % .[1] Again, solubility was considered and the argument was given that the solubility of PAN sections decreased and thereby caused the formation of self-assembled structures inverse to that found in a pure DMF solvent.[1] The solubility of a polymer in a selected solvent, demonstrated by the difference in their solubility parameters, determines the hydrodynamic volume of the dissolved polymer. A greater hydrodynamic volume is associated with

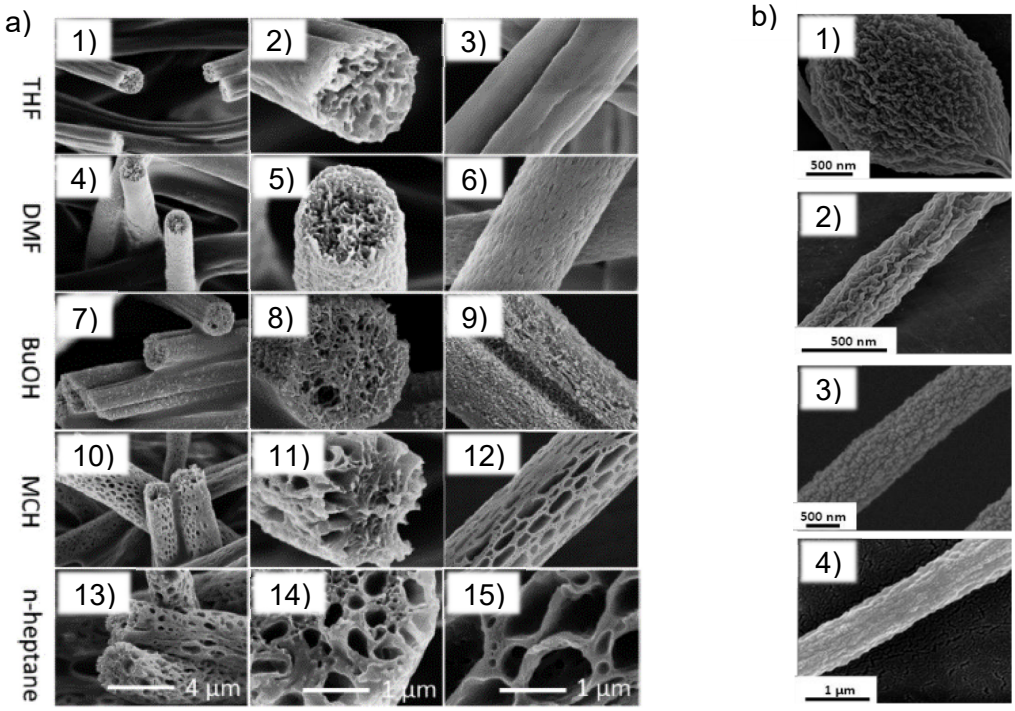

Figure 2.14: a) SEM images of PS fibers electrospun from THF:DMF solution in a 1:1 ratio after *in situ* mixing with 1-3) THF, 4-6) DMF, 7-9) BuOH, 10-12) MCH and 13-15) n-heptane.[20] b) PAN-g-PDMS (12.1 wt.% PDMS) electrospun from a DMF:chloroform solvent mixture containing 1) 2.5 % chloroform, 2) 5.0 % chloroform, 3) 7.5% chloroform and 4) 10.0% chloroform [1]

a greater solution viscosity which leads to a larger fiber diameter. Solvent mixtures do not, as intuition would anticipate, merely lead to fiber diameters intermediate between those of fibers spun from the respective solvents.

2.7.3 Solution ageing

Polymer solutions of PAN-based polymers in DMF undergo a solution ageing phenomenon. This entails shortening of the lengths of solvent bridges between polar nitrile groups, depicted in *Figure 2.15*., that are also highly dependent on temperature.[22] The shortening of these solvent bridges over time increases the solution viscosity leading to electrospun fibers with larger diameters.[1] Eom *et al.* studied the behavior of PAN polymers in both DMF and DMSO with DMF having an overall solubility parameter closer to PAN and DMSO having a polarity more similar to PAN.[22] They came to the conclusion that the lesser chain expansion of the polymers in DMF as opposed to DMSO, as evidenced by the decreased intrinsic viscosity and smaller hydrodynamic volume, is governed by the polar term, δ_p, in the solubility parameter equation rather than the overall solubility parameter, δ.[22] They further investigated the effects of temperature and found that an increase in solution temperature led to a decrease in the intrinsic viscosity and a smaller hydrodynamic volume of the polymers.[22] The explanation given states that the higher mobility of polymer chains at a higher temperature leads to the disintegration of longer solvent bridges and formation of shorter, stronger solvent bridges or even direct coupling between nitrile groups.[22] This can be tracked by UV/Vis spectroscopy where the absorption of the peak between 250 nm and 300 nm increases due to an extension of the conjugated nitrile region.[22] DMF molecules are more easily ejected out of solvent bridges due to the greater difference in polarities between DMF and the nitrile pendant groups.[22]

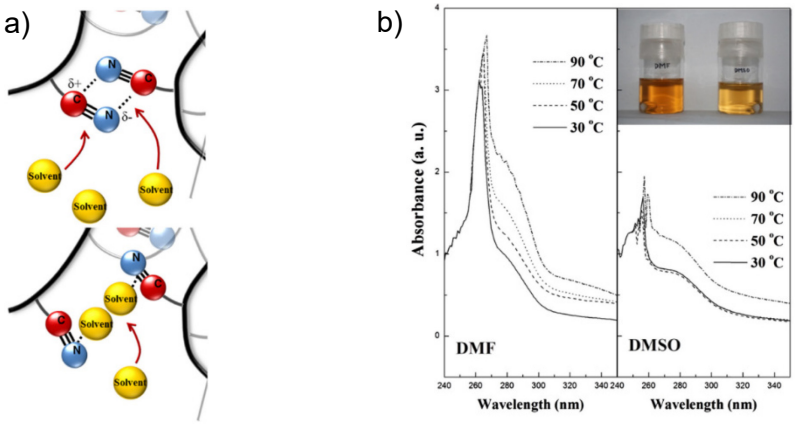

Figure 2.15: a) Schematic illustration of solvent bridges formed upon dissolution of PAN polymers and b) UV/Vis spectra of solutions of PAN in DMF and DMSO at 30 °C, 50 °C, 70 °C and 90 °C [22]

Following results reported by Eom *et al.*, Human conducted a study on the solution ageing of a solution of PAN polymers in DMF. Results of rheological measurements with accompanying SEM images are shown in *Figure 2.16*. The decrease in length of solvent bridges with increased solution

ageing time.[1] The hypothesis states that interdiffusion of polymer chains leads to the shorter solvent bridges and direct nitrile coupling as the timescale is increased.[1]

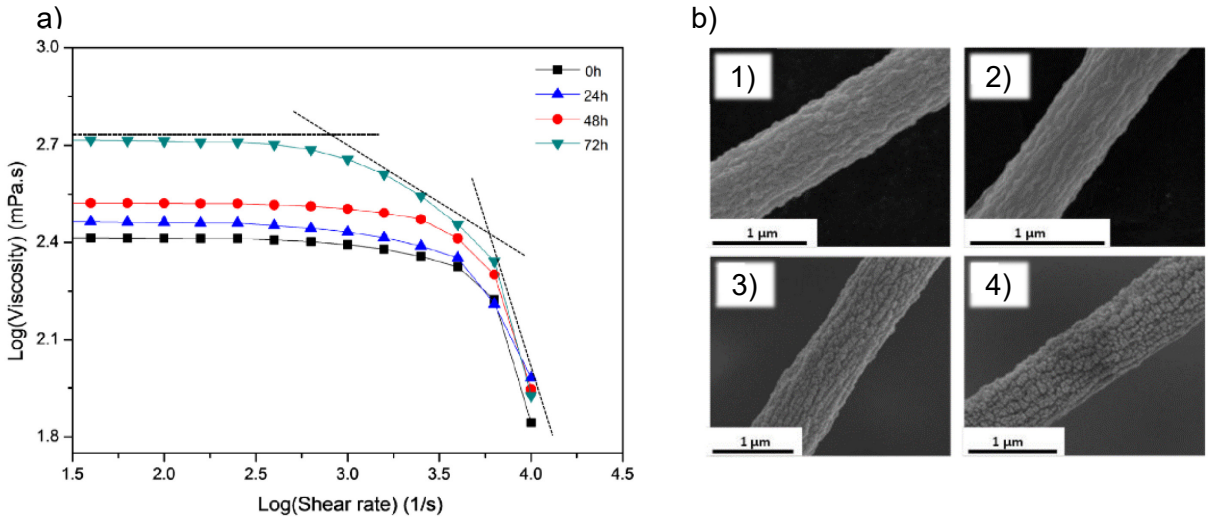

Figure 2.16: a) Rheological measurements of PAN-g-PDMS (12.1 wt. % PDMS) at different solution ageing times and b) SEM images of PAN-g-PDMS (18.3 wt. % PDMS) nanofiber electrospun after solution ageing times of 0 h, 24 h, 48 h and 72 h [1]

It should be noted that there are essentially two types of solution ageing at play in a solution of PAN-g-PDMS in DMF. The first is the shortening of solvent bridges with ageing of the solution. The second is the potential phase separation of the PAN phases and PDMS phases in the polymer solution.

2.7.4 Polymer composition

A number of methods exist that can be used to produce nanofibers containing different polymer compositions. The use of polymer blends, of which resultant fibers are shown in *Figure 2.17*, is one such method.[21] Two polymers are added to a common solvent after which the polymer solution is electrospun. Depending on the miscibility of the polymers as well as their solubility in the common solvent, phase separation will take place to a varying extent. Zhang *et al.* have demonstrated the use of PAN/PVP blended polymer solutions in DMF to electrospun polymer blended nanofibers of which the PVP phases can be extracted using water.[21] Subsequent carbonization led to porous carbon nanofibers with nanoporous structures.[21] The extracted precursor nanofibers as well as the

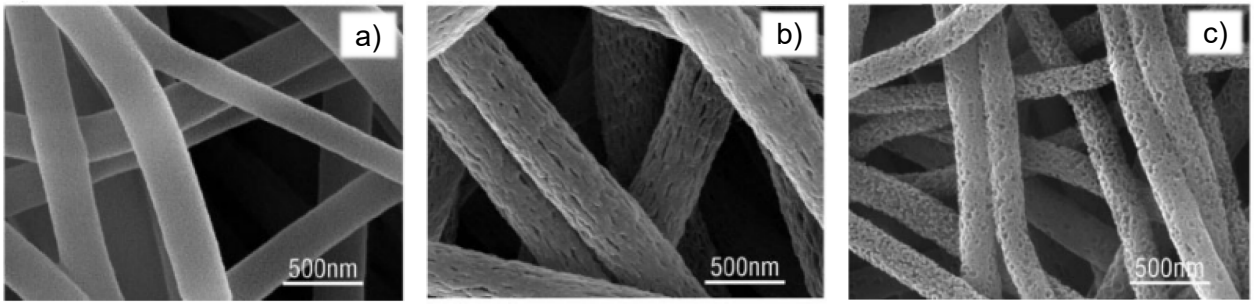

Figure 2.17: a) SEM micrographs of a) PAN/PVP nanofibers electrospun from polymer solution containing a 50:50 ratio of polymers, b) PAN nanofibers prepared by subsequent water-extraction and c) carbon nanofibers produced by subsequent carbonization [21]

carbonized nanofibers showed a drastic increase in pore volume, pore size as well as the surface area w.r.t. the amount of PVP in the electrospinning solution.[21]

The use of amphiphilic copolymers is another, novel method to produce porous nanofibers. *Figure 2.18* shows porous nanofibers prepared by electrospinning of PAN-g-PDMS copolymers.[1,2] Since the chemically distinct moieties are covalently attached to the same polymer chain, macroscopic phase separation is not possible and therefore nanoscopic phase separation will occur. The surface area of carbon nanofibers prepared by carbonization of electrospun PAN-g-PDMS nanofiber precursors, is drastically increased compared to those produced using PAN homopolymers.[1] Electrospinning of the copolymer solutions containing different amounts of PDMS led to distinctly different diameters of the electrospun nanofibers due to the higher solution viscosity attained with a higher PDMS content making fiber stretching a slower process.[2] Fiber diameters were shown to decrease and become more uniform with an increase in TCD for all amounts of 1 kDa and 5 kDa PDMS grafts added up to 19.4 wt.% and 16.2 wt.% respectively.[2] Decreasing the TCD leads to a decrease in fiber flight time which results in less fiber stretching and solvent evaporation and ultimately yields thicker fibers.[2]

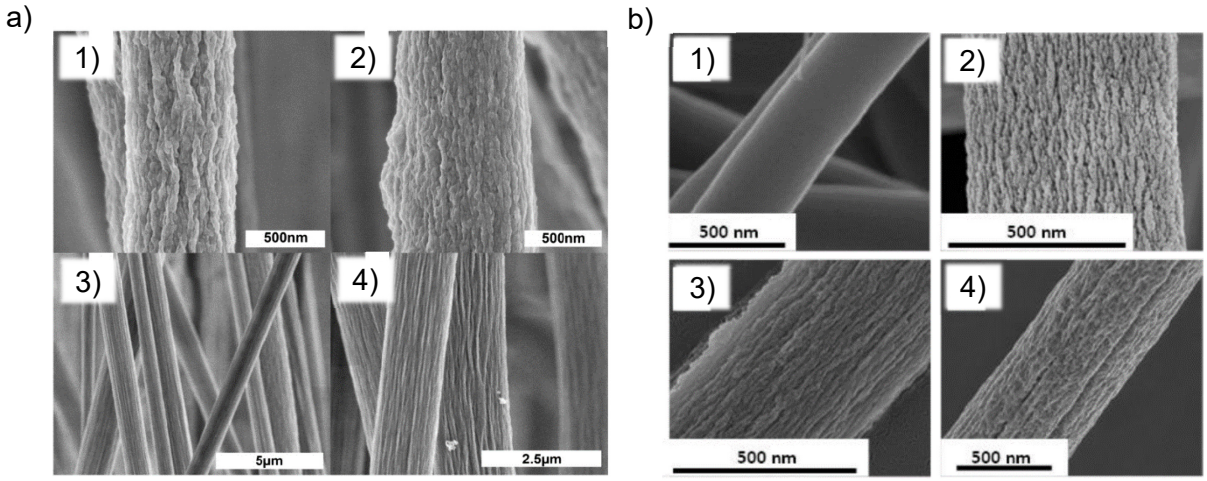

Figure 2.18: a) SEM micrographs of PAN-g-PDMS fibers containing 1,2) 8.5 wt.% PDMS (5 kDa PDMS grafts) and 3,4) 13.1 wt.% PDMS (5 kDa PDMS grafts) reported by Bayley.[2] b) PAN-g-PDMS fibers containing 1) 0 wt.%, 2) 12.1 wt.%, 3) 15.7 wt.% and 4) 18.3 wt.% PDMS (1 kDa PDMS grafts) [1]

2.7.5 Tip-to-collector distance

*Figure 2.*19 shows the effect of an increase in TCD on the electrospun fiber diameter of PAN-g-PDMS copolymer nanofibers.[2,9] Basson found that an increase in the TCD leads to a decrease in fiber diameters due to the longer flight time causing more stretching and more complete evaporation of the solvent.[9] More uniform fiber distributions were observed at a greater TCD.[9] Bayley *et al*. also reported a decrease in fiber diameter and more uniform fibers with an increase in TCD and provided the same explanation.[2] There is a clear plateau followed by a steady increase in fiber diameter from 16cm to 20cm TCD for the copolymer containing 19.4 wt.% PDMS grafts. This was ascribed to the gel-like behaviour of PAN-g-PDMS in DMF which is amplified in the copolymers containing a higher

amount of PDMS due to the large ratio of copolymer to homopolymer formed in the polymerization reaction as presented in the HPLC chromatograms shown in *Figure 2.11*.[2]

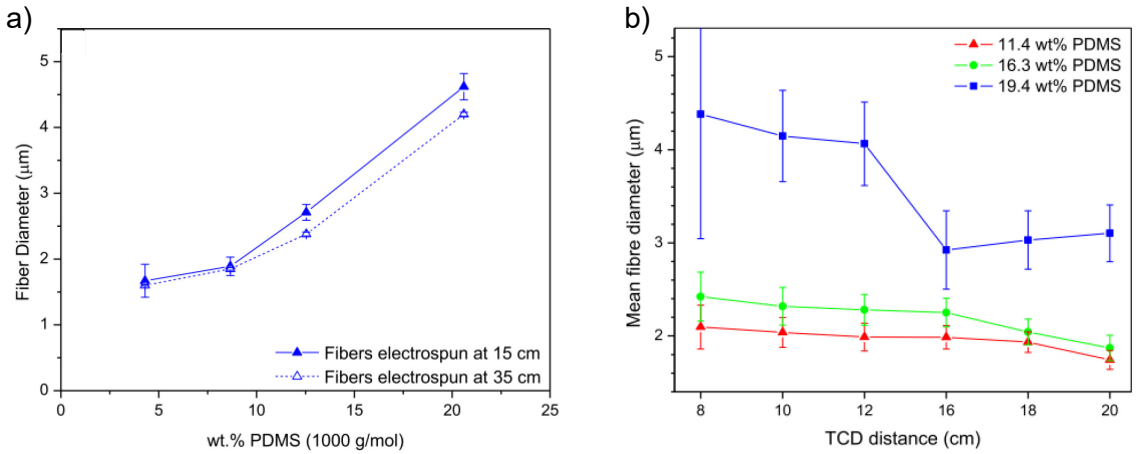

Figure 2.19: a) Plot of PAN-g-PDMS copolymer fiber diameter w.r.t. PDMS graft content electrospun at 15cm and 35cm TCD.[9] b) Plot of PAN-g-PDMS copolymer fiber diameter w.r.t. TCD for 11.4 wt.%, 16.3 wt.% and 19.4 wt.% PDMS graft content.[2] Bars represent the standard deviation of the mean fiber diameter values [2]

2.8 Magnetic iron oxide nanoparticles

Iron oxide nanoparticles can by synthesized by a number of methods. Microemulsion, thermal decomposition and co-precipitation are perhaps the simplest methods of which the resultant nanoparticles are shown in *Figure 2.20*.

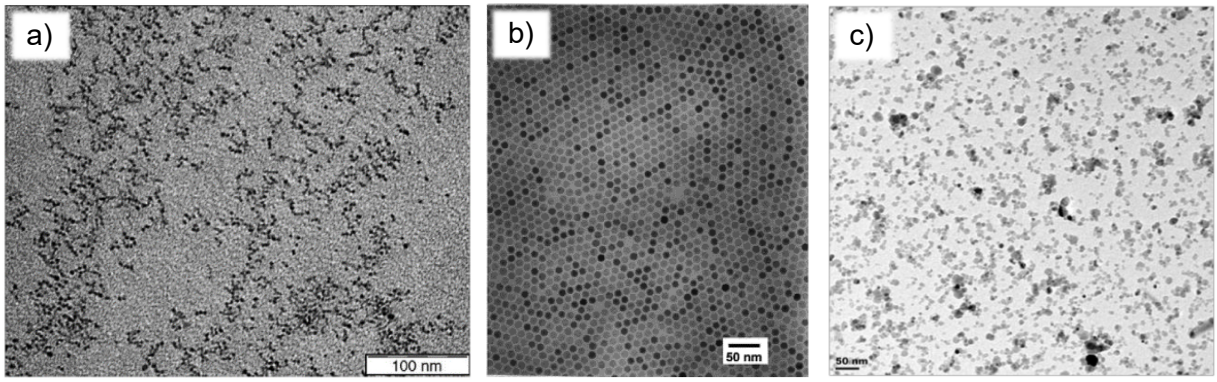

Figure 2.20: IONPs synthesized by a) microemulsion, b) thermal decomposition and c) co-precipitation [24,28,34]

Microemulsion employs a water-in-oil type reaction with iron precursors precipitating inside the droplets upon addition of a base.[23,24,25] Well-defined droplets are dispersed by a monolayer of surfactant molecules with their hydrophobic tails dissolved in the oil phase and their hydrophilic heads dissolved in the aqueous phase to form a thermodynamically stable dispersion of two immiscible phases.[25] Particle sizes can be varied greatly by varying the reaction parameters of the microemulsion procedure. Vidal-Vidal *et al.* have demonstrated the synthesis of nanoparticles smaller than 10 nm with diameters of 9.0 ± 2.3 nm and 3.5 ± 0.6 nm using cyclohexylamine and oleylamine or oleic acid respectively as precipitating agents.[24] Sahoo *et al.* succeeded in decreasing particle size from 21.2 nm to 2.1 nm by increasing the shear rate during the precipitation procedure.[23]

The given hyopthesis states that micro-droplets of oil are formed in the dispersed aqueous phase during vigorous stirring that act as colliders breaking up the aqueous phase droplets to an extent proportional to the rate of stirring.[23]

Thermal decomposition of iron precursors such as $Fe(CO)_5$ (iron pentacarbonyl), $Fe(acac)_3$ (acac=acetylacetonate) and $Fe(cup)_3$ (cup=*N*-nitrosophenylhydroxylamine) in an organic solvent can be employed to synthesize high-quality IONPs with good size-uniformity.[25] In addition to yielding monodisperse nanoparticles, thermal decomposition allows size-control of the nanoparticles.[26,27,28,29] The thermal decomposition method entails the heating of water-soluble iron precursors in a water-in-oil type reaction in the presence of a surfactant such as oleic acid or lauric acid.[26,27,28,29] A high-boiling organic solvent such as dioctyl ether or diphenyl ether is used as the reaction must be heated to reflux.[26,27,28,29] Simeonidis *et al*. demonstrated the synthesis of IONPs with mean size and standard deviation of 4.9 nm ± 9.3 %, 12.3 nm ± 7.1 % and 14.7 nm ± 6.7 % by changing the iron precursor, surfactant, solvent and the ratio of the iron precursor to the surfactant.[27] Park *et al*. reported the preparation of nanoparticles with sizes of 6, 7, 9, 10, 12, 13 and 15 nm, all except the 6 nm particles having a standard deviation less than 5 % (8.5 % for the 6 nm particles), by oxidation of synthesized particles of which the size was controlled by varying the concentration of iron precursor and the ratio of iron precursor to surfactant.[26] A drawback of this method is the high temperatures required.[25,26,27,28,29] As an example, temperatures required for reflux of diphenyl ether and dioctyl ether are respectively 260 °C and 290 °C.[27] Some of the iron precursors generally employed, such as iron pentacarbonyl and decomposition products of iron acetylacetonate, are toxic which raises health concerns w.r.t. upscaling of the thermal decomposition method. Another drawback is that the as-synthesized nanoparticles are generally only dispersed in organic solvents.[25] This is due to the remnant surfactant coating which is not removed during the work-up procedure.

Co-precipitation is the most conventional method of synthesizing magnetite or maghemite IONPs.[25] It is a safe, simple and easy method that does not require any additional instrumentation not typically used in a chemistry lab. The precipitation procedure is carried out by adding a base such as ammonia or sodium hydroxide to an aqueous solution containing ferrous and ferric ion precursors.[30,31,32,33,34,35] The size and shape of the nanoparticles are affected by various reaction conditions including the ratio of ferrous to ferric ions, stirring rate, reaction temperature, pH of the reaction medium and ionic strength of the reaction medium.[25] Shen *et al.* reported the formation of maghemite, Fe_2O_3, instead of magnetite if the reaction temperature was below 60 ℃ or if insufficient ammonia (used as base) was added.[33] The formation of maghemite instead of magnetite can be observed as a brownish colour of the product.[33] Kim *et al.* found that an increase in the concentration of base used at a constant pH will lead to greater particle diameters while an increase in pH at a constant concentration of base will lead to smaller particle diameters.[31] According to thermodynamic modeling, complete precipitation of Fe_3O_4 is expected when a 2:1 molar ratio of Fe^{3+} to Fe^{2+} is used with a pH between

7.5 and 14 in a non-oxidising environment.[31] Nanoparticles with a mean diameter smaller than 10 nm can be synthesized.[30,31,32,33] Particle diameters of 9.2 ± 1.1 nm, 9.3 ± 2.6 nm and 11.8 ± 2.3 nm and 9.0 ± 1.2 nm have been reported.[30,33,34,35] Particles with a wide size distribution are produced that will require further size selection methods if a narrow size distribution is required.[25]

Other methods have been reported as well. Ziolo *et al.* reported an *in-situ* synthesis of IONPs in a polystyrene-based polymer resin by an ion-exchange reaction.[36] Schnepp *et al*. reported the synthesis of iron carbide, Fe_3C, in a gelatin gel matrix that led to iron oxide nanoparticle intermediates.[37]

A general issue in analyzing iron oxide is the similarity between WAXD diffraction patterns as well as FTIR spectra of magnetite and maghemite, as shown in the diffraction pattern and spectra in *Figure 2.21*.[26,27,29] Additional analysis, such as Raman spectroscopy and Mössbauer spectroscopy, are often carried out to unequivocally identify the iron oxide phases present.[28,29]

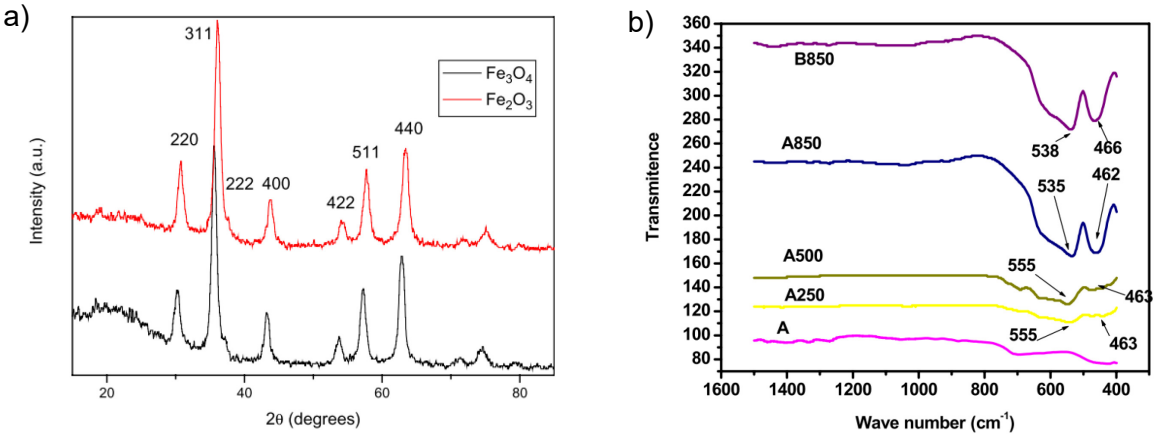

Figure 2.21: a) XRD diffraction patterns of maghemite (red) and magnetite (black).[32] b) FTIR spectra of IONPs of different precursor particles (A: 21.2 nm, B: 2.1 nm diameter) calcinated at different temperatures [23]

2.9 Carbonisation of PAN-IONP nanocomposites

Wojcik *et al.* proposed a scheme of IONP decomposition in a carbon matrix during thermal treatment, shown in *Figure 2.22*.[38] They found that nanocomposites consisting of magnetite nanoparticles embedded in PAN nanofibers had the following crystalline phases after carbonization at 1000 °C: Fe_3O_4 (magnetite), γ-Fe, α-Fe, Fe_3C (iron carbide) and C (graphite).[38] In the interior of the particles, Fe_3O_4 can undergo a phase transition to α-Fe below 572 °C followed by a phase transition to FeO (wüstite) at higher temperatures; both transitions having oxygen as a by-product.[38] Above 723 °C α-Fe can phase transform to γ-Fe.[38] The surface iron atoms can form Fe_3C with carbon atoms from the surrounding polymer matrix; again oxygen is released as a by-product.[38] It should be noted that the authors made no distinction between magnetite, Fe_3O_4, and maghemite, Fe_2O_3, during analysis of the abovementioned phase transitions, which reiterates the difficulty of distinguishing between magnetite and maghemite.

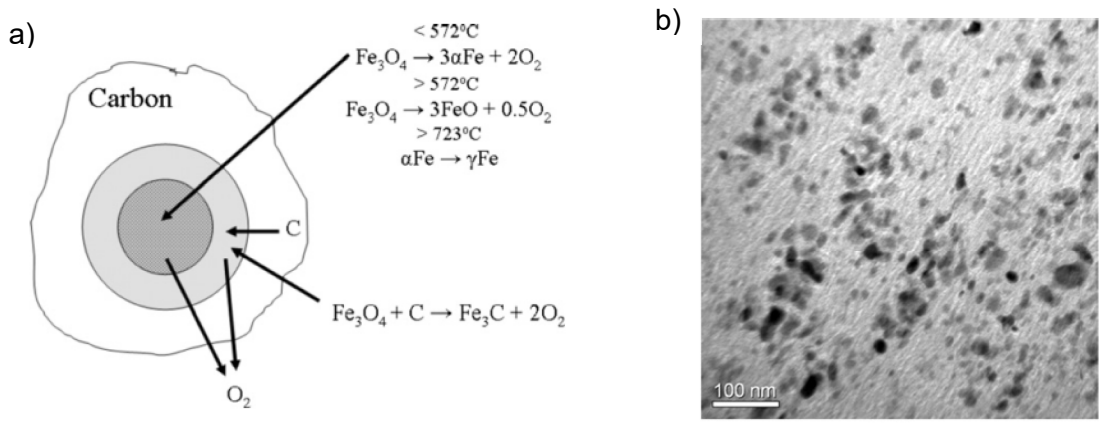

Figure 2.22: a) Scheme of hypothesized phase transitions of magnetite nanoparticles in solution-spun polyacrylonitrile fibers that occur during carbonization with accompanying b) TEM image showing the dispersion of the nanoparticles in the spun polymer matrix [38]

2.10 Silica coating of iron oxide nanoparticles

The Stöber method provides a simple yet reliable reaction procedure for the formation of silica nanoparticles.[39] Pioneering studies, of which results are shown in *Figure 2.23*, found that the solvent (pure or mixture), silicating agent, concentration of silicating agent, concentration of base and concentration of water all affect the particle diameter.[39] The parameters of the procedure can therefore be varied in order to design the synthetic procedure that yields the desired particles. Bekanskienė *et al*. investigated the effects of various parameters on the resultant silica nanoparticles and found that an increase in water added to the reaction leads to an increase in particle diameter while an increase in the amount of ammonia used has the same effect to a different extent.[40] It was also found that the particle size was strongly dependent on the solvent used with the size increasing as follows: methanol<ethanol<2-isopropanol<acetone.[40] Their results showed an increase in particle diameters from 25-35 nm to 35–40 nm for an increase in reaction time from 5 days to 13 days.[40] The small increase might be attributed to depletion of most of the TEOS silicating agent used during the first 5 days of the reaction. Ibrahim *et al*. found that a doubling of the concentration of TEOS from 0.2 M to 0.4 M increased the average particle diameter from ~50 nm to ~65 nm.[41]

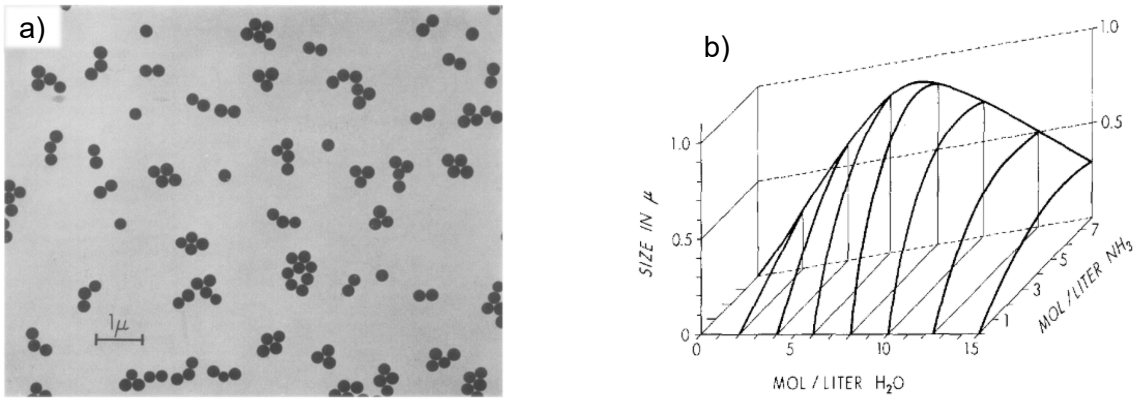

Figure 2.23: a) TEM image of silica nanoparticles prepared in an ethanol-ethyl ester system and b) plot depicting size of silica particles formed under varying concentrations of water and ammonia [39]

IONPs with reactive hydroxyl surface groups, can be used as seeds for the silicating agent employed to form core-shell structures of nanoparticles as seen in *Figure 2.24*.[25] Thus, silica shell is formed around the nascent IONPs resulting in a core-shell nanoparticle structure. By varying the concentrations of ammonia, TEOS and water, silica shell thickness can be controlled between 5 and 200 nm.[25] The magnetic properties of the nascent particles will be altered in the process.[25] The parameters of such a silica coating reaction are slightly different to those of the authentic Stöber method. Reaction parameters are varied to tune the silica shell thickness instead of the silica particle diameter. Deng *et al*. found that the thickness of the silica shell can easily be altered by varying the concentration of TEOS silicating agent.[42] Silica shells could be formed in a large range of ammonia concentrations with higher concentrations leading to the formation of silica nanoparticles.[42] Tadyszak *et al*. reported a procedure to synthesize silica-coated IONPs using oleic acid coated IONPs as starting material; an useful protocol (though experimentally involved) to use in conjunction with the thermal decomposition method as the nascent IONPs are coated with oleic acid.[43]

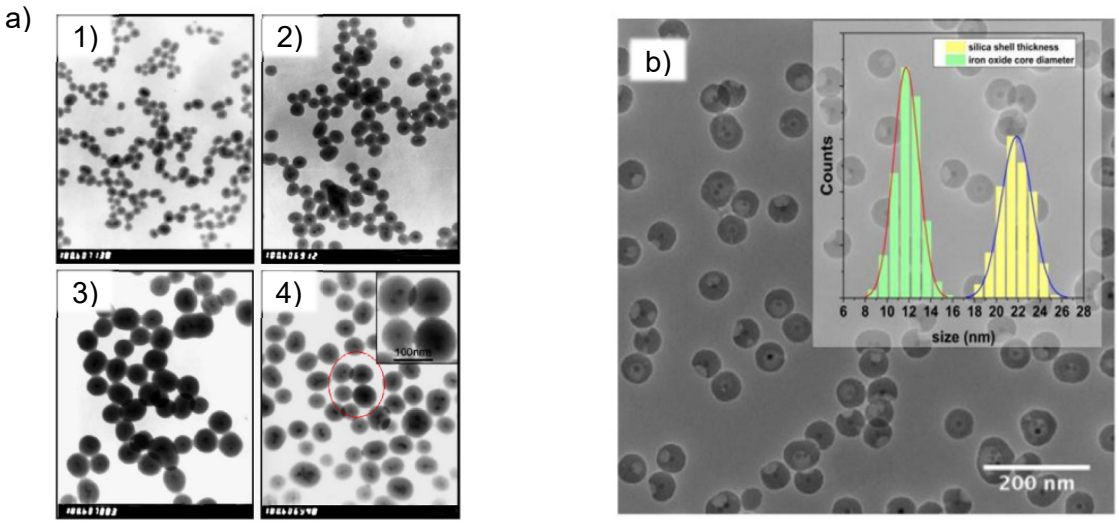

Figure 2.24: a) TEM image of silica-coated IONPs synthesized at increasing concentrations of TEOS.[42] b) TEM image with accompanying size distribution of nascent IONPs (green) and subsequent silica-coated IONPs (yellow) [43]

Figure 2.25 shows the formation of multi-core silica-coated IONPs. The dispersion of the IONPs as well as the solubility of the silicating agent must be taken into account when choosing a solvent or solvent mixture for the reaction. TEOS is miscible with ethanol while IONPs are well-dispersed in water. Deng *et al*. found that silica shells can be formed around IONPs for a wide ratio of ethanol:water solvent mixtures from 2:1 to 4:1 volume ratios.[42] As the amount of water is increased, dispersion of the IONPs improves while the formation of silica nanoparticles becomes more likely due to the fast hydrolysis of the TEOS resulting in phase separation between the silica nanoparticles and the intended IONP reaction seeds.[42] Alternatively, a decrease in water leads to poor dispersion of the IONPs and irregularly silica-coated aggregates of IONPs.[42] During a silica coating procedure, either multi-core nanoparticles or single-core nanoparticles can be formed. Lakay reported the

formation of clusters of IONPs inside the core of the formed silica shell and subsequently hypothesized two possible routes of the reaction: sterically stabilized IONPs leading to single-core nanoparticles or moderately agglomerated IONPs leading to multi-core nanoparticles.[35] Considering the TEM images and procedures published by Deng *et al*., this agglomeration of IONPs in the reaction matrix can be avoided by surface functionalization of the IONPs and using a very low concentration in the silica coating reaction.[42] Trisodium citrate was used to functionalize the surfaces of the IONPs to improve dispersion in aqueous media while the concentration in the reaction mixture was 0.02 wt.%.[42] This procedure led to single-core silica-coated nanoparticles.

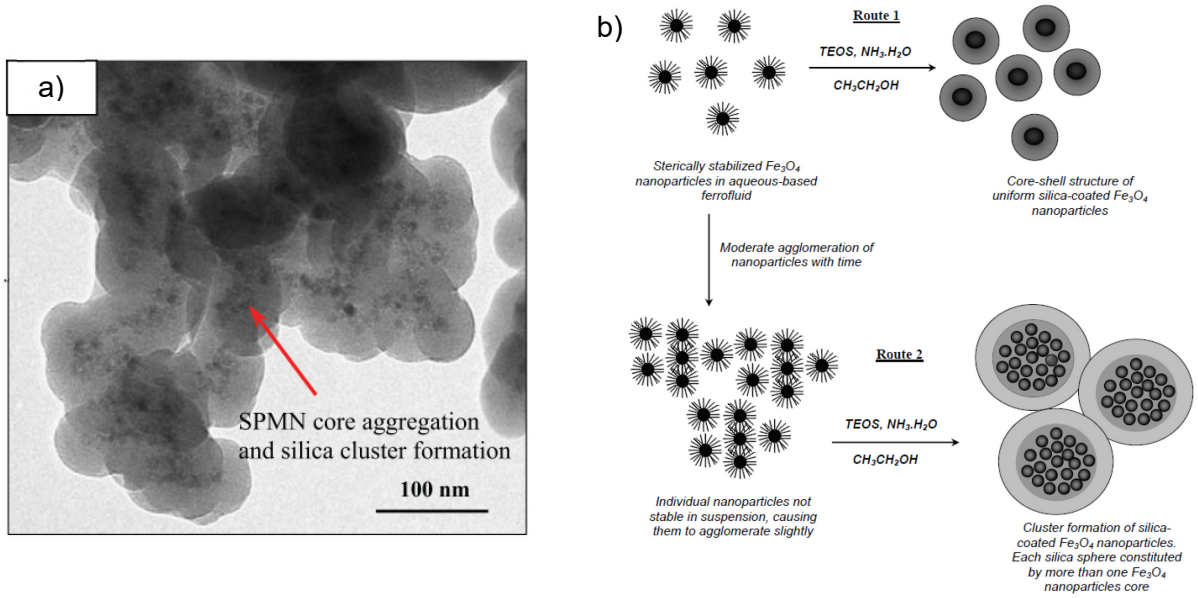

Figure 2.25: a) TEM image of multi-core silica-coated IONPs and b) schematic illustration of the process of formation of either single- or multi-core silica-coated IONPs [35]

Due to reactive hydroxyl groups on the surfaces of silica nanoparticles, further surface functionalization can be achieved. Li *et al*. investigated the surface functionalization of silica nanoparticles with oleic acid and found that the extent of modification influences the dispersion of the particles in different media.[44] Amine functionalities can be attached to the silica surfaces using alkoxysilanes.[45,46]

2.11 Polymer-particle nanocomposites

Dispersion of polymer nanoparticles in a polymer melt has proven to be non-trivial. It is well known that the surface charge of nanoparticles plays an important role in the dispersion or agglomeration of the particles in the surrounding medium, however, other factors must also be taken into consideration.[47] Mackay *et al*. developed a theory of particle dispersion of which results and a schematic representation of agglomerated particles is shown in *Figure 2.26*. By dispersing polymer nanoparticles consisting of polystyrene and polyethylene in a polyethylene melt, they demonstrated, by means of SANS, that no particle agglomeration takes place if the particle radius is smaller than the radius of gyration of the polymers in the melt provided that there are enthalpically favourable

interactions between the surface groups and the medium.[48] The given hypothesis states that mixing is promoted if particles are small enough that the favorable interactions between the nanoparticle surfaces and the polymer medium would overcome the Van Der Waals attractions between particles.[48] In the schematic shown in *Figure 26*, δ is the effective distance over which Van Der Waals forces operate, A is the total area of each particle, A_c is the area of contact between particles that will experience attractive Van Der Waals forces and A_u (= A - A_c) is the area that does not experience such forces and can interact with the medium.[48] If the particles are very small, A_c tends towards A and dispersion is not possible while larger nanoparticles will suffer from having a smaller gain in enthalpy of mixing due to their smaller numbers for a given volume fraction.[48]

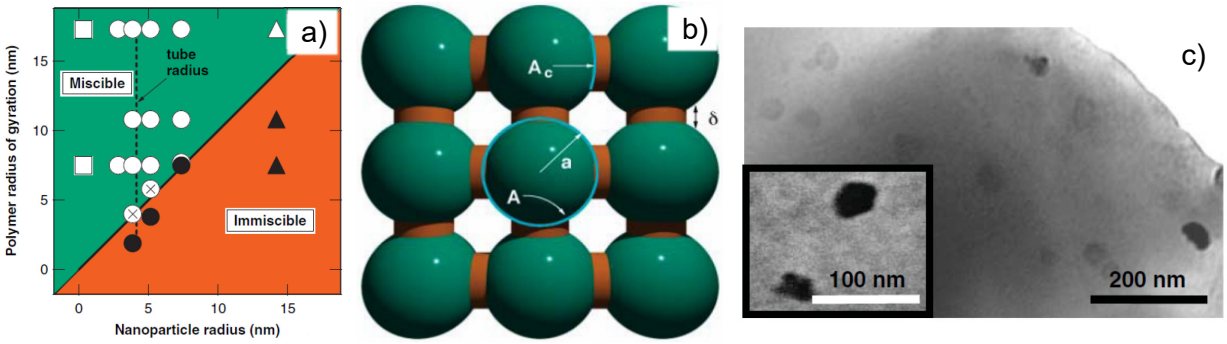

Figure 2.26: a) Polymer radius of gyration-nanoparticle radius phase diagram for C_{60} nanoparticle-polystyrene (squares) system, polystyrene nanoparticle-polystyrene (circles) system and dendritic polyethylene-polystyrene (triangles) system indicating regions of phase separation (solid shapes), some agglomeration (open shapes with crosses) and miscibility (open shapes), b) schematic of agglomerated nanoparticles showing total area (A), particle radius (a), effective distance of Van Der Waals forces (δ) and area of contact between particles (A_c) and c) TEM image of a blend containing well-dispersed 4 % wt. dendritic polyethylene in 393 kDa polystyrene [48]

Liu *et al*. found, by means of computational calculations, that a relatively good dispersion of nanoparticles in a polymer melt can be achieved at moderate polymer-particle interactions, as shown in *Figure 2.27*.[49] This was concluded by considering the number of neighbouring particles within 6.5 times the particle radius.[49] From their results on the time-dependence of dispersion it was clear that moderate polymer-particle interactions will lead to an improvement of dispersion with time as the amount of neighbouring particles will decline.[49]

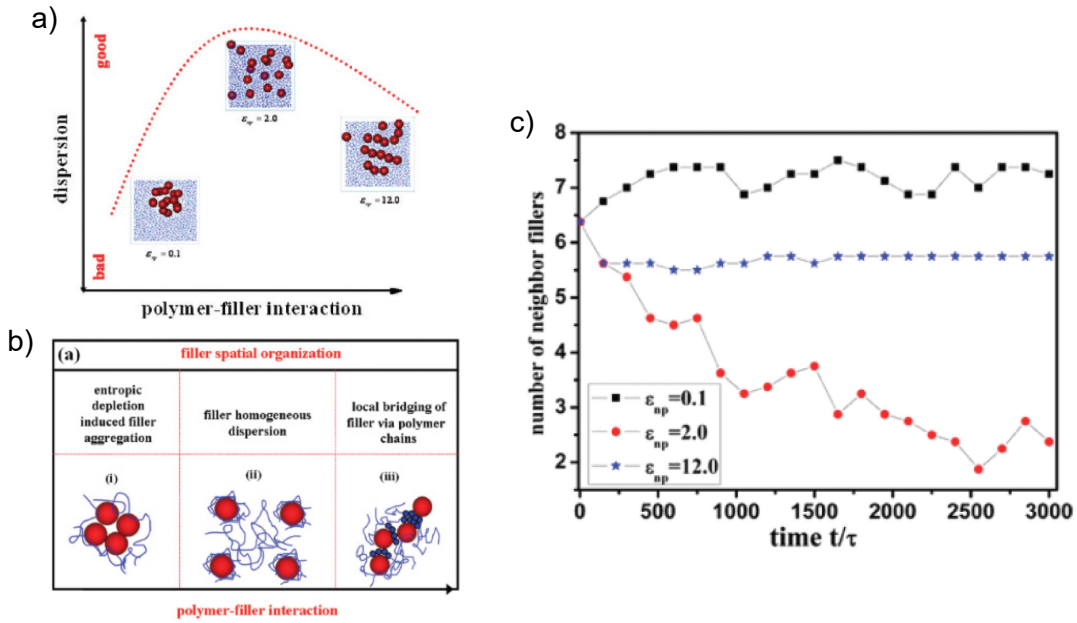

Figure 2.27: a) Dispersion of particles with accompanying snapshots of particles in polymer melt as well as b) illustration of filler spatial organization w.r.t. polymer-particle interactions and c) number of neighbouring particles w.r.t. time for different polymer-particle interactions from results of computational simulations [49]

It was also found that polymer-coated nanoparticles are well-dispersed in a polymer melt, as concluded from the distribution curve in *Figure 2.28* showing a maximum at around 10 r/σ (distance from center/radius of particle).[49] They found that there was no direct contact between the particles and that repulsions between the grafted polymer chains led to large interparticle distances as illustrated by the radial distance, nearly 10 times the particle radius, of the maximum value of the radial distribution.[49] They also found that very strong interactions between the particles and the medium leads to local bridging of the particles via polymer chains, causing the particles to be in close proximity to each other.[49]

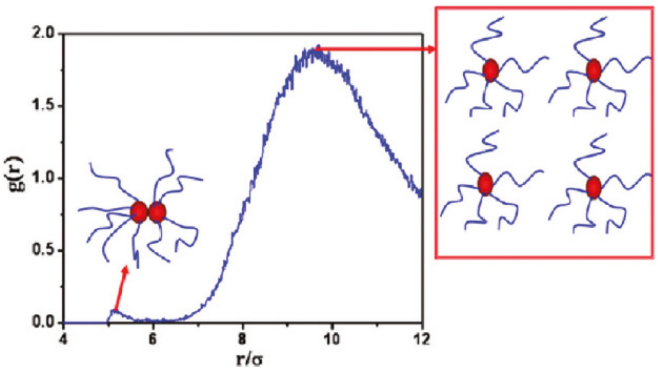

Figure 2.28: Computational result for the radial distribution function of polymer grafted particles in a polymer melt showing good dispersion at moderate polymer-particle interactions [49]

Zhang *et al*. studied the dispersibility of various commercially available nanoparticles in water.[50] Among a variety of nanoparticles, including maghemite nanoparticles, they found that silica nanoparticles were the most stable in water due to its low Hamaker constant which defines attractive interactions between particles.[50] Using DLVO (Derjaguin-Landau-Verwey-Overbeek), they presented a plot of the net energy between particles and the separation distance between particles, shown in *Figure 2.29*.[50] A higher peak represents a greater energy barrier to agglomeration. Silica nanoparticles were better dispersed in pure water than in tap water due to the effect of electrolytes on the electrical double-layer around nanoparticles.[50]

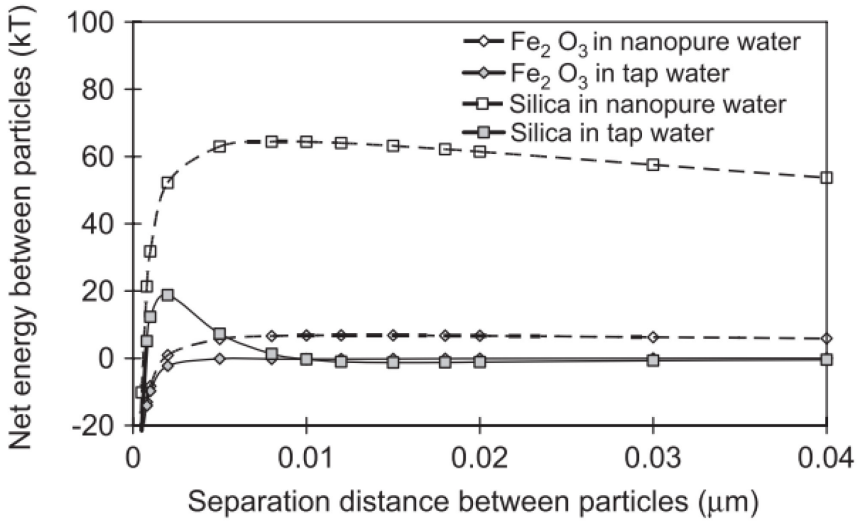

Figure 2.29: DLVO interaction energy between two identical particles of Fe_2O_3 (5-25 nm) and silica (10 nm) in pure water and tap water [50]

2.12 Carbonisation

Carbonisation of PAN-based nanofibers is done at high temperatures in an inert atmosphere. Authors have reported carbonisation temperatures ranging from 600 °C to 1100 °C.[1,3,38,51,52]

It has been postulated that carbonyl groups, hydroxyl groups and carboxylic groups facilitate the initiation of the cyclization process that takes place by a nucleophilic attack and thereby accelerate the subsequent ring-closure reactions.[5] The presence of oxygen promotes the aromatisation of the cyclized sequences by elimination of water.[5] Avilés found that, even after prolonged drying at 110 °C, DMF, acting as a plasticizer, was still present in the PAN polymer samples.[5] This is to be expected considering the molecular interactions between the DMF amide group, having a high dipole moment, and the strongly polar nitrile groups of the PAN polymers.[5] Interactions between nitrile groups in bulk PAN are replaced by interactions between nitrile groups and DMF molecules in PAN containing residual DMF.[5] Upon carbonisation, the thermoplastic polymer chain is transformed into a non-meltable ladder-type polymer chain with a closed chain aromatic structure.[5] Avilés confirmed the cyclization of PAN using FTIR by considering the reduction in intensity of the C-N nitrile stretch absorption band at c.a. 2220 cm^{-1} and the formation of a broad C-C double bond stretch and a C-N double bond stretch band at c.a. 1690 cm^{-1}.

According to the diagram by Fitzer *et al*., shown in *Figure 2.30.a*, carbonisation reactions, emitting hydrogen cyanide and nitrogen as gas, occur above 500 °C and 700 °C respectively.[4] Therefore it is advisable to do a carbonisation procedure above 700 °C. Human proposed a reaction scheme for carbonisation of PAN-g-PDMS polymers shown in *2.30.b*.[1] It is proposed that essentially the same

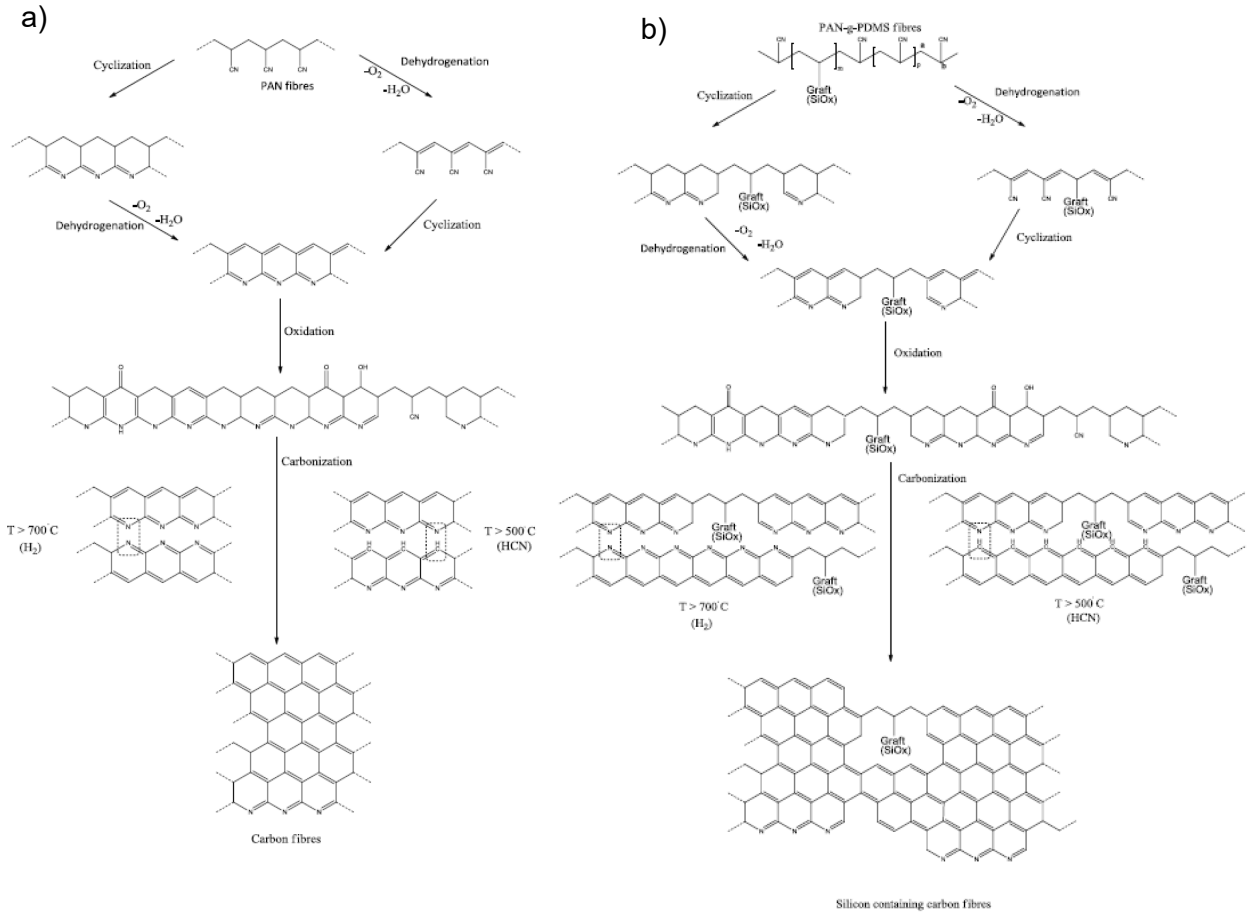

Figure 2.30: a) Carbonisation reaction process of PAN as described by Fitzer *et al*.[4] b) Carbonization reaction process of PAN-g-PDMS proposed by Human [1]

reactions take place in the PAN sections while the PDMS grafts simply do not participate in the carbonisation procedure.[1]

Studies by Camino *et al*. suggest that, during thermal treatment of PDMS in either nitrogen or air, cyclic oligomers are formed of which the larger oligomers are subsequently broken up into smaller oligomers, the smallest oligomer formed being hexamethylcyclotrisiloxane, as shown in *Figure 2.31*.[53] It was stated that the postulated degradation reactions might not be valid for PDMS containing hydroxyl terminal groups due to possible end-initiated mechanisms; only trimethylsilylated end-capped PDMS was investigated.[53] Thermal treatment in air leads to degradation products through oxygen-catalysed reactions starting at a temperature of 290 °C .[53] Thermal treatment in air led to a large amount of silica residue which was, on average, 47 % the weight of the initial PDMS sample while thermal treatment in nitrogen, starting at 400 °C, left no residue.[53] The result of thermal

treatment in air was not reproducible (variations of about 15 %) due to the fact that volatile oligomers oxidized to silica erratically precipitate onto the sample pan of the instrument.[53]

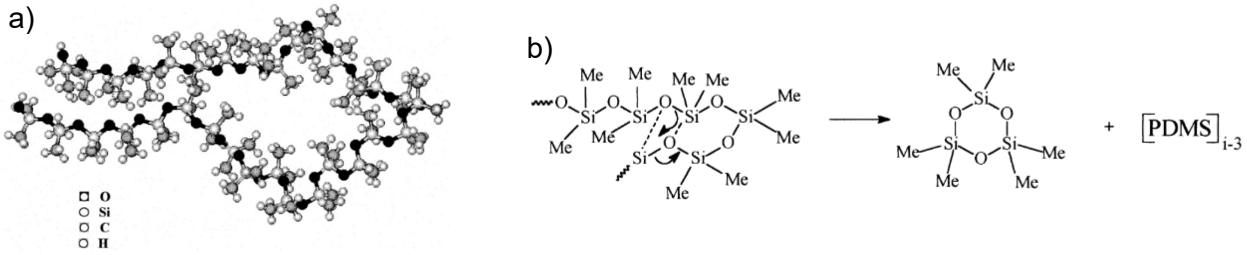

Figure 2.31: a) Computational model of PDMS (MW of 2432 g/mol) shown during the cyclic transition state leading to chain shortening and cyclic dimethylsiloxane of which b) formation of hexadimethylcyclosiloxane from PDMS gives to the smallest volatile cyclic oligomers [53]

Camino *et al*. also found that at a higher heating rate of PDMS in either nitrogen or air, a lower residual mass is observed, as seen in *Figure 2.32*.[53] This is due to the competing reactions forming either silica or volatile products that are respectively dependent on the diffusion and solubility oxygen into the sample and on the degradation and evaporation of oligomers.[53]

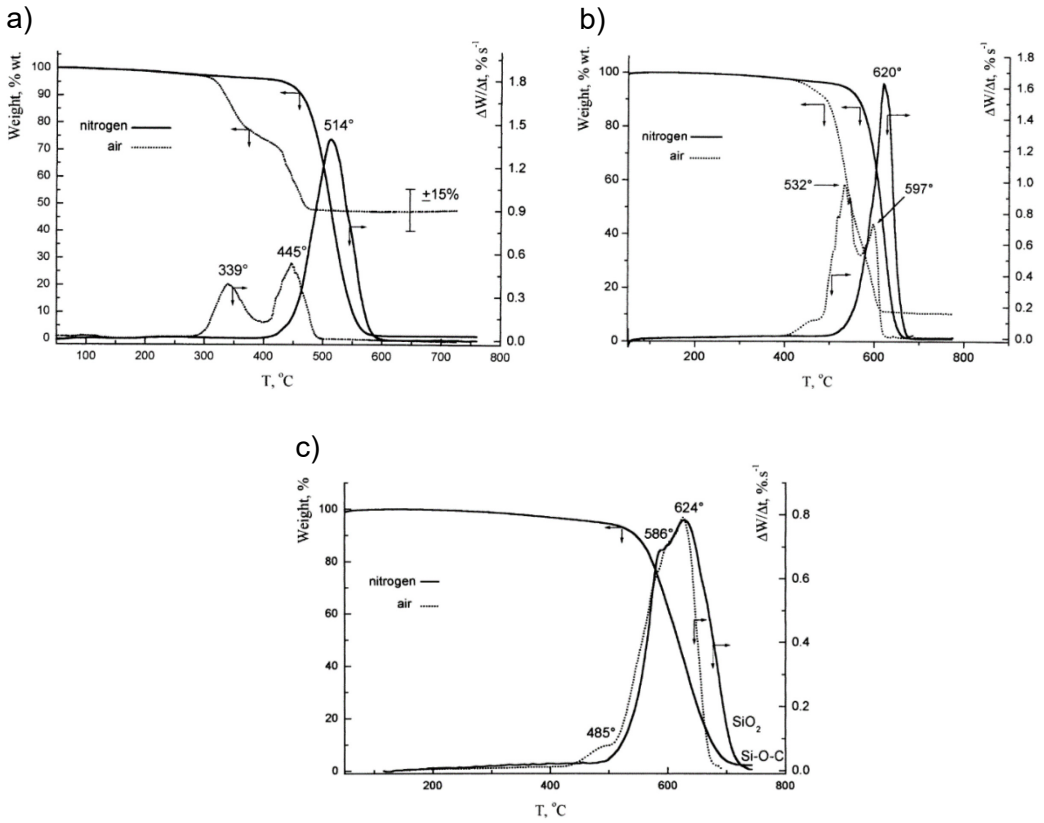

Figure 2.32: TGA heating curves of PDMS in nitrogen (solid line) and in air (dotted line) at a heating rate of a) 1 °C/min, b) 50 °C/min and c) 100 °C/min [53]

These results have some implications for the carbonisation procedure of PAN-g-PDMS nanofibers. The oxidation step is usually carried out at 300 °C in air. At this point the abovementioned reactions become apparent. It is therefore conceivable that carbon nanofibers, produced from carbonisation of precursor nanofibers consisting of PAN-g-PDMS copolymers, will contain silica phases templated

by PDMS phases in the precursor nanofibers. The schematic proposed by Human can therefore be developed further to feature silica phases imbedded in the carbon matrix. The amount of elemental silicon present might be decreased during carbonisation due to removal of volatile siloxane products. Human studied the elemental composition of PAN-g-PDMS precursor nanofibers and their subsequent carbon nanofibers. For PAN-g-PDMS precursor nanofibers containing 18.3 wt.% PDMS, nitrogen decreased from 24.8 % to 0.0 % suggesting successful carbonisation.[1] The increase in silicon from 4.6 % to 10.8 % proved to be much higher than the increase in carbon from 59.4 % to 61.3 %.[1] This indicates the formation of thermally stable silicon-based phases in the carbonised nanofibers, presumably silica phases. The heating rate employed in the thermal program used by Human was, however, quite low at a rate of 5 °C/min and had an idle stage at 300 °C in air for 2 h.[1]

According to the results published by Camino *et al*., such a heating profile should lead to a large amount of residual silica in the carbonised nanofibers. Oxidative degradation of the PDMS phases will take place yielding a large amount of silica considering the slow heating procedure. This explains the increase in silicon in the carbonised nanofibers compared to the increase in carbon.

References

1. Human, C. Facile method for producing silicon containing porous carbon nanofibres from amphiphilic copolymers and controlling precursor fibre morphology, MSc Thesis. (Stellenbosch University, 2015).
2. Bayley, G. M. & Mallon, P. E. Porous microfibers by the electrospinning of amphiphilic graft copolymer solutions with multi-walled carbon nanotubes. *Polym. (United Kingdom)* **53**, 5523–5539 (2012).
3. Tai, M. H., Tan, B. Y. L., Juay, J., Sun, D. D. & Leckie, J. O. A Self-Assembled Superhydrophobic Electrospun Carbon-Silica Nanofiber Sponge for Selective Removal and Recovery of Oils and Organic Solvents. *Chem. - A Eur. J.* **21**, 5395–5402 (2015).
4. Fitzer, E. *et al. Ullmann's Encyclopeida of Industrial Chemistry*. (Wiley-VCH Verlag GmbH & Co. KGaA, 2011).
5. Avilés, M. A. *et al.* Thermal analysis of acrylonitrile polymerization and cyclization in the presence of N,N-dimethylformamide. *J. Therm. Anal. Calorim.* **67**, 177–188 (2002).
6. Rodríguez-Hernández, J., Chécot, F., Gnanou, Y. & Lecommandoux, S. Toward 'smart' nano-objects by self-assembly of block copolymers in solution. *Prog. Polym. Sci.* **30**, 691–724 (2005).
7. Song, C. *et al.* Preparation of thermo-responsive graft copolymer by using a novel macro-RAFT agent and its application for drug delivery. *Mater. Sci. Eng. C* **62**, 45–52 (2016).
8. Kikuchi, A. & Nose, T. Unimolecular Micelle Formation of Poly(methyl methacrylate)-*graft*-polystyrene in Mixed Selective Solvents of Acetonitrile/Acetoacetic Acid Ethyl Ether. *Macromolecules* **29**, 6770–6777 (1996).
9. Basson, N. Free volume of electrospun organic-inorganic copolymers, MSc Thesis. (Stellenbosch University, 2014).
10. Bayley, G. M. Synthesis and characterisation of organic-inorganic hybrid block copolymers of polydimethylsiloxane and polystyrene, MSc Thesis. (Stellenbosch University, 2007).
11. Wagenaar, S. The synthesis and characterization of films and nanofibres from novel poly(N,N' -dimethyl acrylamide)-graft-poly(dimethyl siloxane) amphiphilic hydrogels, MSc Thesis. (Stellenbosch University, 2016).
12. Siebert, P. Electrospun carbon nanotube filled composite nanofibers by non-covalent compatibilization, MSc Thesis. (Stellenbosch University, 2016).
13. Ma, L. *et al.* Synthesis and characterization of polymer grafted graphene oxide sheets using a Ce(IV)/HNO_3 redox system in an aqueous solution. *Carbon N. Y.* **53**, 269–276 (2013).
14. Gao, H. & Matyjaszewski, K. Synthesis of Molecular Brushes by 'Grafting onto' Method: Combination of ATRP and Click Reactions. *J. Am. Chem. Soc.* **129**, 6633–6639 (2007).
15. Lien, Y. & Wu, T. Preparation and characterization of thermosensitive polymers grafted onto

silica-coated iron oxide nanoparticles. *J. Colloid Interface Sci.* **326**, 517–521 (2008).

16. Catta Preta, I. F. *et al.* Thermal behavior of polyacrylonitrile polymers synthesized under different conditions and comonomer compositions. *J. Therm. Anal. Calorim.* **87**, 657–659 (2007).
17. Jamil, S. N. A., Daik, R. & Ahmad, I. Redox Synthesis and Thermal Behavior of Acrylonitrile-Methyl Acrylate-Fumaronitrile Terpolymer as Precursor for Carbon Fiber. *Int. J. Chem. Eng. Appl.* **3**, 416–420 (2012).
18. Ramakrishna, S. *et al.* Electrospun nanofibers: solving global issues. *Mater. Today* **9**, 40–50 (2006).
19. Shenoy, S. L., Bates, W. D., Frisch, H. L. & Wnek, G. E. Role of chain entanglements on fiber formation during electrospinning of polymer solutions: good solvent, non-specific polymer-polymer interaction limit. *Polymer (Guildf).* **46**, 3372–3384 (2005).
20. Liu, W., Zhu, L., Huang, C. & Jin, X. Direct Electrospinning of Ultrafine Fibers with Interconnected Macropores Enabled by in Situ Mixing Microfluidics. *ACS Appl. Mater. Interfaces* **8**, 34870–34878 (2016).
21. Zhang, Z. *et al.* Polyacrylonitrile and Carbon Nanofibers with Controllable Nanoporous Structures by Electrospinning. *Macromol. Mater. Eng.* **294**, 673–678 (2009).
22. Eom, Y. & Kim, B. C. Solubility parameter-based analysis of polyacrylonitrile solutions in N,N-dimethyl formamide and dimethyl sulfoxide. *Polym. (United Kingdom)* **55**, 2570–2577 (2014).
23. Sahoo, S. K., Agarwal, K., Singh, A. K., Polke, B. G. & Raha, K. C. Characterization of γ- and α-Fe_2O_3 nano powders synthesized by emulsion precipitation-calcination route and rheological behaviour of α-Fe_2O_3. *Int. J. Eng. Sci. Technol.* **2**, 118–126 (2010).
24. Vidal-Vidal, J., Rivas, J. & López-Quintela, M. A. Synthesis of monodisperse maghemite nanoparticles by the microemulsion method. *Colloids Surfaces A Physicochem. Eng. Asp.* **288**, 44–51 (2006).
25. Wu, W., He, Q. & Jiang, C. Magnetic Iron Oxide Nanoparticles: Synthesis and Surface Functionalization Strategies. *Nanoscale Res. Lett.* **3**, 397–415 (2008).
26. Park, J. *et al.* One-Nanometer-Scale Size-Controlled Synthesis of Monodisperse Magnetic Iron Oxide Nanoparticles. *Angew. Chemie - Int. Ed.* **44**, 2872–2877 (2005).
27. Simeonidis, K. *et al.* Controlled synthesis and phase characterization of Fe-based nanoparticles obtained by thermal decomposition. *J. Magn. Magn. Mater.* **316**, e1–e4 (2007).
28. Hyeon, T., Lee, S. S., Park, J., Chung, Y. & Na, H. B. Synthesis of Highly Crystalline and Monodisperse Maghemite Nanocrystallites without a Size- Selection Process. *J. Am. Chem. Soc.* **123**, 12789–12801 (2001).
29. Woo, K. *et al.* Easy Synthesis and Magnetic Properties of Iron Oxide Nanoparticles. *Chem. Mater.* **16**, 2814–2818 (2004).
30. Bumb, A. *et al.* Synthesis and characterization of ultra-small superparamagnetic iron oxide nanoparticles thinly coated with silica. *Nanotechnology* **19**, 335601 (2008).

31. Kim, D. K., Zhang, Y., Voit, W., Rao, K. V. & Muhammed, M. Synthesis and characterization of surfactant-coated superparamagnetic monodispersed iron oxide nanoparticles. *J. Magn. Magn. Mater.* **225**, 30–36 (2001).
32. Sun, Y., Ma, M., Zhang, Y. & Gu, N. Synthesis of nanometer-size maghemite particles from magnetite. *Colloids Surfaces A Physicochem. Eng. Asp.* **245**, 15–19 (2004).
33. Shen, L., Laibinis, P. E. & Hatton, T. A. Bilayer Surfactant Stabilized Magnetic Fluids: Synthesis and Interactions at Interfaces. *Langmuir* **15**, 447–453 (1999).
34. Fortuin, L. Modified chitosan nano-substrates for mycobacterial capture, MSc Thesis. (Stellenbosch University, 2015).
35. Lakay, E. M. Superparamagnetic iron-oxide based nanoparticles for the separation and recovery of precious metals from solution, MSc Thesis. (Stellenbosch University, 2009).
36. Ziolo, R. F. *et al.* Matrix-Mediated Synthesis of Nanocrystalline γ-Fe_2O_3: A New Optically Transparent Magnetic Material. *Science (80-.).* **257**, 219–223 (1992).
37. Schnepp, Z., Wimbush, S. C., Antonietti, M. & Giordano, C. Synthesis of Highly Magnetic Iron Carbide Nanoparticles via a Biopolymer Route. *Chem. Mater.* **22**, 5340–5344 (2010).
38. Wojcik, M., Chmist, J., Przewoznik, J., Figiel, H. & Blazewicz, S. Magnetic properties of PAN-based carbon fibres modified with magnetite nanoparticles. *Carbon N. Y.* **50**, 1604–1613 (2012).
39. Stöber, W., Fink, A. & Bohn, E. Controlled Growth of Monodisperse Silica Spheres in the Micron Size Range. *J. Colloid Interface Sci.* **26**, 62–69 (1968).
40. Beganskienė, A., Sirutkaitis, V., Kurtinaitienė, M., Juškėnas, R. & Kareiva, A. FTIR, TEM and NMR Investigations of Stöber Silica Nanoparticles. *Mater. Sci.* **10**, 287–290 (2004).
41. Ibrahim, I. A. M., Zikry, A. A. F. & Sharaf, M. A. Preparation of spherical silica nanoparticles: Stober silica. *J. Am. Sci.* **6**, 985–989 (2010).
42. Deng, Y. H., Wang, C., Hu, J., Yang, W. & Fu, S. Investigation of formation of silica-coated magnetite nanoparticles via sol-gel approach. *Colloids Surfaces A Physicochem. Eng. Asp.* **262**, 87–93 (2005).
43. Tadyszak, K. *et al.* Spectroscopic and magnetic studies of highly dispersible superparamagnetic silica coated magnetite nanoparticles. *J. Magn. Magn. Mater.* **433**, 254–261 (2017).
44. Li, Z. & Zhu, Y. Surface-modification of SiO_2 nanoparticles with oleic acid. *Appl. Surf. Sci.* **211**, 315–320 (2003).
45. White, L. D. & Tripp, C. P. Reaction of (3-Aminopropyl)dimethylethoxysilane with Amine Catalysts on Silica Surfaces. *J. Colloid Interface Sci.* **232**, 400–407 (2000).
46. Bini, R. A., Marques, R. F. C., Santos, F. J., Chaker, J. A. & Jafelicci, M. Synthesis and functionalization of magnetite nanoparticles with different amino-functional alkoxysilanes. *J. Magn. Magn. Mater.* **324**, 534–539 (2012).
47. Verwey, E. J. W. Theory of the stability of lyophobic colloids. *J. Phys. Colloid Chem.* **51**, 631–

636 (1947).

48. Mackay, M. E. *et al.* General Strategies for Nanoparticle Dispersion. *Science (80-.).* **311**, 1740–1743 (2006).
49. Liu, J., Gao, Y., Cao, D., Zhang, L. & Guo, Z. Nanoparticle Dispersion and Aggregation in Polymer Nanocomposites: Insights from Molecular Dynamics Simulation. *Langmuir* **27**, 7926–7933 (2011).
50. Zhang, Y., Chen, Y., Westerhoff, P., Hristovski, K. & Crittenden, J. C. Stability of commercial metal oxide nanoparticles in water. *Water Res.* **42**, 2204–2212 (2008).
51. Zhu, J. *et al.* Magnetic polyacrylonitrile-Fe@FeO nanocomposite fibers - Electrospinning, stabilization and carbonization. *Polymer (Guildf).* **52**, 2947–2955 (2011).
52. Panels, J. E. *et al.* Synthesis and characterization of magnetically active carbon nanofiber/iron oxide composites with hierarchical pore structures. *Nanotechnology* **19**, 455612 (2008).
53. Camino, G., Lomakin, S. M. & Lazzari, M. Polydimethylsiloxane thermal degradation Part 1. Kinetic aspects. *Polymer (Guildf).* **42**, 2395–2402 (2001).

Chapter 3: Experimental Procedures

Procedures related to polymer and nanoparticle synthesis, electrospinning, carbonization and characterization are outlined in detail. Some variable parameters are omitted and reported alongside their affected results in *Chapter 4.*

3.1. Purification of chemicals

3.1.1. Purification of acrylonitrile

Acrylonitrile (Sigma Aldrich, >99%) was received containing 35-45 ppm MEHQ as radical inhibitor. The radical inhibitor was removed by passing the monomer through a MEHQ removal column twice. The monomer was then distilled at 45 °C under stirring at 450 r.p.m. and a vacuum of approximately 250 hPa using a Heidolph MR3001K magnetic stirrer and hotplate, a Vacuubrand DVR2 vacuum gauge and an Edwards membrane vacuum pump.

3.1.2. Purification of AIBN

AIBN (98 % purity) was received from Sigma Aldrich and further purified by recrystallization. 5 g of AIBN was added to 80 mL methanol and heated to 40 °C under stirring until dissolved. More AIBN was added until the added powder took more than one minute to dissolve. The solution was then removed from heat and vacuum filtered. The filtrate containing dissolved AIBN was placed in a refrigerator. Recrystallization took place during cooling. After about 30 min of cooling, the recrystallized AIBN was vacuum filtered and washed with cold methanol. The obtained powder was dried in a vacuum oven at room temperature for 24 h and subsequently stored in a sealed container in a freezer.

3.1.3. Purification of solvents

DMF used for polymerization reactions was distilled and stored in sealed bottles over >10 wt.% 4 Å molecular sieves (mass relative to amount of solvent) for at least 24 hrs prior to use.

Benzene was received in >99.0 % purity and used as-received to avoid distillation since benzene is a toxic and carcinogenic substance.

Ethanol was distilled and used without drying. Drying of ethanol, successively used in a reaction employing a 70:30 v/v ethanol:water ratio, would be redundant. It has been reported that, after storage in open air, ethanol contained a total of 1428 ppm water.[1] Considering the solvent ratio and amount of water absorbed from the air, the deviation from the reported solvent ratio is very small, roughly 0.1 %, if drying is omitted. This minute difference has a negligible effect on the product of the reaction performed; a much greater difference in ethanol:water ratio is required to impose a notable effect.[2]

18 MΩ.cm water from an Elga Purelab Option-Q purification instrument was used.

3.2. Polymerization reactions

3.2.1. Conventional free radical PAN homopolymer synthesis

The reaction scheme for the homopolymerization is outlined in *Scheme 3.1*. The homopolymer was synthesized using a conventional free radical polymerization method in a precipitation reaction following methods reported in the literature.[3,4] The solvent mixture used was DMF:toluene in a 8:92

weight ratio. This ratio was used to ensure that the monomer was miscible and the polymer insoluble in the solvent mixture. The monomer was added in a monomer:solvent 15:85 weight ratio. 0.1 wt.% AIBN was used as a thermal initiator. The reaction was carried out in a 250 mL round bottom flask under stirring at 150 r.p.m. while heated to 70 °C. The monomer and about 90 % (v/v) of the solvent mixture was added to the 250 mL round bottom flask along with a magnetic stirrer bar after which the flask was sealed with a septum and degassed with nitrogen for 30 min. Simultaneously a 50 mL round bottom flask sealed with a septum was used to bubble the remainder of the solvent mixture containing the required amount of AIBN with nitrogen for 30 min. The AIBN solution was transferred to the reaction flask using a degassed syringe and needle. The reaction mixture was further bubbled with nitrogen for another 15 min after which it was added to the oil bath at 70 °C. The reaction was run for 48 h. The septum was removed and the synthesized polymer was fully precipitated by decanting the reaction mixture into rapidly stirring methanol. The precipitated polymer powder was vacuum filtered and dried in a vacuum oven at room temperature for 72 h.

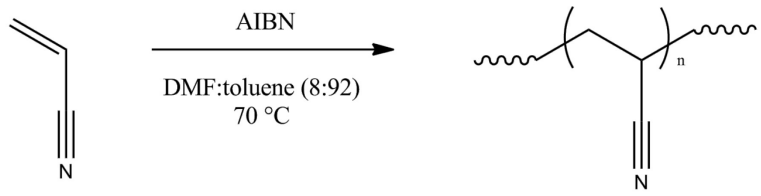

Scheme 3.1: Conventional free radical homopolymerization of acrylonitrile

3.2.2. Conventional free radical PAN-g-PDMS copolymer synthesis

The reaction scheme for the copolymerization is outlined in *Scheme 3.2*. The PDMS macromonomers used, monomethacryloxypropyl-terminated polydimethylsiloxane, was received from Gelest Inc. and used as-is due to the non-volatile nature that prevents distillation. The copolymer was synthesized using a conventional free radical method in a precipitation reaction. The solvent mixture used was DMF:benzene in an 8:92 weight ratio. This ratio was used to ensure that both the monomer and the macromonomer was miscible and the polymer insoluble in the solvent mixture. The monomer was added in a monomer:solvent weight ratio of 15:85. 0.1 wt.% AIBN was used as a thermal initiator unless stated otherwise. The reaction was carried out in a 100 mL round bottom flask under stirring at 150 r.p.m. while heated to 70 °C. The monomers and about 90 % (v/v) of the solvent mixture was added to the 100 mL round bottom flask along with a magnetic stirrer bar after which the flask was sealed with a septum and degassed with nitrogen for 30 min. Simultaneously, a 50 mL round bottom flask sealed with a septum was used to bubble the remainder of the solvent mixture containing the required amount of AIBN with nitrogen for 30 min. The AIBN solution was transferred to the reaction flask using a degassed syringe and needle. The reaction mixture was further bubbled with nitrogen for another 15 min after which it was added to the oil bath at 70 °C. The reaction was run for 48 h. The septum was removed and the synthesized polymer was fully precipitated by decanting the reaction mixture into rapidly stirring methanol. An extraction of

unreacted PDMS macromonomers and homoPDMS formed by the macromonomers was carried out by adding the powder to hexane and stirring the mixture at 500 r.p.m. for 48 h. PDMS macromonomers and homoPDMS are soluble in hexane and will be removed from the precipitated powder during the hexane extraction procedure. The precipitated polymer powder was vacuum filtered and dried in a vacuum oven at room temperature for 72 h.

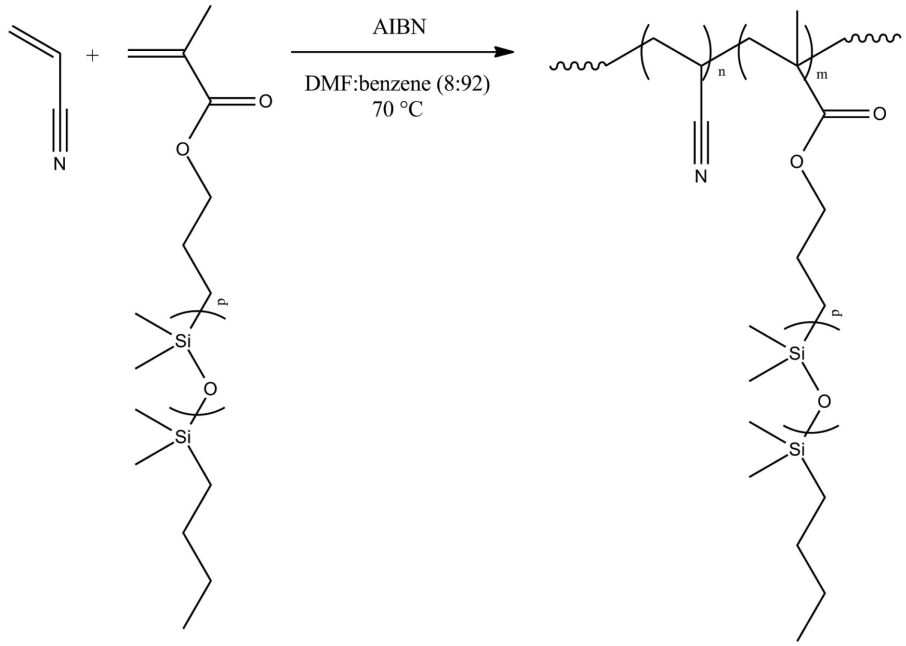

Scheme 3.2: Reaction scheme of conventional free radical copolymerization of acrylonitrile and PDMS macromonomers

3.3. Nanoparticle reactions

3.3.1. Co-precipitation of iron oxide nanoparticles

Ferrous chloride and ferric chloride were used as precursors in an aqueous medium with ammonia as the precipitating agent in a co-precipitation process.

Nitrogen was bubbled in the solution throughout the procedure. 340 mL distilled water was added to a three-neck round bottom flask and bubbled for 30 min while heating to 80 °C. 8 g $FeCl_3 \cdot 6H_2O$ and 3 g $FeCl_2 \cdot 4H_2O$ was added to the water and bubbled for 30 min while dissolving at 80 °C. Simultaneously, 60 mL of 25 % ammonium hydroxide was bubbled for 30 min in a dripping funnel attached to the round bottom flask. The ammonium hydroxide solution was rapidly added to the reaction mixture. The reaction was run for 40 min at 80 °C under stirring at 700 r.p.m. and a constant nitrogen purge. During the co-precipitation process, a solution of citric acid monohydrate in water (6 g in 50 mL) was added to the overhead dripping funnel and bubbled for 20 min during the latter half of the co-precipitation period. After the co-precipitation process, the reaction flask was removed from the heat and allowed to cool for 5 min after which the citric acid solution was added in a fast but dropwise fashion to the as-synthesized iron oxide nanoparticle dispersion. Stirring was continued for 20 min at 700 r.p.m. under constant nitrogen purge. Stirring and nitrogen purge was ceased and the reaction mixture was decanted into 2 L of acetone to precipitate the nanoparticles. A dark fluid was

observed at the bottom of the flask which, upon closer inspection during slow stirring, appeared to be a very dark shade of green. This is presumably due to ferrous iron forming under the prevalent conditions of pH and solvent composition. Magnetically-assisted decantation was carried out to remove the bulk of the acetone-water mixture giving a magnetic fluid. The magnetic fluid was dialysed in water using a dialysis tube with a 3500 molecular weight cut-off. The water was replaced every 1.5 h for the first 6 h followed by another 18 h of dialysis. After dialysis, a dark magnetic fluid was obtained and stored in an airtight container. The concentration of the nanoparticles in the water-based magnetic fluid was determined by weighing three aliquots before and after the removal of the water in a vacuum oven. The dried powder of the aliquots was black and could easily be re-dispersed in water.

3.3.2. Silica coating of iron oxide nanoparticles

A procedure based on the Stöber method was followed to coat the IONPs with a silica shell.[5] A predetermined amount of the magnetic fluid, based on its concentration and the amount of IONPs required in the reaction, was added to a 2 L Erlenmeyer flask along with an appropriate amount of water and ethanol to obtain a 1:2.3 v/v ratio. This ratio is used due to the fact that the nanoparticles are well-dispersed in water while TEOS is miscible with ethanol.[2] Ammonia solution ($NH_4OH_{(aq)}$, 25% in water) was added to a final concentration of 0.15 M according to literature recommendations.[2] The required amount of TEOS was added dropwise over a period of 5 min under stirring at 700 r.p.m. The reaction was run for 24 h. The reaction mixture was added to an equal volume of hexane to remove unreacted TEOS which is miscible with hexane. The dark-brown water-ethanol phase containing the silica-coated nanoparticles was isolated in a separating funnel. The resultant magnetic fluid was left in a fumehood for 48 h to evaporate most of the solvent after which the silica-coated IONP powder was placed in a vacuum oven at room temperature for 48 h. The dried product was a dark-brown colour.

3.4. Electrospinning

Electrospinning was carried out on an in-house built setup shown in *Figure 3.1*. Pure polymer electrospinning solutions were prepared as follows: DMF was added to the polymer powder along with a magnetic stirrer bar, placed in a heat bath at 50 °C and at a stirring rate of 125 r.p.m. for 1 h. Thereafter, the polymer solution was sonicated for 1 h to remove any air bubbles formed during the dissolution process. Polymer-nanoparticle electrospinning solutions were prepared as follows: DMF was added to the nanoparticles and sonicated for 20 min after which the nanoparticle dispersion was added to the polymer powder along with a magnetic stirrer bar. As in the case of the pure polymer solutions, the solution was prepared in a heat bath at 50 °C and at a stirring rate of 125 r.p.m. for 1 h followed by sonication for 1 h. A Harvard Apparatus Pump 33 syringe pump and a home-built high voltage power supply with the positive electrode attached to the needle and the negative electrode attached to the collector plate were used. A 1 mL Avacare Luer-slip syringe was used as a polymer

solution pool while a connected Sterican 0.8 × 22 mm blunt-nosed needle acted as a spinneret. Humidity was controlled using a AOTE CFZ-20 dehumidifier. Electrospinning was carried out only when the relative humidity was below 45 %. The flow rate, applied voltage and tip-to-collector distance (TCD) for each electrospun fiber mat is reported along with the results.

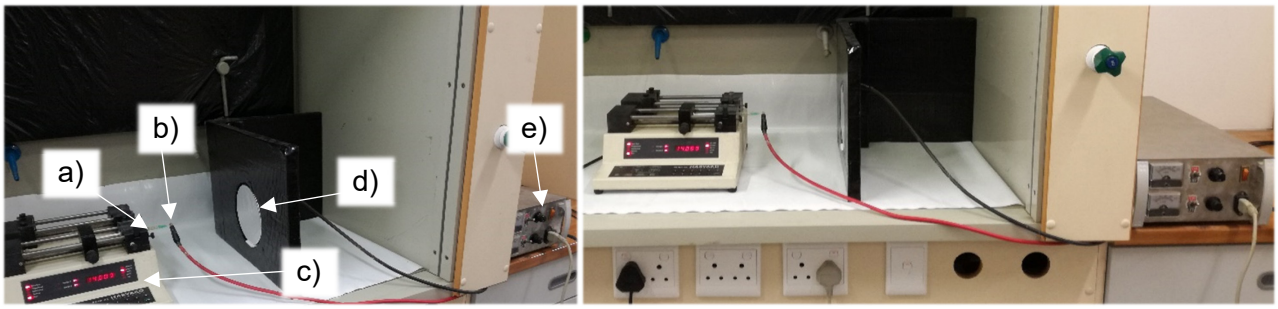

Figure 3.1: Digital photos of electrospinning setup comprised of a a) syringe and b) needle as spinneret attached to a c) solution pump, a d) collector plate and a e) high-voltage power supply with the positive electrode (red wire) connected to the spinneret and the negative electrode connected to the collector plate

3.5. Carbonisation

Carbonisation was done in a Carbolite GHC 12/450 modular horizontal tube furnace equipped with an Eurotherm Type 3216 P1 temperature controller shown in *Figure 3.2*. Baseline grade argon gas with a purity of 5.0, supplied by Afrox, was fed directly into the furnace to provide inert conditions required after the isothermal stage at 300 °C.

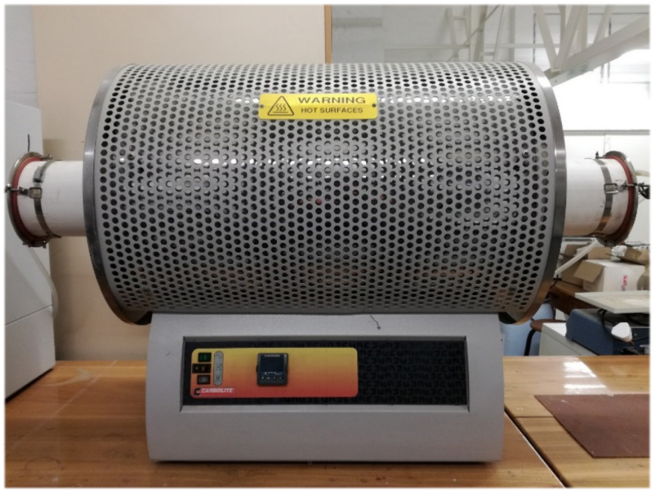

Figure 3.2: Digital photo of Carbolite tubular furnace equipped with an Eurotherm temperature controller used for carbonisation

The temperature program employed was as follows:

1. Ramp from room temperature to 300 °C at 5 °C /min under atmospheric air
2. Isothermal stage at 300 °C for 2 h under atmospheric air
3. Isothermal stage at 300 °C for 20 min under argon flush

4. Ramp to 800 °C at 5 °C /min under argon flush
5. Isothermal stage at 800 °C for 2 h under argon flush
6. Cooling under ambient conditions to room temperature under argon flush.

3.6. Characterization

3.6.1. Size Exclusion Chromatography (SEC)

SEC was performed using dimethylacetamide (DMAc) as a solvent. A Waters 1515 isocratic HPLC pump, a Waters 717plus auto-sampler and a Waters 600E system controller were operated by Breeze Version 3.30 SPA software employed in the experiments. PMMA calibration standards were used: the obtained results are therefore reported as PMMA equivalents. The analysis was run at 40 °C using an injection volume of 100 µl. Samples were prepared by dissolving polymers in HPLC grade DMAc (purity of >99.9 %) at a concentration of 2 mg/mL followed by filtration through an Acrodisc syringe filter containing a 0.45 µm GHP membrane using a glass syringe.

3.6.2. ^{1}H NMR spectroscopy

A Varian VXR Unity 300 MHz NMR instrument was used for ^{1}H NMR. PAN homopolymer and PAN-g-PDMS copolymers were run in DMSO-d_6 while the PDMS macromonomers were were run in chloroform-*d* all at a concentration of approximately 2 wt.%. The polymer solutions were dissolved overnight. Analysis was done at 25 °C.

3.6.3. Differential Scanning Calorimetry (DSC)

DSC experiments were done on a TA Instruments Q100 machine. TA Instruments Universal Analysis 2000 Version 4.1.0.16 software was used to run experiments and perform data analysis. Samples weighing 4-6 mg were placed in aluminum pans with lids. The thermal procedure entailed cooling to 0 °C followed by heating at a rate of 10 °C /min to 300 °C. Since the thermal process of interest is an exothermic reaction and not a physical process, only one heating cycle was required.

3.6.4. Attenuated Total Reflectance Fourier-Transform Infrared spectroscopy (ATR-FTIR)

ATR-FTIR was done on a Thermo Fischer Nicolet iS10 Smart iTR instrument. Solid powders and fibers were analysed as-is without any sample preparation. Omnic software was used to run experiments, record data and do a baseline correction for each sample spectrum. A background spectrum was run prior to every sample spectrum. All spectra were compiled by an accumulation of 64 successive spectra at a resolution of 4 cm^{-1} over a range of 600-4000 cm^{-1}.

3.6.5. Wide-Angle X-ray Diffraction (WAXD)

WAXD was done on fine powders after grinding for about 10 min. The instrument used was a Bruker AXS D2 Phaser diffractometer equipped with a Cu source. An X-ray generation of 30 kV and 10 mA was used with a sample rotation of 30 r.p.m. A diffraction pattern was recorded from 4 to 80 2θ at

increments of 0.02 and a recording time of 0.5 s. DIFFRAC.SUITE software was used to run experiments and record the data. A baseline correction was performed using Origin Pro 9.0 software.

3.6.6. Scanning electron microscopy (SEM)

SEM was performed on a Carl Zeiss Gemini 2 MERLIN Field Emission Scanning Electron Microscope (FE-SEM) instrument. Samples were placed on metallic sample stubs covered with carbon tape and gold coated using an Edwards S150A sputter coater. Images used for fiber diameter measurements as well as all images presented were taken in the secondary electron high resolution mode of detection, usually at an electron acceleration of 5 kV and an electron current of 250 pA. Fiber diameter measurements were done fibers using AxioVision release 4.4 software. At least 50 fibers were measured.

3.6.7. Scanning Transmission Electron Microscopy (STEM)

STEM was performed on the same instrument as SEM. Copper grids covered with carbon film were used as supports. Nanofibers were wet with water (a non-solvent for PAN), placed on copper grids and dried in air. Imaging was done at an electron acceleration of 20 kV and an electron current of 250 pA.

3.6.8. Transmission Electron Microscopy (TEM)

TEM was performed on a FEI/Tecnai T20 instrument. Sample preparation was similar to that of STEM analysis: copper grids covered with carbon film were used as supports for the samples. Nanoparticle samples were prepared by sonication of a nanoparticle dispersion of less than 1 % (g/mL) in water for 20 min after which a single droplet was placed on the copper grid and dried in air. Nanofiber samples were prepared as with STEM imaging. Imaging was done at an electron acceleration of 200 kV and an electron current of 250 pA. Particle diameter measurements were done using AxioVision release 4.4 software. At least 125 particles were measured.

3.6.9. Dynamic Light Scattering (DLS)

DLS size and zeta potential measurements were done on a Zetasizer Nano ZS90. Nanoparticles were prepared in water at a concentration of 1 % (g/L) and sonicated for 20 min. All measurements were done in triplicate. Polystyrene cuvettes were used.

3.6.10. Sorption capacity study

The sorption capacity of fiber membranes was tested by soaking a pre-weighed section of the membrane in the tested liquid for 1 min after which the wet membrane was dabbed on a piece of paper towel to remove liquid on the surfaces and weighed. To regain sorption capacity by removing the absorbed liquid, the membrane was immersed in hexane for 3 min followed by drying at 120 °C for 2 h. The same membrane was tested 5 times to investigate recyclability.

References

1. Williams, D. B. G. & Lawton, M. Drying of Organic Solvents: Quantitative Evaluation of the Efficiency of Several Desiccants. *J. Org. Chem.* **75,** 8351–8354 (2010).
2. Deng, Y. H., Wang, C., Hu, J., Yang, W. & Fu, S. Investigation of formation of silica-coated magnetite nanoparticles via sol-gel approach. *Colloids Surfaces A Physicochem. Eng. Asp.* **262,** 87–93 (2005).
3. Human, C. Facile method for producing silicon containing porous carbon nanofibres from amphiphilic copolymers and controlling precursor fibre morphology, MSc Thesis. (Stellenbosch University, 2015).
4. Bayley, G. M. & Mallon, P. E. Porous microfibers by the electrospinning of amphiphilic graft copolymer solutions with multi-walled carbon nanotubes. *Polym. (United Kingdom)* **53,** 5523–5539 (2012).
5. Stöber, W., Fink, A. & Bohn, E. Controlled Growth of Monodisperse Silica Spheres in the Micron Size Range. *J. Colloid Interface Sci.* **26,** 62–69 (1968).

Results and Discussion

Experimental results of the project are presented and discussed in detail.

4.1 Synthesis of PAN-g-PDMS copolymer precursors

Table 4.1 shows results of the analysis of copolymerization reactions involving 1 kDa PDMS grafts.

Table 4.1:

PDMS graft incorporation, reaction yield, number average molar mass (M_n) and molar mass dispersity *Đ* of copolymers synthesized using various 1 kDa PDMS macromonomer feeds

PDMS feed (wt.%)	[a]PDMS incorporation (wt.%)	[b]Percentage yield (wt.%)	[c]M_n (× 10^5 g/mol)	Molar mass dispersity, *Đ*
5	3.9	49.7	1.59	2.0
5	3.7	53.0	1.88	2.1
10	9.6	37.1	1.16	2.3
10	8.4	39.6	1.62	1.9
15	15.2	29.5	1.38	2.2
15	13.5	36.3	1.35	1.9
20	20.8	32.6	1.03	2.7
20	18.5	33.0	1.27	1.8

[a]Determined by ^{1}H NMR spectroscopy
[b]Determined gravimetrically
[c]Determined by SEC w.r.t. linear PMMA calibration standards

The copolymerization reactions employing the 1 kDa PDMS macromonomers were done in duplicate to verify the validity of the gravimetric results that showed a relatively low reaction yield. The reaction yields did not differ significantly for the second series which proves that the first series of reactions were performed successfully. Small differences are seen in PDMS graft content as well as reaction yields. It appears that a slight decrease in the PDMS graft incorporation corresponds to a slight increase in the reaction yield. This observation supports the hypothesis that incorporation of PDMS macromonomers impairs the rate of the copolymerization reaction.

The PAN-based copolymers were synthesised as described in the experimental section according to reaction conditions reported in literature.[1,2] The ratio of monomer to macromonomer was varied to alter the incorporation of PDMS macromonomers in the synthesised copolymer. The molar mass was analysed using size exclusion chromatography with PMMA calibration standards. Gravimetric analysis was carried out by weighing the powder product and calculating the percentage of the powder mass as a fraction of the total mass of monomers and macromonomers in the reaction feed. This was done after extraction in hexane and in vacuo drying of the filtered polymer powder. The gravimetrically determined reaction yield does not discriminate between monomer and macromonomer; it is simply the percentage of powder product w.r.t. the amount of monomer and macromonomers added. The copolymer content was determined using ^{1}H NMR. The siloxane methyl peak in the region of 0.05 ppm chemical shift, associated with incorporated PDMS

macromonomer, and the methylene peak around 2.05 ppm, associated with incorporated acrylonitrile monomer, were integrated and the ratio used to determine the mole ratio of incorporation and consequently the wt.% PDMS macromonomer incorporated. No vinyl peaks were visible in the vinyl region at a chemical shift of 4.5-6.5 ppm in any of the ^{1}H NMR spectra.[3] This suggests that, given the substantial amount of unreacted monomer and macromonomer as evidenced by gravimetric yield, the macromonomer hexane extraction and subsequent monomer evaporation processes were successful in removing any unreacted reagents from the product.

Table 4.2 shows results of the analysis of copolymerization reactions involving 5 kDa PDMS grafts.

Table 4.2:

PDMS graft incorporation, reaction yield, number average molar mass (M_n) and molar mass dispersity *Đ* of copolymers synthesized using various 5 kDa PDMS macromonomer feeds at different concentrations of thermal initiator

PDMS feed (wt.%)	[a]Thermal initiator (wt.%)	[b]PDMS incorporation (wt.%)	[c]Percentage yield (wt.%)	[d]M_n (× 10^5 g/mol)	Molar mass dispersity, *Đ*
5	0.10	2.4	47.6	1.79	2.2
5	0.15	2.4	66.3	1.54	2.6
5	0.20	2.9	75.2	1.34	2.8
10	0.10	6.5	41.0	1.25	2.2
10	0.15	4.8	64.2	1.59	2.4
10	0.20	5.8	71.8	1.28	2.7
15	0.10	8.9	33.5	1.60	2.3
15	0.15	7.7	59.6	1.47	2.5
15	0.20	8.2	68.1	1.19	2.9
20	0.10	11.6	43.6	1.37	2.5
20	0.15	11.6	57.4	1.42	2.5
20	0.20	12.0	65.8	1.30	2.7

[a]AIBN concentration w.r.t. total mass of monomer and macromonomer
[b]Determined by ^{1}H NMR spectroscopy
[c]Determined gravimetrically
[d]Determined by SEC w.r.t. linear PMMA calibration standards

The initially synthesized series of PAN-g-PDMS containing the 5 kDa PDMS grafts could not be dissolved in a 15 wt.% polymer solution. The maximum concentration attainable without gelation was 8 wt.%. This was not ideal, since the series containing 1 kDa and 10 kDa PDMS grafts could be electrospun from a 15 wt.% polymer solution into fibers but formed fibers with beads at lower concentrations. Ideally, all electrospinning should be done at the same concentration for the sake of comparison. Consequently, successive copolymerization reactions were carried out using the 5 kDa PDMS macromonomers with increasing amounts of the thermal initiator in an attempt to decrease the molar mass and thereby avoid gelation at a concentration of 15 wt.%. This attempt was based

on the preliminary assumption that the high molar mass, PDMS graft content and length of the PDMS grafts all contributed to gelation at a polymer solution concentration of 15 wt.%. The variation in initiator concentration was based on the premise that a higher concentration of initiator will lead to a higher concentration of growing chain ends. In such a case, monomer concentration will decrease more rapidly and, therefore, each growing chain will react with less monomer and macromonomers before terminating. Copolymers synthesised from copolymerizations containing 0.15 wt.% AIBN could be dissolved in a 10 wt.% polymer solution and those synthesised from copolymerizations containing 0.20 wt.% AIBN could be dissolved in a 10.5 wt.% polymer solution. After the third failed attempt at synthesizing copolymers containing 5 kDa PDMS grafts that can be dissolved in a 15 wt. % polymer solution, this endeavour was terminated. Electrospinning of PAN-g-PDMS copolymers containing 16.2 wt.% of 5 kDa PDMS graft with M_n of 1.06×10^5 g/mol at polymer solution concentrations of 10-18 wt.% in DMF has been reported for copolymers synthesized using the exact same synthetic procedure employed in the current study.[2] However, it has also been reported that a range of PAN-g-PDMS copolymers containing 3.2-17.1 wt.% of 5 kDa PDMS grafts with M_n of 14.0-0.9×10^5 g/mol, also synthesized by the same procedure used in this study, could not be electrospun even at a polymer solution concentration of 5 wt.% in DMF due to high viscosity.[4] Considering how close these reported molar masses are to each other, it is not clear why PAN-g-PDMS copolymers containing 5 kDa PDMS grafts behave very differently for the products of different reaction series while PAN-g-PDMS copolymers containing 1 kDa and 10 kDa PDMS grafts can be electrospun.

The effect of an increase in initiator concentration on the gravimetric yield is clear from *Table 4.2*: a higher amount of initiator leads to a higher gravimetric yield. This is seen for all the PDMS macromonomer feed ratios. It is not an unexpected result, since there are more growing chains present if a larger amount of initiator is used. At a higher concentration of initiator, the concentration of radicals will be higher when steady state is reached w.r.t. initiation and termination of growing chains. A larger amount of growing chains will ultimately react with more monomers and macromonomers and thereby increase the reaction yield. It is clear that the variation in initiator used does not affect the PDMS macromonomer incorporation.

Table 4.3 shows results of the analysis of copolymerization reactions involving 10 kDa PDMS grafts.

Table 4.3:

PDMS graft incorporation, reaction yield, number average molar mass (M_n) and molar mass dispersity *Đ* of copolymers synthesized using various 10 kDa PDMS macromonomer feeds

PDMS feed (wt.%)	[a]PDMS incorporation (wt.%)	[b]Percentage yield (wt.%)	[c]M_n (× 10^5 g/mol)	Molar mass dispersity, *Đ*
5	1.2	59.6	1.43	2.0
10	2.6	50.5	1.13	1.9
15	5.7	35.4	1.08	1.8
20	8.5	41.8	1.01	1.7

[a]Determined by ^{1}H NMR spectroscopy
[b]Determined gravimetrically
[c]Determined by SEC w.r.t. linear PMMA calibration standards

Considering *Table 4.1, Table 4.*2 and *Table 4.*3, there is no clear trend w.r.t. the molar masses for all the synthesised polymers. The molar mass dispersity, *Đ*, ranges from 1.6 to 2.9. Conventional free radical polymerization reactions offer very little control in terms of molar mass and thus this result is to be expected. SEC data was reported as being relative to linear PMMA calibration standards. The PDMS grafts also act as branching points in the polymer while adding an additional chemical constituent. The difference in chemical composition between the PAN sections and PDMS sections lead to different solubilities in the solvent, in this case DMAc, used for elution which will affect the solution behavior and hydrodynamic volume of the copolymers in solution. The reported molar mass must, therefore, be interpreted only as the hydrodynamic volume of the analysed polymer equal to that of the linear PMMA reported and not as the absolute molar mass of the synthesized copolymers.

Clear trends are seen with an increase in the PDMS feed ratio. For all series of PDMS macromonomers, a higher PDMS feed produced a higher PDMS incorporation as observed by ^{1}H NMR measurements. This was accompanied by a trend of decreasing reaction yield for a larger PDMS feed as determined by gravimetric analysis. During free radical copolymerization, a radical can be stabilized more effectively on the reactive tertiary carbon of PDMS macromonomers than on the reactive secondary carbon of acrylonitrile monomers. Based on this consideration alone, a conclusion might be drawn that the PDMS macromonomers are more reactive than acrylonitrile monomers. However, solubility and steric effects will play a role in reaction kinetics. The reported solvent mixture was employed in order to solubilize both the monomer and the macromonomer and thereby yield good incorporation of the macromonomers.[5] The PDMS macromonomers, containing flexible PDMS chains, will assume various coil-like solution conformations that will cause the reactive vinyl group to be less accessible for reaction than in the case of a low molar mass monomer such as acrylonitrile. These effects can subdue the stabilizing effects of the reactive tertiary carbon and thereby reduce the reactivity of the PDMS macromonomers to below that of acrylonitrile. A higher

feed of PDMS macromonomer, yielding higher incorporation, leads to a lower reaction yield. This result suggests that the PDMS macromonomers are less reactive than the acrylonitrile monomers under the current reaction conditions. The lower reactivity of the PDMS macromonomers will impair the rate of the copolymerization reaction compared to that of an acrylonitrile homopolymerization reaction and thereby lead to a lower reaction yield. The reaction time could be increased in an attempt to increase reaction yield but increasing viscosity due to polymer precipitation will gradually restrict mobility of the monomers and macromonomers and subsequently diminish the rate of polymerization.

There is no clear trend in terms of reaction yield w.r.t. chain length of the PDMS macromonomers used. Even though a larger macromonomer might be less reactive due to the reasons discussed above, a smaller molar amount of macromonomers are present in a reaction employing a larger macromonomer provided that the mass of the macromonomer in the feed remains constant. Therefore, the effect of having a less reactive chain-end is offset by the lower amount of said chain-ends.

Figure 4.1 shows the PDMS incorporation as a function of the PDMS macromonomer feed ratio along with the associated trendlines.

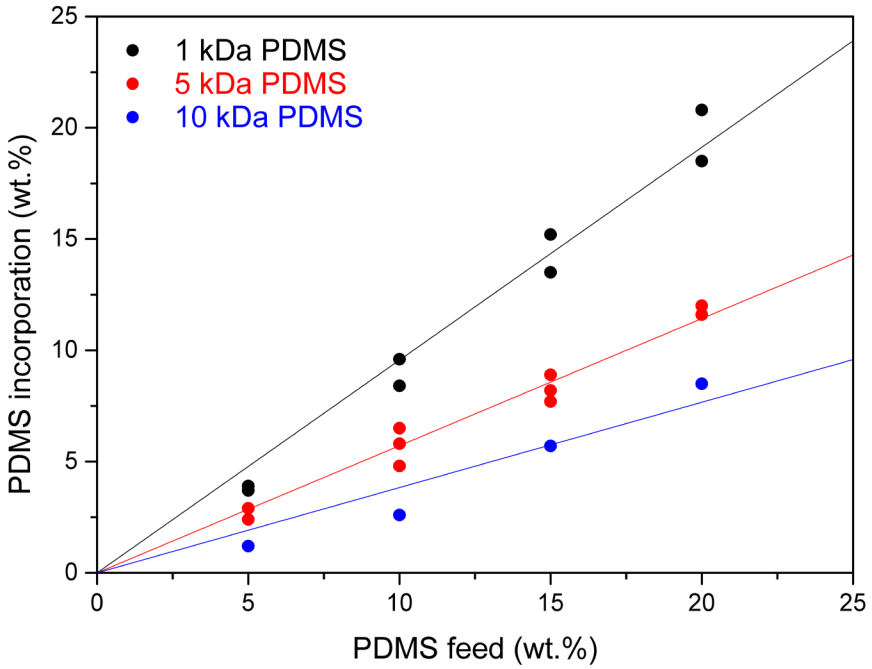

Figure 4.1: Plot of incorporation vs feed with accompanying trendlines for PAN-g-PDMS copolymerization reactions employing 1 kDa (black), 5 kDa (red) and 10 kDa (blue) PDMS macromonomers

From this plot it is clear that even though the incorporation of the PDMS macromonomers differs from the feed for all chain lengths used, a linear trend exists proving the incorporation to be directly proportional to the feed ratio. This result suggests that a macromonomer incorporation vs. feed plot

can be formulated. The intercept must be set to zero: when no PDMS macromonomer is used in the feed it cannot be incorporated and a homopolymer consisting of the monomers would be formed.

The duplicate series of copolymers synthesized using 1 kDa PDMS macromonomers were used as a single dataset for the plot. A linear fit of the data resulted in a slope of 0.956 and an R^2-value of 0.993. The high R^2-value proves that a linear fit described the data well and thus a linear trend is followed. The slope proves that only a minor discrepancy between the feed ratio and the incorporation of PDMS macromonomers can be expected.

The three series of copolymers synthesized using 5 kDa PDMS macromonomers at differeing amount of initiator were used as a single dataset. This was done because there was no clear difference in PDMS macromonomer incorporation between the three series. The PDMS macromonomer incorporation is clearly independent of the amount of initiator added to the reaction. The linear fit resulted in a slope of 0.571 and an R^2-value of 0.995. The slope suggests that the wt.% incorporation of PDMS macromonomers is expected to be close to half the wt.% in the feed, much lower than the incorporation expected when using the 1 kDa PDMS macromonomers. The high R^2-value proves that using results from the three series as a single dataset is legitimate and that PDMS macromonomer incorporation is independent of the amount of initiator used. If this premise was not valid, the three series would not lead to an acceptable R^2-value if used as a single dataset.

The linear fit of the series containing 10 kDa PDMS macromonomers resulted in a slope of 0.383 and an R^2-value of 0.968. The slope suggests that a much lower incorporation can be expected than in the case of the lower chain length PDMS macromonomers.
These results support the hypothesis that a lack of accessibility of the reactive vinyl group leads to lower incorporation of the PDMS macromonomers. When larger macromonomers are used, a larger amount is needed to achieve the desired incorporation. As a result, a larger amount of macromonomer will remain unreacted and will be removed during the hexane extraction procedure if larger macromonomers are used.

In order to achieve better incorporation of the PDMS macromonomer and minimize the loss of macromonomers, the 1 kDa PDMS macromonomer was selected for use instead of the higher molar mass macromonomers in the rest of this study.

4.2 Electrospinning of copolymer nanofiber precursors

4.2.1 Effect of PDMS graft content on precursor fiber surface morphology

Figure 4.2 shows SEM images of electrospun precursor nanofibers consisting of 1 kDa PDMS graft copolymers.

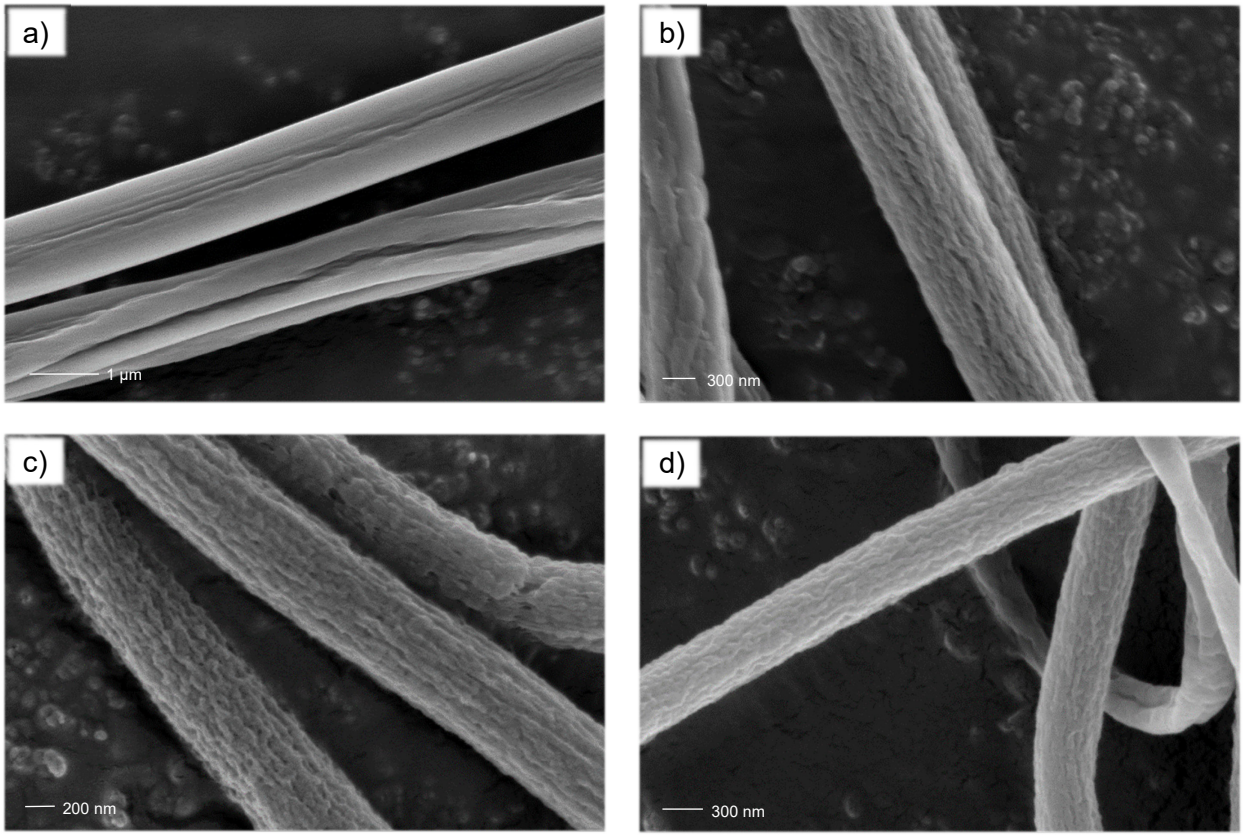

Figure 4.2: SEM images of precursor nanofibers consisting of PAN-g-PDMS copolymers containing a) 3.7 wt.%, b) 8.4 wt.%, c) 13.5 wt.% and d) 18.5 wt.% 1 kDa PDMS grafts

As discussed in *Chapter 2*, incorporation of PDMS grafts into a PAN backbone will lead to solvent-induced phase separation in a DMF solvent translating to a porous electrospun nanofiber morphology. This effect is seen in *Figure 4.2*: as the amount of PDMS incorporated increases, the porosity of the fibers increases. Since PDMS constitutes the insoluble phase, an increase in PDMS grafts incorporated into the PAN backbone is expected to cause a more porous fiber surface morphology. Whether the increase in porosity continues indefinitely with an increase in PDMS graft content is questionable.

4.2.2 Effect of molar mass, PDMS graft content and TCD

Fiber diameters results of electrospun nanofibers consisting of copolymers containing 1 kDa PDMS grafts are shown in *Figure 4.3*.

Electrospinning of the synthesized copolymers was done on the setup reported in *Chapter 3*. For electrospinning of the copolymers, the solution flow rate was 14 µl/min, the applied voltage was 15 kV in accordance with the literature method reported for electrospinning of PAN-g-PDMS copolymers

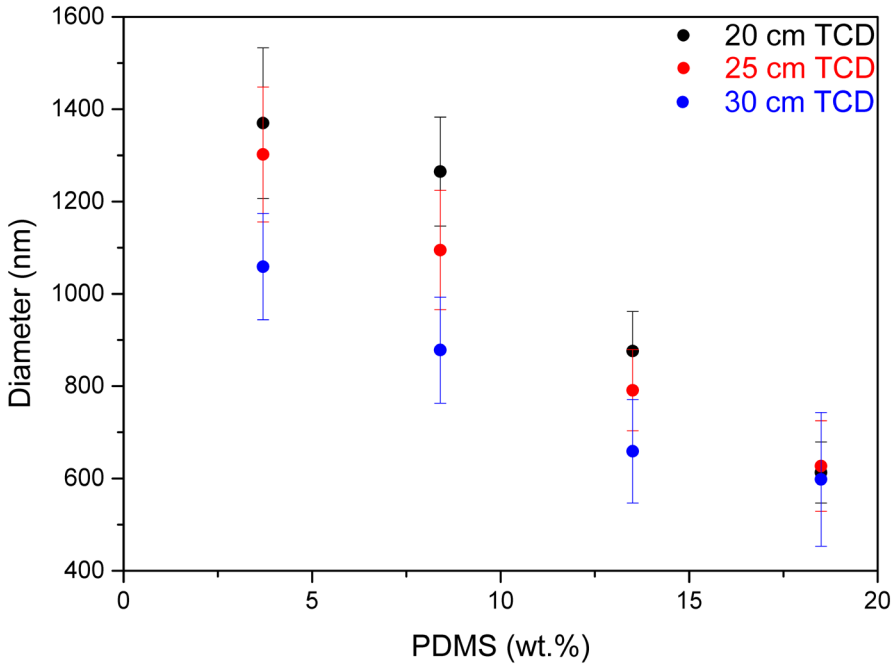

Figure 4.3: Fiber diameter w.r.t. PDMS graft content at a TCD of 20 cm (black), 25 cm (red) and 30 cm (blue) for PAN-g-PDMS copolymers containing 1 kDa PDMS grafts electrospun at a concentration of 15 wt.% (bars show intervals of one standard deviation, not errors)

from a DMF polymer solution.[1] Copolymers containing PDMS grafts of 1 kDa and 10 kDa were spun at a solution concentration of 15 wt.% of polymer in DMF while those containing grafts of 5 kDa were spun at 10.5 wt.%, 10 wt.% and 8 wt.% due to gelation occurring at higher concentrations as discussed in the previous section. The fiber diameter results were obtained by measuring at least 50 fiber diameters and calculating the number average and standard deviation of the measured fiber diameters. To investigate the effect of tip-to-collector distance (TCD), electrospinning was done at three distances namely 20 cm, 25 cm and 30 cm for all three series of PDMS grafts. A decrease in fiber diameter with an increase in TCD has been reported in the literature for electrospun PAN-g-PDMS nanofibers.[2,4]

For the series containing 1 kDa PDMS grafts, fiber diameters decrease as the PDMS graft content increases for all TCD's at which fibers were spun. This is in contrast to literature results reported on electrospinning of PAN-g-PDMS copolymers.[1,2,4] The incorporation of PDMS grafts leads to self-assembled morphologies or aggregates that increase the electrospinning solution viscosity.[2] An increase in viscosity leads to an increase in fiber diameter due to greater resistance to stretching of the fibers.[2] Therefore, an increase in fiber diameter is expected when the PDMS graft content is increased. However, the effects of molar mass must also be taken into consideration when analyzing the fiber diameter results. The observed trend can be explained by considering the molar mass results reported in *Table 4.1*. For the series containing copolymers of 1 kDa PDMS grafts, a gradual

decrease in molar mass can be seen as the PDMS macromonomer feed is increased. Previous studies do not correlate in terms of the molar masses reported of PAN-g-PDMS copolymer series synthesized by the current procedure of conventional free radical copolymerization.[1,2,4] This suggests that the molar mass trend is nothing more than mere coincidence. As Shenoy *et al*. demonstrated, the amount of chain entanglements per polymer chain, and consequently the polymer solution viscosity, increases with an increase in molar mass.[6] A decrease in molar mass is, therefore, expected to lead to a decrease in chain entanglements per polymer chain and a lower viscosity that translates to a smaller fiber diameter. However, the results of Shenoy *et al*. were reported for various homopolymers, not graft copolymers.[6] Graft copolymers, having grafts that act as chain branches, will have a higher molar mass than linear homopolymers at equal hydrodynamic volumes, i.e. at equal molar mass as determined by SEC. It is, therefore, not legitimate to make an assumption about the amount of chain entanglements and consequent solution viscosity based solely on SEC results. Nevertheless, the results prove that the fiber diameter follows the trend of molar mass and not that of PDMS incorporated. The lack of the expected effects of PDMS aggregate formation might be due to the absence thereof. Aggregation might, at least to an extent, be prevented by the method of polymer solution preparation. Human reported a procedure whereby an electrospinning solution was prepared by stirring at 40 °C until all the polymer was completely dissolved followed by sonication for 30 min. after which electrospinning of the prepared polymer solutions was carried out immediately.[1] This procedure differs from the current procedure in terms of the temperature at which dissolution was executed as well as the duration of sonication. It is possible that self-assembled aggregates consisting of PDMS grafts could have formed during dissolution at 50 °C and subsequently disintegrated during extended sonication. Alternatively, the slightly higher temperature of 50 °C might have prevented the formation of aggregates after which sonication further inhibited the formation thereof. In the latter case, a critical temperature of aggregate formation exists between 40 °C and 50 °C above which aggregate formation is inhibited. Avoiding PDMS aggregate formation will consequently prevent the associated increase in viscosity and thereby counteract the expected trend of increasing fiber diameter with increasing PDMS graft content.

The fiber diameter of electrospun PAN-g-PDMS copolymer-based nanofibers is expected to decrease as the TCD is increased.[2,4] During fiber formation the surface charge on forming fibers causes stretching of the fibers and thereby yield fibers with a very small diameter which is typical in electrospinning. An increase in TCD will lead to increased time of flight and greater fiber stretching thereby leading to thinner fibers.[2] Increasing the TCD has been shown to yield more uniform nanofibers.[2,4] A trend of decreasing fiber diameter with an increase in TCD is seen for all but the copolymer containing 18.5 wt.% PDMS grafts. Results do, however, show that the intervals within one standard deviation from the average fiber diameter overlap for the fibers spun at 25 cm and 30 cm consisting of the copolymer containing 18.5 wt.% PDMS grafts. Therefore, it cannot be concluded with certainty that the 18.5 wt.% PDMS copolymers do not follow the expected trend.

Electrospinning of the copolymers containing 5 kDa PDMS grafts proved to be more challenging than electrospinning of copolymers containing 1 kDa and 10 kDa PDMS grafts. Due to severe gelation at 15 wt.% concentration, two new series were made containing increasing amounts of initiator in the polymerization reaction in an attempt to lower the molar mass and thereby produce copolymers that can be electrospun at 15 wt.% concentration as the series of 1 kDa and 10 kDa PDMS graft copolymers. None of the three series of 5 kDa PDMS grafts could be spun at 15 wt.% concentration and consequently had to be spun at the maximum concentrations at which gelation did not take place, namely 8 wt.%, 10 wt.% and 10.5 wt.% concentration respectively.

Fiber diameter results of the first series, electrospun at a polymer solution concentration of 8 wt.%, are shown in *Figure 4.4*.

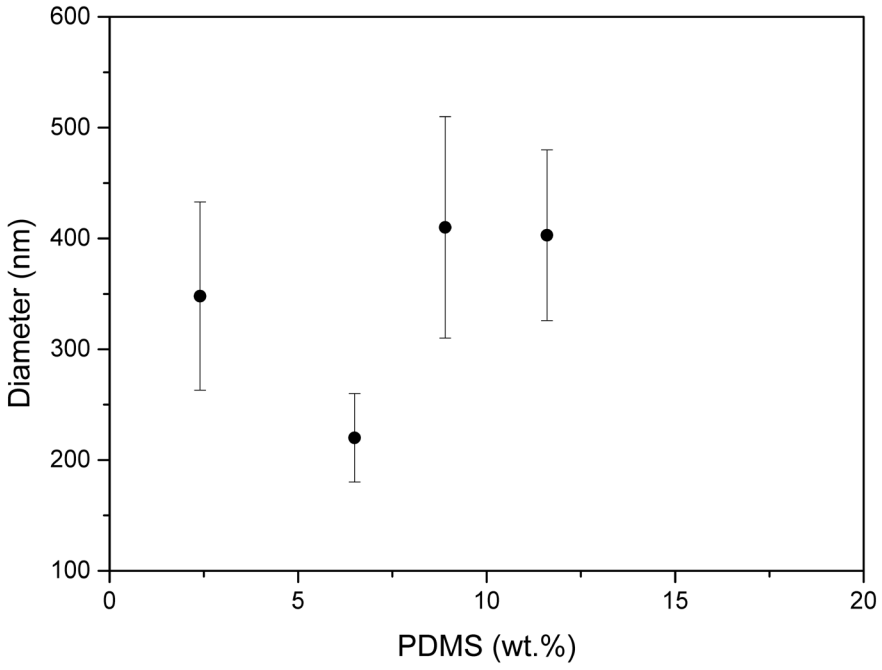

Figure 4.4: Fiber diameter w.r.t. PDMS graft content at a TCD of 20 cm for PAN-g-PDMS copolymers containing 5 kDa PDMS grafts synthesized using 0.10 wt.% AIBN and consequently electrospun at a concentration of 8 wt.%

The fiber diameters can again be explained by considering the PDMS graft content and the molar mass reported in *Table 4.2*. The copolymer containing 8.9 wt.% PDMS has a lower molar mass than that of the copolymer containing 2.4 % PDMS but due to the higher amount of PDMS incorporated it formed fibers of larger diameter than other copolymers in the series. The copolymer containing 11.6 wt.% PDMS grafts has a lower molar mass than that of both the copolymers containing 2.4 wt.% and the 8.9 wt.% PDMS grafts but has a higher amount of PDMS grafts incorporated and consequently formed fibers with an average diameter between those formed by the aforementioned

copolymers. The copolymer containing 6.5 wt.% PDMS grafts had the lowest molar mass, lower than the copolymer containing 2.4 wt.% PDMS grafts, and, therefore, formed fibers with smaller diameters than those formed by copolymers containing 2.4 wt.% PDMS grafts.

The second series, of which the results are shown in *Figure 4.5*, was spun at a polymer solution concentration of 10 wt.% and a TCD of 20 cm.

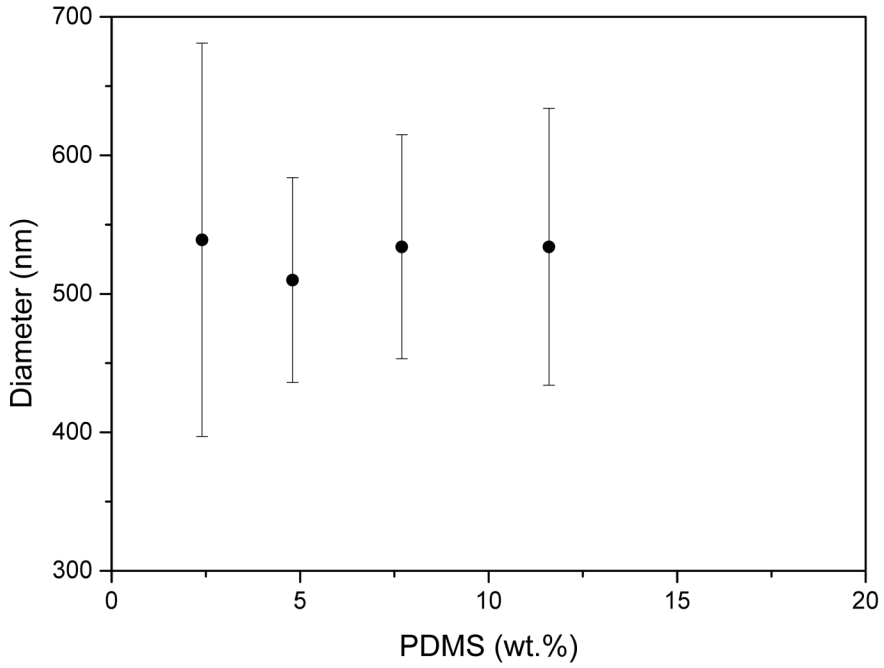

Figure 4.5: Fiber diameter w.r.t. PDMS graft content at a TCD of 20 cm for PAN-g-PDMS copolymers containing 5 kDa PDMS grafts synthesized using 0.15 wt.% AIBN and consequently electrospun at a concentration of 10 wt.%

From *Table 4.2* it can be seen that copolymers in this series have comparable molar masses with a slight initial increase in going from the 2.4 wt.% PDMS graft copolymer to the 4.8 wt.% PDMS graft copolymer and then gradually decreasing to the 11.6 wt.% PDMS graft copolymer. The fibers formed from this series have similar average fiber diameters all within one standard deviation of each other. This supports the premise that the molar mass of the copolymers in solution and the PDMS graft incorporation both affect the electrospun fiber diameter.

Results of the third series, electrospun at a polymer solution concentration of 10.5 wt.% and TCD's of 20 cm, 25 cm and 30 cm, are shown in *Figure 4.6*.

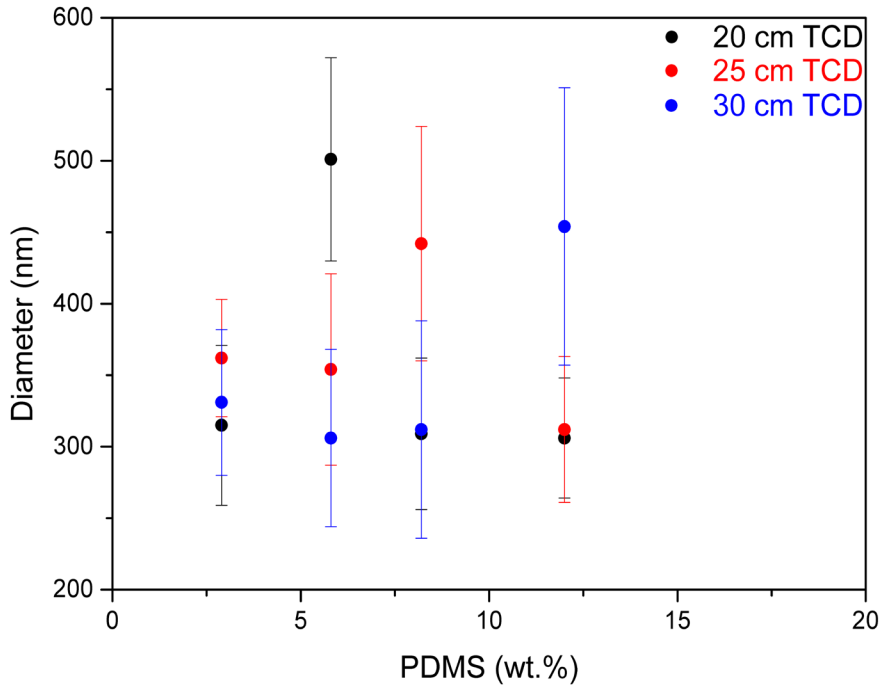

Figure 4.6: Fiber diameter w.r.t. PDMS graft content at a TCD of 20 cm (black), 25 cm (red) and 30 cm (blue) for PAN-g-PDMS copolymers containing 5 kDa PDMS grafts synthesized using 0.20 wt.% AIBN and consequently electrospun at a concentration of 10.5 wt.%

The copolymers in this series also have very similar molar masses. At each TCD it is clear that one copolymer leads to a fiber diameter much larger than that of the rest of the copolymers. The reason for this result is not clear.

Figure 4.7 shows results of the 10 kDa series electrospun at 20 cm, 25 cm and 30 cm TCD.

There is no clear trend with respect to increasing PDMS graft content for the nanofibers consisting of copolymers containing 10 kDa PDMS grafts. Considering the results reported in *Table 4.3*, no clear trend can be seen between fiber diameter and molar mass either.

For this series it is clear that, at all TCD's, the copolymers containing 1.2 wt.% PDMS grafts, having the largest molar mass of the 10 kDa PDMS graft series, form fibers that have larger diameters than those formed by the copolymers containing 2.6 wt.% PDMS grafts. This can be ascribed to the substantial decrease in molar mass when going from the copolymers containing 1.2 wt.% PDMS grafts to those containing 2.6 wt.% PDMS grafts. The copolymers containing 2.6 wt.%, 5.7 wt.% and 8.5 wt.% PDMS grafts all have similar molar masses. The increasing amount of PDMS incorporated at similar molar masses in going from the copolymer containing 2.6 wt.% PDMS grafts to those

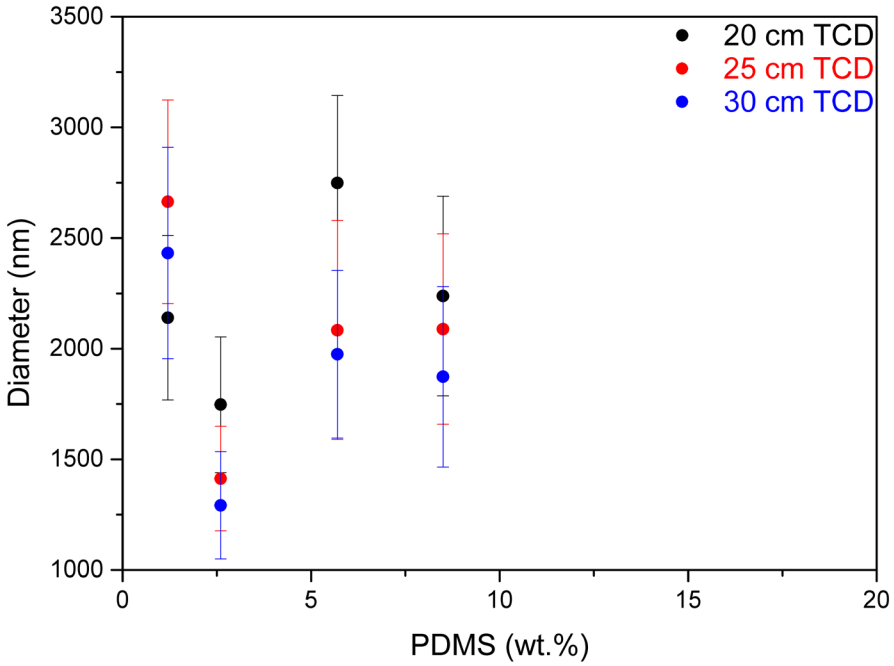

Figure 4.7: Fiber diameter w.r.t. PDMS graft content at a TCD of 20 cm (black), 25 cm (red) and 30 cm (blue) for PAN-g-PDMS copolymers containing 10 kDa PDMS grafts electrospun at a concentration of 15 wt.%

containing 5.7 wt.% and 8.5 wt.% PDMS grafts leads to the increase in fiber diameters. Fibers electrospun from copolymers containing 5.7 wt.% and 8.5 wt.% PDMS grafts have clearly overlapping intervals of standard deviation and, therefore, no definite conclusion can be drawn w.r.t. differences in fiber diameters. Even though aggregate formation might be impaired, PDMS grafts are still expected to increase viscosity due to an increased amount of chain entanglements. As mentioned earlier, copolymers of equal hydrodynamic volume can have different molar masses due to the fact that PDMS grafts act as chain branches. The copolymers containing higher amounts of PDMS grafts may have higher molar masses even though their hydrodynamic volumes may be close to those of lower molar mass copolymers having a lower amount of PDMS graft incorporation. This provides a possible explanation for the increase in fiber diameter through an increase in chain entanglements.

Alternatively, the more established explanation pertaining to the formation of aggregates could be valid. If this is true the formation of aggregates of copolymers containing 10 kDa PDMS grafts and those containing 1 kDa PDMS grafts differ in either kinetics of formation or thermodynamic stability since the method of preparation was the same.

4.2.3 Effect of polymer solution ageing on precursor fiber surface morphology

Figure 4.8 shows selected SEM images from a solution ageing study during which a polymer solution of PAN-g-PDMS copolymer containing 18.5 wt.% 1 kDa PDMS grafts was aged for a total of 168 h and spun at intervals.

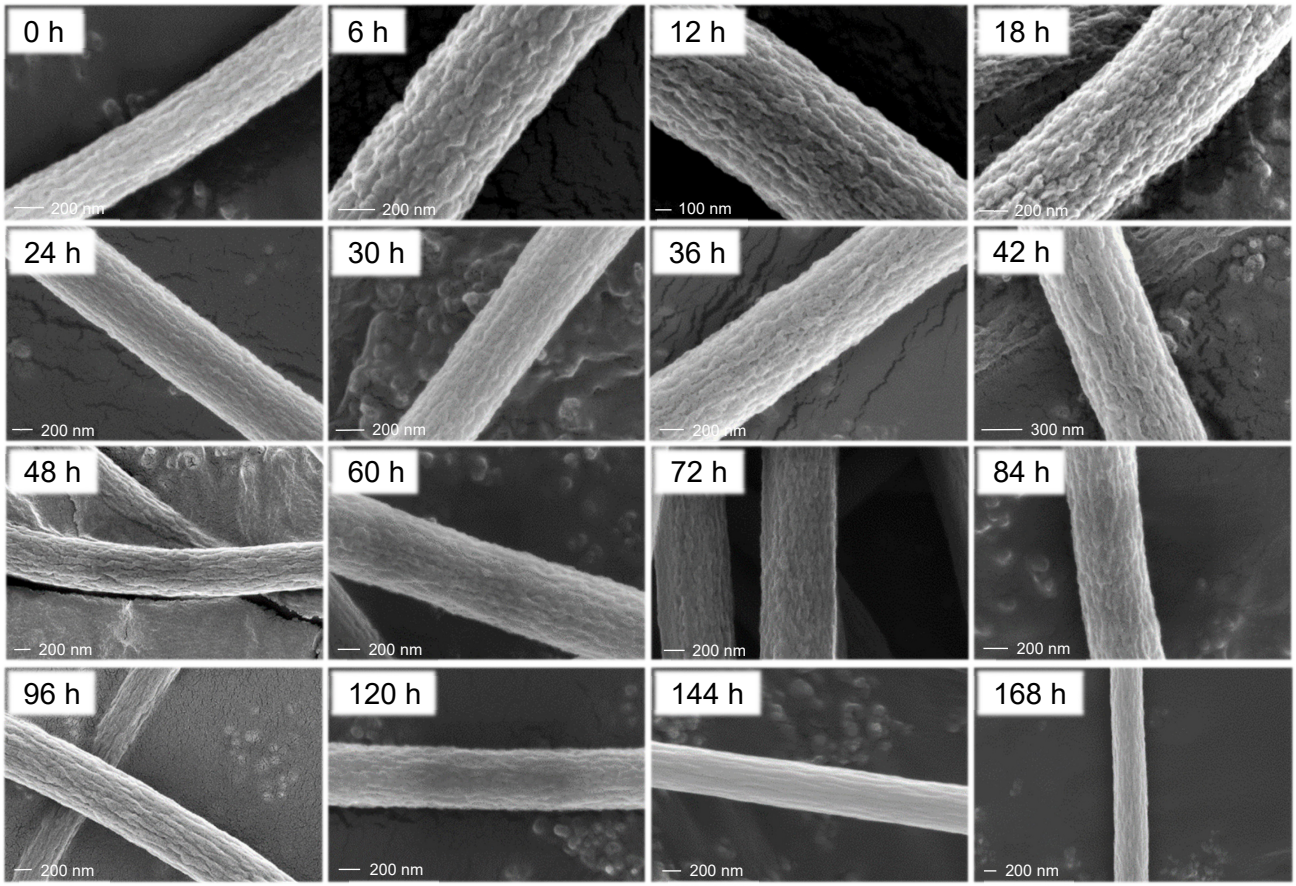

Figure 4.8: SEM images of fibers electrospun from solutions aged for various times (h)

It has been reported that solution ageing of PAN-based polymers in DMF increases solution viscosity.[1] This phenomenon is due to interactions between the polar nitrile groups and the surrounding solvent molecules that form solvent bridges between nitrile pendant groups.[7] As the solution is allowed to age, the amount of solvent molecules that constitute solvent bridges between the polar nitrile pendant groups decreases due to interdiffusion of polymers thus leading to stronger interactions between nitrile groups and a higher solution viscosity.[1]

The phase separation of PAN sections constituting the polymer backbone and the PDMS sections constituting the grafts, is also a time-dependent process. Human has demonstrated that a more roughly textured surface morphology of electrospun precursor fibers is achieved as solution ageing time is increased.[1] The amphiphilic nature of the graft copolymers is apparent in these results: phase separation of insoluble PDMS sections and soluble PAN sections is allowed to develop as the polymer solution is aged.

From the SEM images in *Figure 4.8* it appears that after 18 h of solution ageing, the fiber surface roughness is at its apex. At longer solution ageing times the surface roughness seems to decline and fibers with more smooth surfaces are formed. The reason for this decline in electrospun fiber surface roughness at longer solution ageing times is not clear.

4.2.4 Effect of polymer solution ageing on precursor fiber diameter

The results of fiber diameter measurements that were done at 24 h intervals for the first 120 h are shown in *Figure 4.9*.

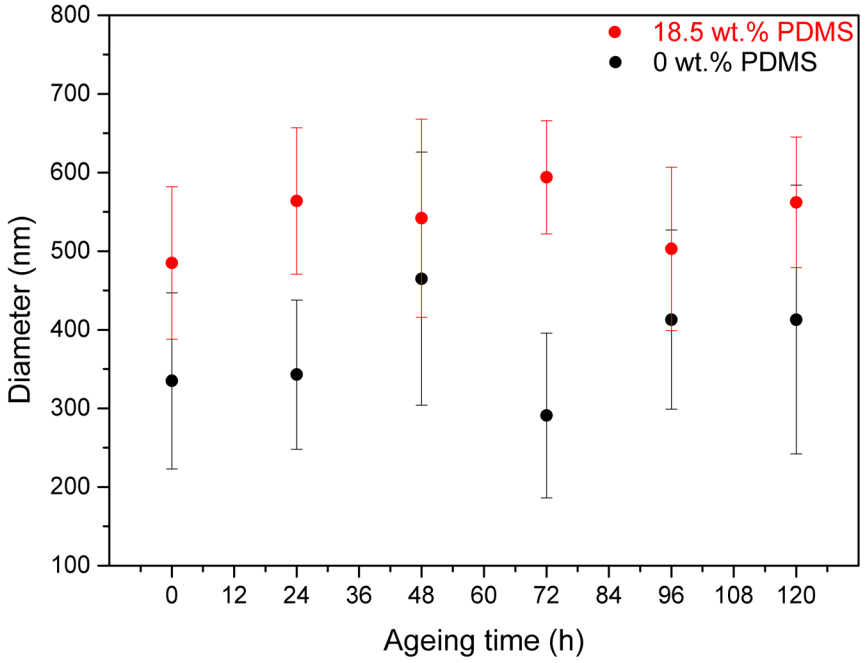

Figure 4.9: Fiber diameters of nanofibers consisting of PAN-g-PDMS copolymers containing 18.5 wt.% PDMS grafts electrospun from solutions aged at 24 hr intervals

The fiber diameters do not follow the expected trend: there is no clear increase in fiber diameter as solution ageing time continues. A possible reason for this is the variation in ambient conditions throughout the 120 h period for which fiber diameter measurements were done. Eom *et al*. have demonstrated that the intrinsic viscosity, the dynamic viscosity as well as the hydrodynamic volume, all of which are related, are dependent on the polymer solution temperature of PAN solutions in DMF.[7] They demonstrated an increase in these three solution properties as the temperature is increased due to the shortening of solvent bridges between polar nitrile groups.[7] In the current study, the incorporation of PDMS grafts might lead to different trends in solution properties w.r.t. temperature variations. It appears that variations in ambient temperature had a significant effect on the electrospun fiber diameter. The results of fiber diameter measurements w.r.t. solution ageing time are, therefore, inconclusive. This is in stark contrast to results by Human that showed a clear increase in fiber diameter with solution ageing time for both the PAN homopolymer and a PAN-g-

PDMS copolymer containing 12.1 wt.% PDMS grafts with the effect being more pronounced for the PAN homopolymer due to the fact that solvent bridges form between polar nitrile pendant groups on the PAN backbone.[1]

Comparison of the SEM images and the fiber diameter measurements w.r.t. solution ageing time reveals an interesting occurrence. It is clear that the surface roughness does increase w.r.t. solution ageing time until an apex is reached after which a gradual smoothening of the fiber surface is observed; a result clearly in agreement with what is expected from solution phase separation of the synthesised PAN-g-PDMS copolymers. The process of phase separation of the insoluble PDMS sections and soluble PAN sections of the copolymers is time-dependent.[1] Sporadic fiber diameters suggest that ambient conditions have an immediate effect on the polymer solution viscosity that can undermine effects emerging from polymer solution ageing. The effects of ambient conditions do not, however, eradicate phase separated morphologies. Polymers need to undergo conformational changes in solution in order to form phase separated morphologies that develop over time. Solvent bridges that form between adjacent polymer molecules are strongly dependent on temperature. An increase in temperature will “kick out” solvent molecules while a decrease in temperature will allow more solvent molecules to span solvent bridges.[7] Since solvent molecules are present in abundance and the process of lengthening or shortening of solvent bridges do not require any timely conformational rearrangement of the polymer molecules, a change in ambient conditions will have an immediate effect on the solution viscosity. Polymer solution conformations may also be dependent on temperature, though considering the consistent change in precursor fiber surface morphology it appears that a thermodynamically stable solution morphology is not reached within at least the first 24 h of solution ageing after which a gradual decline in roughness of the precursor fiber surface morphology is seen. Evidently, the effect of temperature on the surface morphology of electrospun precursor fibers is negligible. The contrast between the strong temperature dependence of the precursor fiber diameters and the weak temperature dependence of the precursor fiber surface morphologies produced by electrospinning of aged solutions of PAN-g-PDMS copolymers in DMF shows the complex interplay between different solution processes and conditions under which the solutions were prepared and electrospun as well as differences in kinetics and thermodynamic stability of the underlying processes.

4.3 Thermal behavior of copolymer powders and nanofibers

Figure 4.10 shows the DSC thermograms of the powders and electrospun fibers for copolymers containing 1 kDa PDMS grafts.

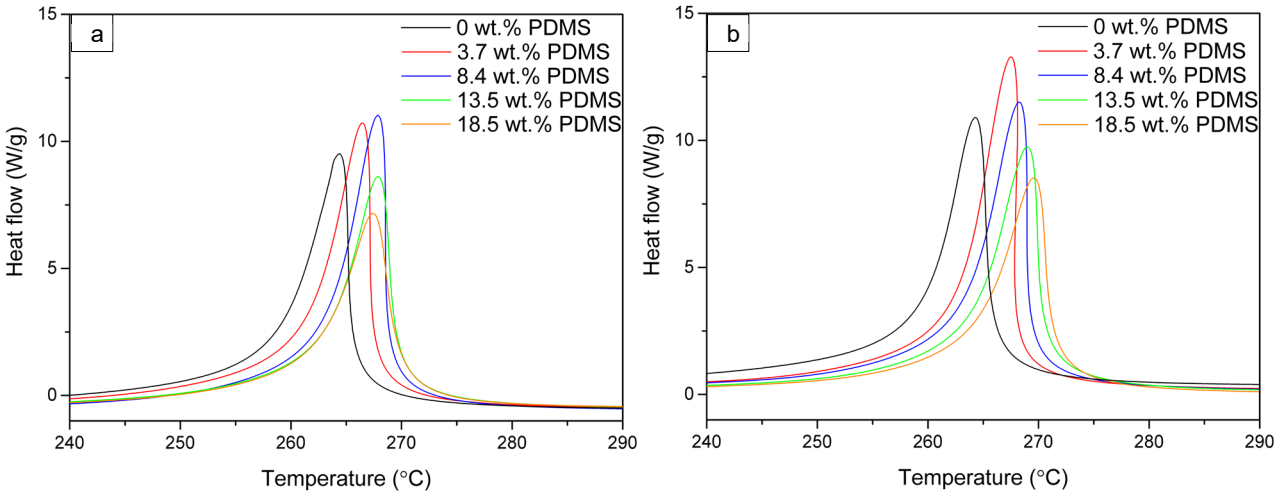

Figure 4.10: DSC thermograms of a) powders and b) electrospun nanofibers consisting of PAN homopolymer (black) and PAN-g-PDMS copolymers containing 3.7 wt.% (red), 8.4 wt.% (blue), 13.5 wt.% (green) and 18.5 wt.% (orange) 1 kDa PDMS grafts

Cyclization of pendant nitrile groups is the first step in the process of carbonization. It is a crucial step since the ladder-type polymers that are formed as products are needed for subsequent carbonization steps. A sharp exotherm exists in the DSC thermogram seen in *Figure 4.10* which originates from the cyclization process in question. It has been shown that the incorporation of PDMS grafts into a PAN backbone shifts the peak associated with the cyclization exotherm enthalpy to a higher temperature.[1] In addition, it was found that the cyclization reaction occurred to a lesser extent as the PDMS graft incorporation was increased.[1] The incorporation of PDMS grafts into the backbone clearly affects the process of cyclization. The reported peak maxima were shifted to a higher temperature according to the PDMS graft content which indicates retardation of the cyclization process.[1] The thermal procedure followed in the DSC analyses does, however, not represent the actual thermal procedure employed during carbonization since the DSC analyses were done in nitrogen. Therefore, oxidation reactions inherent in the carbonization procedure can be neglected when considering the results. The exotherm enthalpy can be considered to be originating only from the cyclization of PAN sections. Since the cyclization reaction occurs in PAN sections of the copolymer and not in PDMS sections, it would be useful to have a value for the enthalpy corrected for amount of PAN in the sample. Results from ^{1}H NMR, reported in *Table 4.1*, *Table 4.2* and *Table 4.3*, show the wt.% PDMS grafts for the synthesised PAN-g-PDMS copolymers. Using this value and the enthalpy of cyclization, i.e. integrated area under the cyclization exotherm, the corrected cyclization enthalpy can be calculated as follows:

$$Corrected\ enthalpy = \left(\frac{Enthalpy}{Mass\ fraction\ of\ PAN}\right)$$

This value is significant due to the fact that the exothermic cyclization reaction takes place between adjacent nitrile groups in the PAN sections and not in the PDMS sections. Comparison of these values from different samples shows the relative amount of PAN sections that took part in the cyclization process.

The peak maxima and corrected exotherm enthalpy w.r.t. 1 kDa PDMS graft content for the powders and electrospun fibers are shown in *Figure 4.11*.

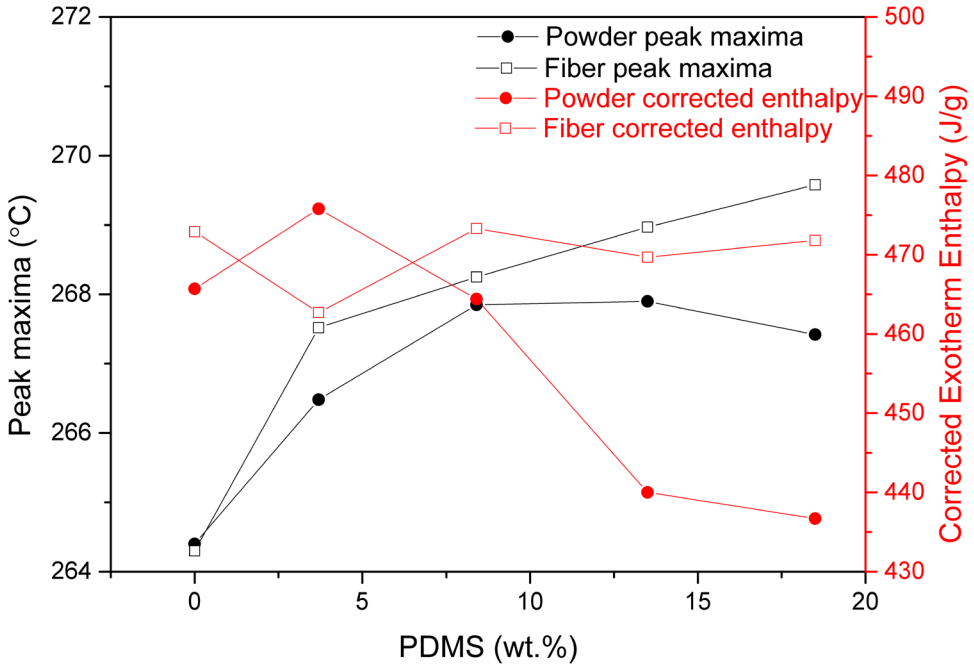

Figure 4.11: Peak maxima (black) and corrected exothermic enthalpy (red) w.r.t. PDMS graft content of powders (solid dots) and electrospun nanofibers (open squares) consisting of copolymers containing 1 kDa PDMS grafts

Table 4.4 summarizes the peak maxima, the exotherm enthalpy and the corrected exotherm enthalpy for powders and electrospun fibers containing 1 kDa PDMS grafts.

Table 4.4:

DSC peak maximum, exotherm enthalpy and corrected exotherm enthalpy for thermograms of 1 kDa PDMS graft copolymers

	PDMS (wt.%)	Peak maxima (°C)	Exotherm enthalpy (J.g)	Corrected exotherm enthalpy (J/g)
Powders	0	264.4	465.7	465.7
	3.7	266.5	458.2	475.8
	8.4	267.9	425.4	464.4
	13.5	267.9	380.6	440.0
	18.5	267.4	355.9	436.7
Fibers	0	264.3	472.9	472.9
	3.7	267.5	445.6	462.7
	8.4	268.3	433.5	473.3
	13.5	269.0	406.3	469.7
	18.5	269.6	384.5	471.8

As seen in *Figure 4.11* and *Table 4.4*, peak maxima increase continuously with PDMS graft content for the electrospun nanofibers but not for the powders. It is to be expected, considering phase separated regions in electrospun fibers that are known to retard the cyclization reaction.

Table 4.4 shows a decrease in the cyclization exotherm enthalpy with increasing PDMS graft content. This decrease is to be expected since the PAN sections decrease in mass content as the PDMS grafts increase in mass content. It is expected that the phase separation would impair the cyclization reaction between adjacent nitrile groups, yet this is not seen in the results. Human reported results of DSC experiments on fibers and films of PAN-g-PDMS copolymers and observed that films showed a lower cyclization exotherm enthalpy compared to fibers.[1] It must be noted that more severe phase separation is to be expected in the case of the films than in the case of the fibers due to the respective methods of preparation. The extent of phase separation directly affects the cyclization exotherm of PAN sections in the copolymers. Therefore, the current result, showing rather consistent values for the corrected exotherm enthalpy, is puzzling. As was discussed in *Section 4.2.2*, the phase separation of copolymers in the electrospinning solution may have been impaired due to the method of polymer solution preparation. This will explain the lack of a clear decrease in the corrected exotherm enthalpy of the electrospun fibers. The decrease in the corrected exotherm enthalpy of the powder samples might be due to minor phase separated morphologies that were transferred from the reaction mixture and subsequent precipitation procedure.

DSC thermograms of both the powders and the electrospun fibers consisting of the of 5 kDa PDMS grafts synthesized with 0.10 wt.% AIBN content are shown in *Figure 4.12*.

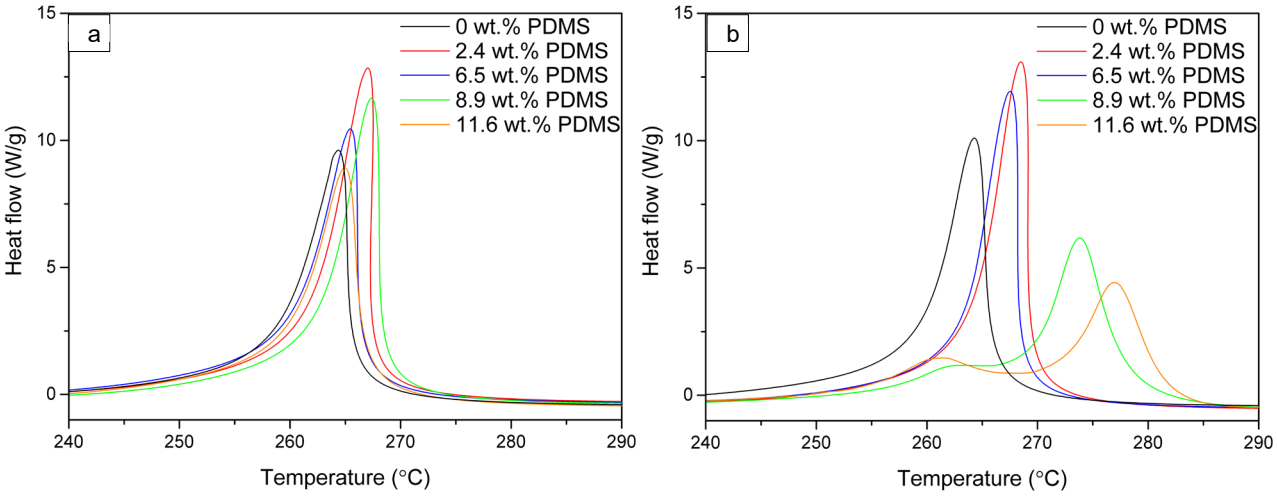

Figure 4.12: DSC thermograms of a) powders and b) electrospun nanofibers consisting of PAN homopolymer (black) and PAN-g-PDMS copolymers containing 2.4 wt.% (red) 6.5 wt.% (blue) 8.9 wt.% (green) and 11.6 wt.% (orange) 5 kDa PDMS grafts synthesized by copolymerization reactions utilizing 0.10 wt.% AIBN

The peak maxima and corrected exotherm enthalpy w.r.t. 5 kDa PDMS graft content for the powders and electrospun fibers of copolymers synthesized using 0.10 wt.% AIBN is shown in *Figure 4.13*.

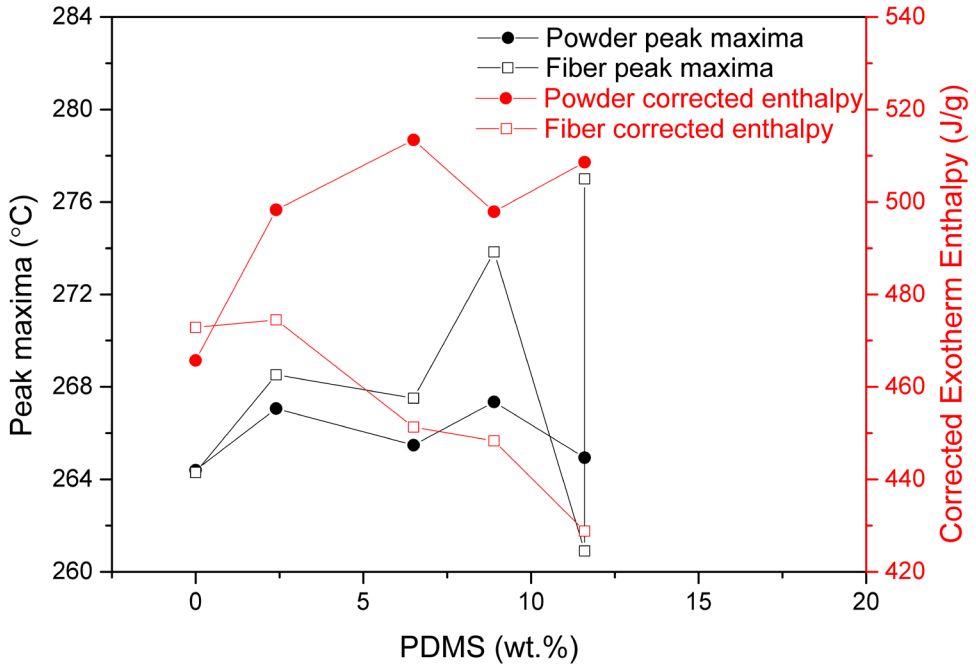

Figure 4.13: Peak maxima (black) and corrected exothermic enthalpy (red) w.r.t. PDMS graft content of powders (solid dots) and electrospun nanofibers (open squares) consisting of copolymers containing 5 kDa PDMS grafts synthesized using 0.10 wt.% AIBN

DSC thermograms of both the powders and the fibers consisting of the of 5 kDa PDMS grafts synthesized with 0.15 wt.% AIBN contents are shown in *Figure 4.14*.

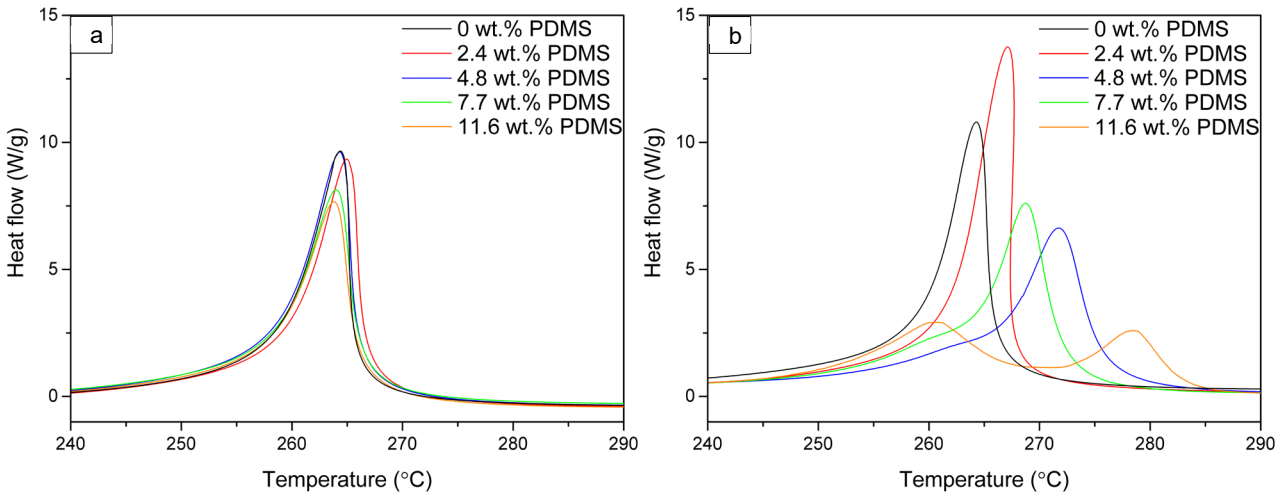

Figure 4.14: DSC thermograms of a) powders and b) electrospun nanofibers consisting of PAN homopolymer (black) and PAN-g-PDMS copolymers containing 2.4 wt.% (red), 4.8 wt.% (blue), 7.7 wt.% (green) and 11.6 wt.% (orange) 5 kDa PDMS grafts synthesized by copolymerization reactions utilizing 0.15 wt.% AIBN

DSC thermograms of both the powders and the fibers consisting of the 5 kDa PDMS grafts synthesized with 0.20 wt.% AIBN contents are shown in *Figure 4.15*.

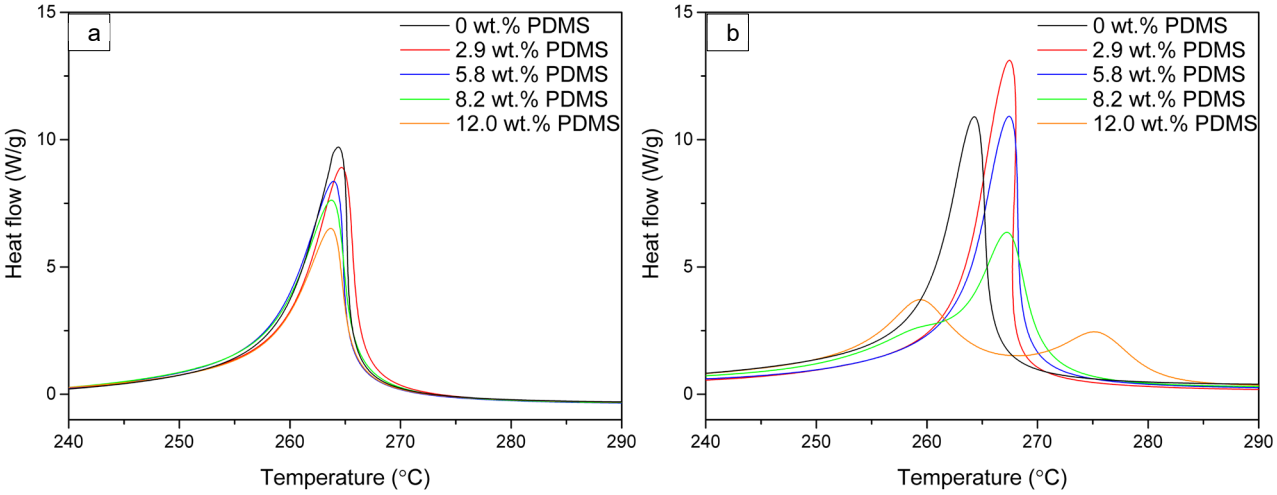

Figure 4.15: DSC thermograms of a) powders and b) electrospun nanofibers consisting of PAN homopolymer (black) and PAN-g-PDMS copolymers containing 2.9 wt.% (red), 5.8 wt.% (blue), 8.2 wt.% (green) and 12.0 wt.% (orange) 5 kDa PDMS grafts synthesized by copolymerization reactions utilizing 0.20 wt.% AIBN

Table 4.5 shows the peak maxima, exotherm enthalpy and corrected exotherm enthalpy for all the copolymer powders and electrospun nanofibers containing 5 kDa PDMS grafts.

Table 4.5:

DSC peak maximum, exotherm enthalpy and corrected exotherm enthalpy for thermograms of 5 kDa PDMS graft copolymers

	PDMS (wt.%)	Peak maximum (°C)		Exotherm enthalpy ($J.g^{-1}$)	Corrected exotherm enthalpy (J/g^{-1})
		T_{m1}	T_{m2}		
Powders	0	264.4		465.7	465.7
	2.4	267.0		486.3	498.3
	6.5	265.5		480.0	513.4
	8.9	267.4		453.6	497.9
	11.6	265.0		449.6	508.6
Fibers	0	268.5		463.1	474.5
	2.4	268.5		463.1	474.5
	6.5	267.5		422.0	451.3
	8.9	262.3	273.8	408.4	448.3
	11.6	260.9	277.0	379.1	428.8

For all the series of 5 kDa PDMS grafts, the only observed trends are those of the decreasing corrected exotherm enthalpy for the electrospun fibers of the copolymers synthesized using 0.10 wt.% AIBN (*Figure 4.12* and *Figure 4.13*) and of decreasing peak maxima for the powder samples

synthesized using 0.15 wt.% and 0.20 wt.% AIBN (*Figure 4.14* and *Figure 4.15*). The decrease in peak maxima is not expected considering trends mentioned in the literature.[1] The lack of any trends expected of solution phase separated PAN-g-PDMS copolymers supports the hypothesis that solution phase separation was inhibited during sample preparation in the case of the fibers and was never allowed time to develop in the case of the powders.

Thermograms of the copolymers containing 5 kDa PDMS grafts show interesting behaviour. A single exothermic peak is seen for all the powder samples while the fiber samples clearly show the formation of a shoulder and ultimately the formation of a doublet peak as the PDMS graft content is increased. This is observed for all of the electrospun nanofibers consisting of high PDMS graft content as can be seen in *Figure 4.12*, *Figure 4.14* and *Figure 4.15* for the copolymers containing 5 kDa grafts synthesized with different AIBN contents in the reaction. The reason for these double cyclization exotherm peaks in the high PDMS graft content samples of the 5 kDa PDMS graft series is not clear. Thermograms of the copolymers containing 1 kDa PDMS grafts (*Figure 4.10*) and those containing 10 kDa PDMS grafts (reported hereafter) all show single cyclization exotherm peaks for both the powder and the fiber samples. The fact that different samples in the 5 kDa PDMS graft series show these double cyclization peaks in the electrospun fibers suggest that there is a unique phenomenon for the 5 kDa PDMS series. Interestingly, the second cyclization peak shows a very clear shift to higher temperatures in all cases, whereas the first peak remains more or less at the PAN cyclization peak temperature with increasing PDMS content. As mentioned before, all three series containing 5 kDa PDMS grafts showed gelation at the concentrations at which the 1 kDa and 10 kDa PDMS graft copolymer series were electrospun. A possible explanation for the double peak could be that more severe phase separation of the electrospun 5 kDa PDMS graft series occurred. If this hypothesis is correct, PDMS-rich phase domains are expected to undergo the cyclization reaction at higher temperatures than the PAN-rich phase domains if heat transfer from PAN-rich domains undergoing cyclization at a lower temperature is slow compared to the heating rate of 10 °C/min followed by the thermal program. In such an event, large temperature gradients exist between phase domains in the same fiber. The same reaction, cyclization of PAN-based nitrile groups, will occur in different sections of the same fiber but at a different time and temperature during the experiment. The first peak is associated with the cyclization exotherm of PAN-rich domains consisting mainly of PAN homopolymers while the second peak is associated with the cyclization exotherm of PDMS-rich domains consisting mainly of PAN-g-PDMS copolymers. The shift in the second peak to higher temperatures with increasing PDMS grafts supports this hypothesis. The hypothesis that stated that a lack of solution phase separation is the cause of the lack of expected results seems to be in contrast to the currently stated hypothesis. However, the domain sizes may differ greatly and therefore these two processes cannot be equated.

DSC thermograms of both the powders and the fibers consisting of the of 10 kDa PDMS grafts are shown in *Figure 4.16*.

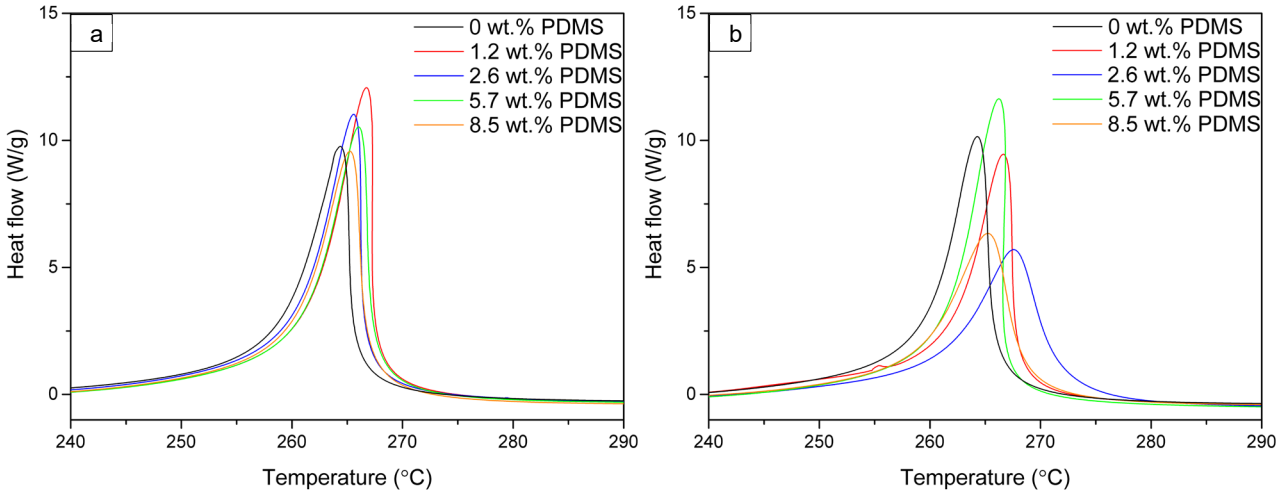

Figure 4.16: DSC thermograms of a) powders and b) electrospun nanofibers consisting of PAN homopolymer (black) and PAN-g-PDMS copolymers containing 1.2 wt.% (red), 2.6 wt.% (blue), 5.7 wt.% (green) and 8.5 wt.% (orange) 10 kDa PDMS grafts

The peak maxima and corrected exotherm enthalpy w.r.t. 10 kDa PDMS graft content for the powders and electrospun fibers of copolymers is shown in *Figure 4.17*.

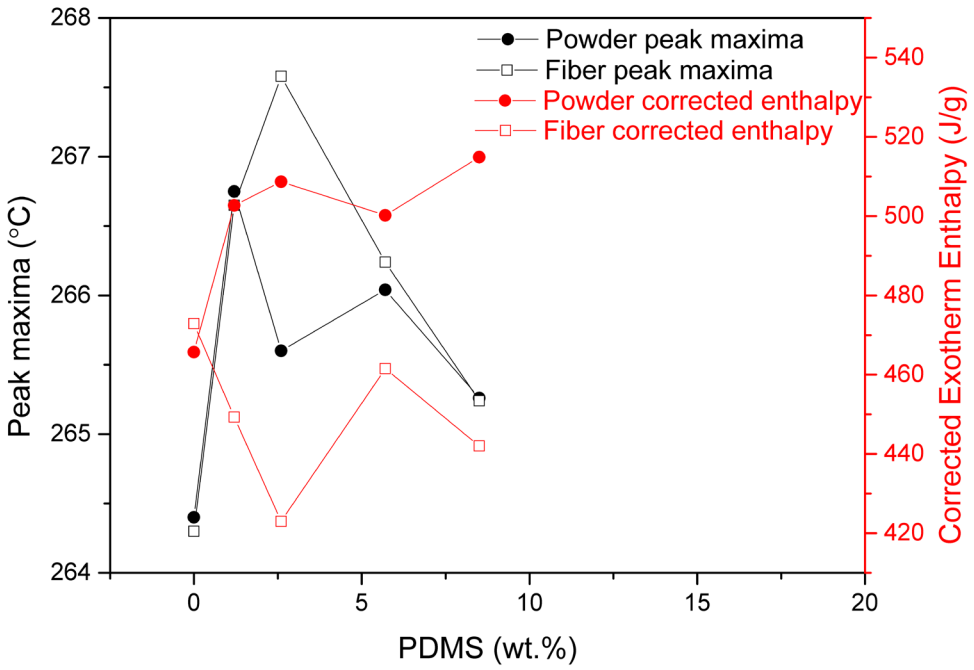

Figure 4.17: Peak maxima (black) and corrected exothermic enthalpy (red) w.r.t. PDMS graft content of powders (solid dots) and electrospun nanofibers (open squares) consisting of copolymers containing 10 kDa PDMS grafts

Table 4.6 shows the peak maxima, exotherm enthalpy and corrected exotherm enthalpy for all the copolymer powders and electrospun nanofibers containing 10 kDa PDMS grafts.

Table 4.6:

DSC peak maximum, exotherm enthalpy and corrected exotherm enthalpy for thermograms of 10 kDa PDMS graft copolymers

	PDMS (wt.%)	Peak maximum (°C)	Exotherm enthalpy (J.g)	Corrected exotherm enthalpy (J/g)
Powders	0	264.4	465.7	465.7
	1.2	266.8	496.7	502.7
	2.6	265.6	495.5	508.7
	5.7	266.0	471.7	500.2
	8.5	265.3	471.1	514.9
Fibers	0	264.4	465.7	465.7
	1.2	266.7	443.9	449.3
	2.6	267.6	412.0	423.0
	5.7	266.2	435.2	461.5
	8.5	265.2	404.4	442.0

No clear trend is seen for the peak maxima and corrected exotherm enthalpy of either the powders or the fibers. The possibility of a lack of solution phase separation exists for the 10 kDa PDMS graft copolymers as well.

4.4 Carbonisation of polymer nanofibers

The carbonized products of PAN-g-PDMS copolymers containing 1 kDa PDMS grafts are shown in *Figure 4.18*.

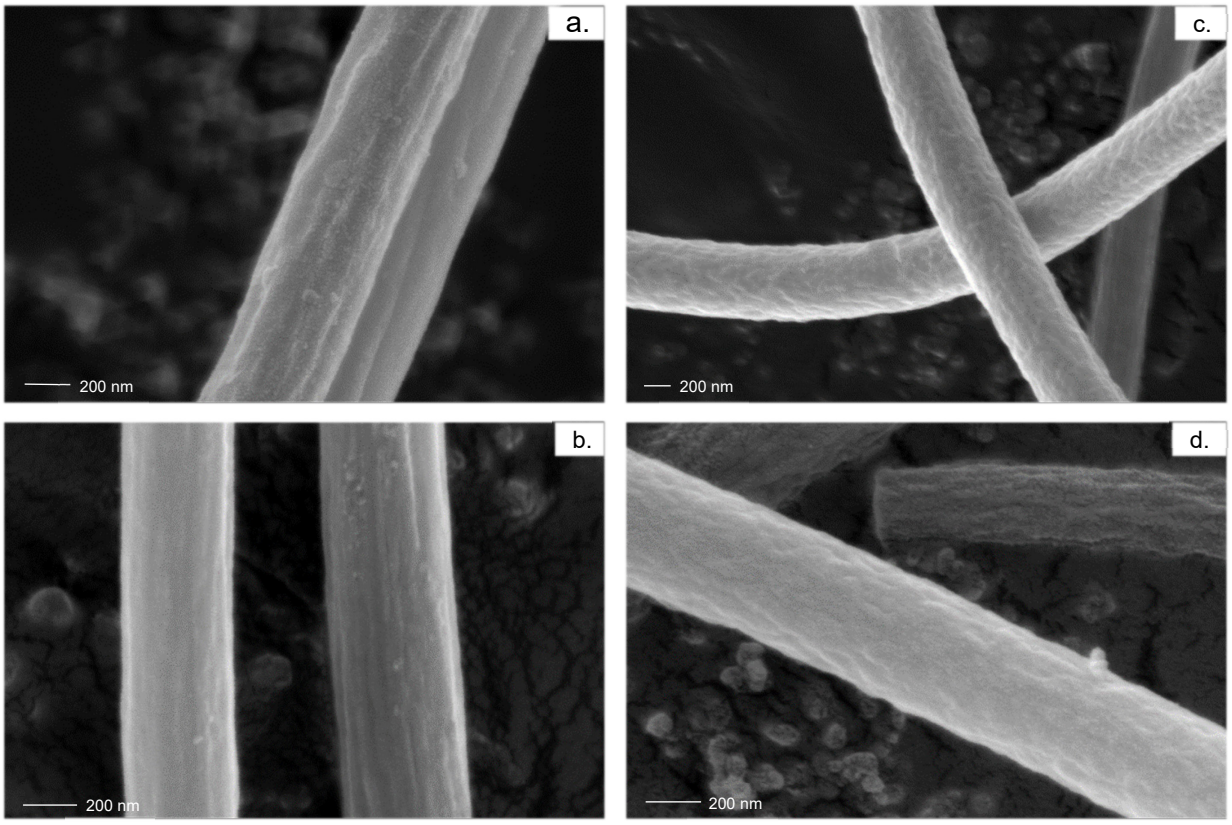

Figure 4.18: SEM images of carbon nanofibers produced by carbonization of precursor polymer nanofibers consisting of PAN-g-PDMS copolymer containing a) 3.7 wt.%, b) 8.4 wt.%, c) 13.5 wt.% and d) 18.5 wt.% 1 kDa PDMS grafts

The product is in the form of nanofibers with rough, although more smoothened than in the case of the precursor copolymer nanofibers, textured surfaces. Very little fiber breakage was noticed during imaging. This proves that the fiber morphology is retained to an extent during the carbonisation procedure. Previous results on carbonization of PAN-g-PDMS copolymer fibers also found that the surface morphology is preserved during carbonization.[1] The high thermal stability of PAN capacitates the preservation of the fiber surface morphology. This unique property is what makes PAN-based fibers suitable for carbonization.

Figure 4.19 shows digital photographs of the electrospun precursor nanofibers consisting of PAN-g-PDMS copolymers and the carbonized nanofibers thereof.

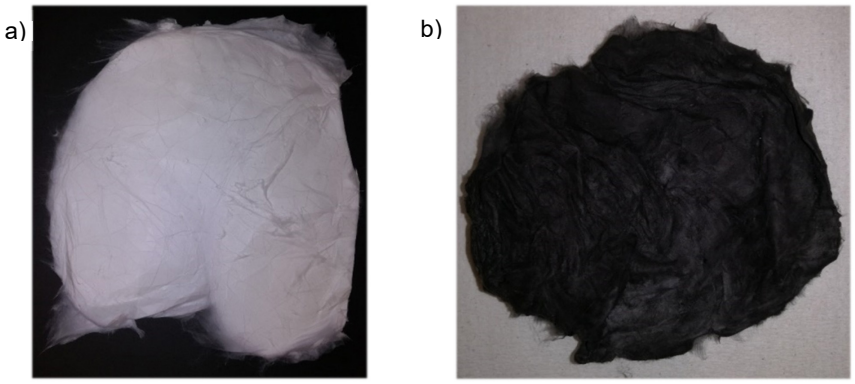

Figure 4.19: Digital photographs of a) electrospun precursor nanofibers consisting of PAN-g-PDMS copolymers as well as the b) carbonized product

Fiber diameters of the precursor nanofibers and the carbon nanofibers as well as the percentage fiber shrinkage is shown in *Figure 4.20*.

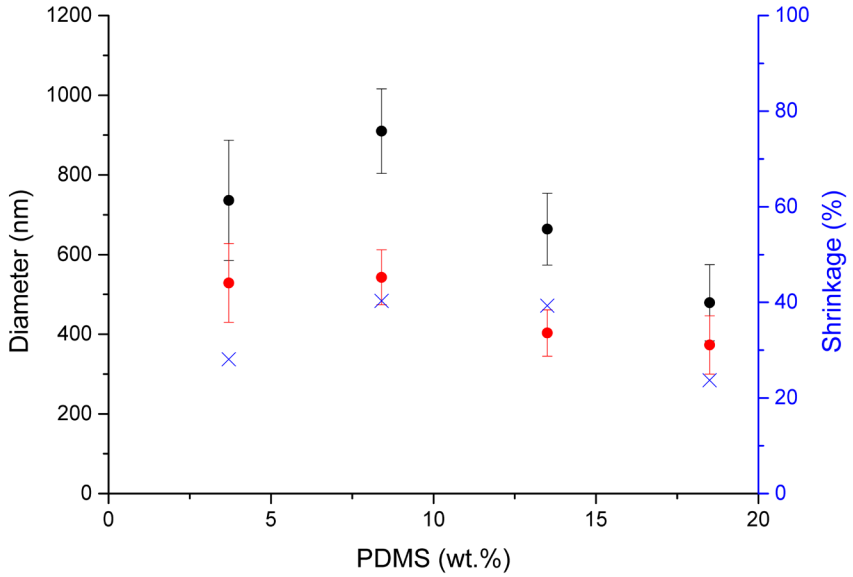

Figure 4.20: Precursor fiber diameter of nanofibers consisting of 1 kDa PDMS graft copolymers (black) and carbon fiber diameter (red) produced by carbonization of precursor nanofibers as well as fiber shrinkage (blue crosses) w.r.t. PDMS graft content

Fiber shrinkage is to be expected since a large amount of mass is lost due to the release of gases inherent in the carbonization process.[8] The pattern of fiber diameter w.r.t. PDMS graft content is retained after carbonization; a result that has previously been reported for fibers electrospun from PAN-g-PDMS copolymers.[1] Fiber shrinkage ranges from 23 % to 41 % and, considering the pattern of precursor fiber diameters, seem to be dependent on both the precursor fiber diameter as well as on the PDMS graft content. While the mass loss of PAN is well-documented and contributes greatly to the total mass loss of the PAN-g-PDMS copolymer nanofibers, the mass loss of the PDMS grafts might still contribute significantly to the overall mass loss. Considering the results of Camino *et al.*, the thermal procedure currently followed, having a slow temperature ramp to 300 °C followed by a 2

h interval in air and a 20 min interval during argon flush at 300 °C, should cause significant mass loss of PDMS starting at 290 °C.[9] Analysis of the mass loss of PAN sections and that of PDMS grafts as well as the effect of the incorporation of PDMS grafts on the mass loss of PAN sections remains an endeavor for future work.

4.5 Co-precipitation of iron oxide nanoparticles

IONPs were synthesized by co-precipitation of iron precursors as described in *Chapter 3*. TEM images are shown in *Figure 4.21*.

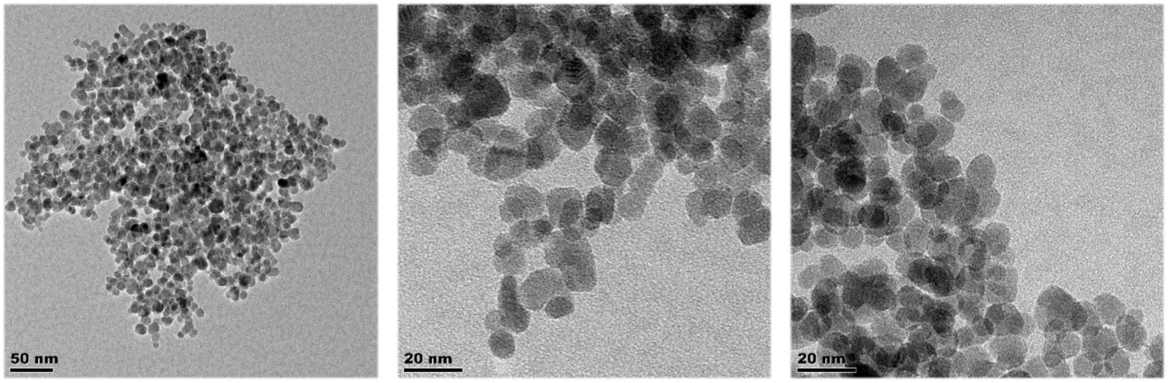

Figure 4.21: TEM images of IONPs synthesized by co-precipitation

TEM images revealed that the nanoparticles have irregular shapes while diameter measurements showed a number average particle diameter of 10.2 nm with a standard deviation of 2.4 nm. The shapes, mostly spherical or ellipsoid, and wide size distribution of the nanoparticles are to be expected considering results reported in the literature.[10,11,12,13,14]

4.6 Silica coating of iron oxide nanoparticles

4.6.1 Multi-core nanoparticles

TEM images of silica-coated IONPs are shown in *Figure 4.22*.

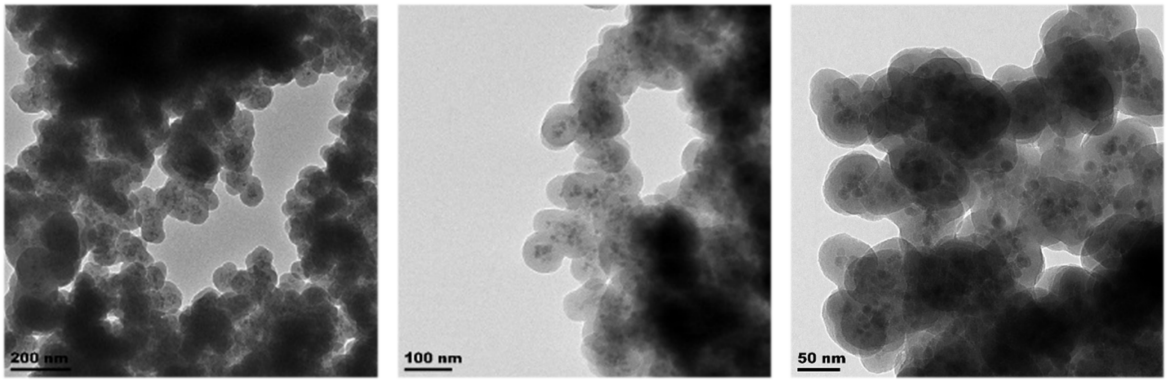

Figure 4.22: TEM images of multi-core silica-coated IONPs synthesized using 0.18 wt.% IONPs and 7.2 × 10^{-2} M TEOS

TEM imaging of the silica-coated nanoparticles, produced following the method laid out in *Chapter 3*, has shown that multi-core silica-coated nanoparticles were synthesized. Using the same general

procedure, some authors have also found multi-core nanoparticles to be formed while others have reported the formation of single-core silica-coated iron oxide nanoparticles.[14,15,16,17] The difference in the product can be attributed to differing concentrations of reagents in the reaction mixture. Among the many parameters associated with the process of silica coating are the amount of TEOS and the concentration of IONPs in the reaction mixture. Either of these two parameters could be the reason for the formation of multi-core nanoparticles. The silica layer is intended to provide a barrier between the IONPs and the surrounding carbon material during carbonization. It only needs to cover the entire surface of the IONPs; there is no minimum shell thickness required. It is important, however, that a low mass of nanoparticles will be produced if a low concentration of IONPs is to be coated with a thin silica shell. This will produce nanoparticles having a high mass percentage of magnetic iron oxide which will maximize magnetization originating from the nanoparticle core. Contrary to a thin silica shell, a thick silica shell around the magnetic nanoparticles will lead to a lower magnetization per mass of nanoparticles since the fraction of silica in the total mass of each particle will be higher. It has been demonstrated that the thickness of the silica shell can be varied by simply changing the amount of TEOS silicating agent used.[16,18]

In order to produce IONPs with a thinner silica shell, various silica coating reactions were carried out in order to find a set of reaction parameters that would lead to single-core nanoparticles with a thin silica shell. Henceforth, “multi-core nanoparticles” will refer to the nanoparticles presently discussed that contain a lower amount of IONPs in the product than those discussed in the next section.

4.6.2 Single-core nanoparticles

Figure 4.23 shows TEM images of a silica coating reaction where silica-coated IONPs were prepared using a reaction mixture containing IONPs at a concentration of 0.02 wt.% (g/mL) and TEOS at a concentration of 9.0×10^{-3} M.

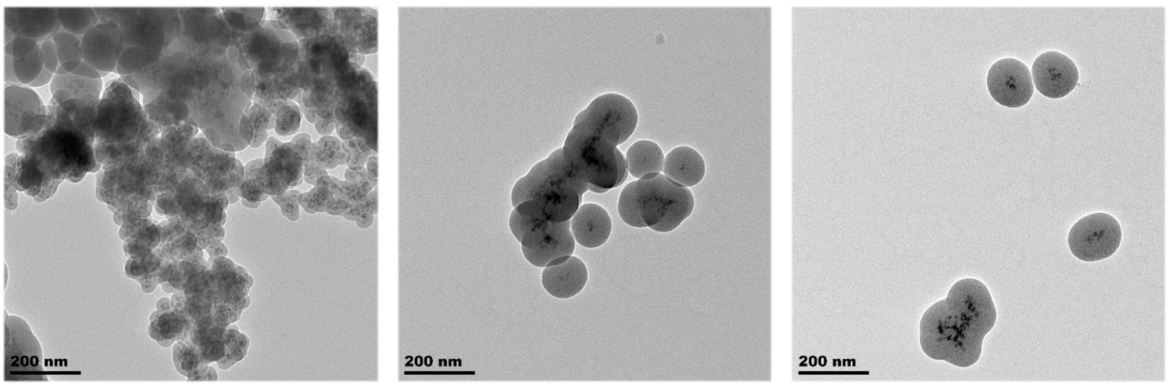

Figure 4.23: TEM images of multi-core silica-coated IONPs synthesized using 0.02 wt.% IONPs and 9.0×10^{-3} M TEOS

The concentration of IONPs added was according to the method reported by Deng *et al*.[16] The nanoparticles do not have a single-core structure and have thick silica shells.

Figure 4.24 shows TEM images of nanoparticles formed at a concentration of 0.02 wt.% IONPs (g/mL) and TEOS at a concentration of 2.3 × 10^{-3} M.

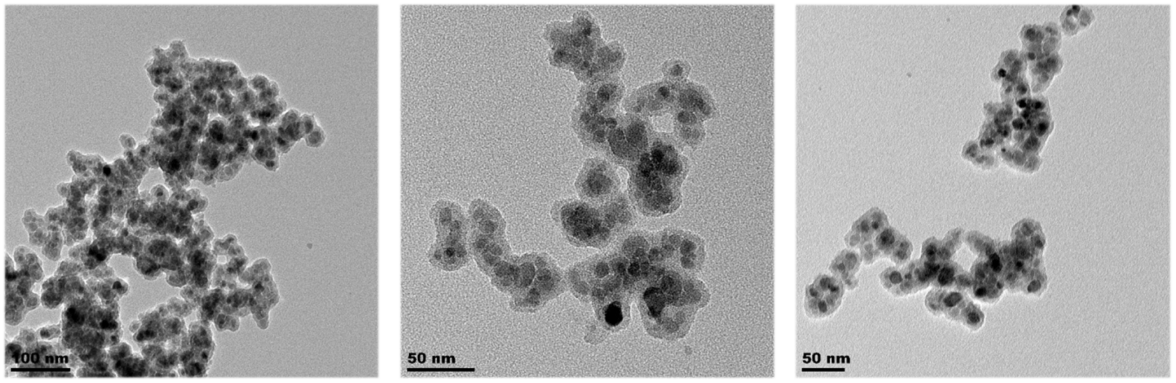

Figure 4.24: TEM images of single-core silica-coated IONPs synthesized using 0.02 wt.% IONPs and 2.3 ×10^{-3} M TEOS

From these results it is clear that the concentration of TEOS added determines the core-shell structure of the nanoparticles, however, the effects of the concentration of IONPs is still unclear since multi- and single-core nanoparticles were synthesized at the same concentration of IONPs by varying the amount of TEOS added. It is possible that, at 2.3 × 10^{-3} M TEOS, an increase in IONP concentration would lead to multi-core nanoparticles. It might be that the TEOS:IONPs ratio, not the absolute concentration of TEOS or IONPs, determines the core-shell structure of the nanoparticles.

4.6.3 Thermally treated single-core nanoparticles

Figure 4.25 shows TEM images of single-core nanoparticles that were thermally treated at 800 °C for 2 h.

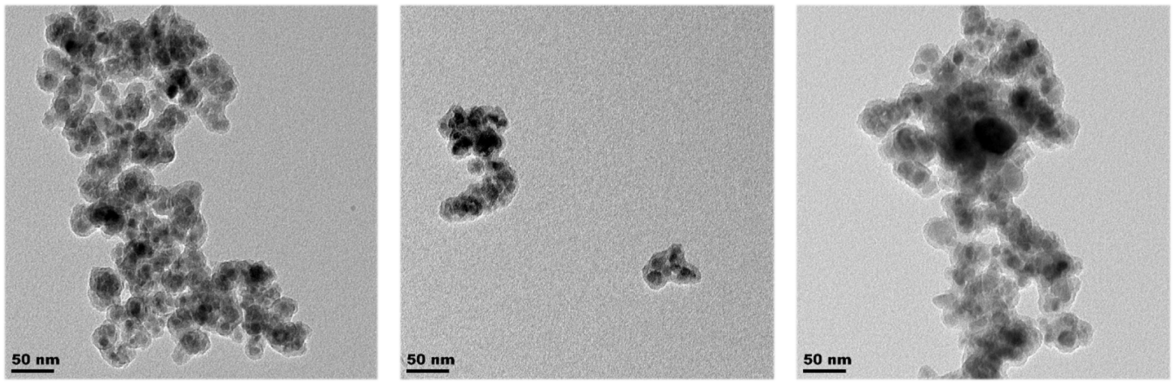

Figure 4.25: TEM images of thermally treated single-core silica-coated IONPs

This was done in order to remove any oxygen that might otherwise be emitted during carbonization. The nanoparticles appear to be very similar to the untreated single-core nanoparticles. Wojzik *et al*. has reported phase transition inside IONPs during thermal treatment at high temperatures that lead to the release of oxygen. At the temperatures employed during carbonization, released oxygen will oxidize the surrounding carbon matrix which will lead to the loss of fiber material. TEM imaging proved that the nanoparticles are still intact and in particle form: dark cores are seen surrounded by

shells of a lighter shade. Clearly the core-shell structure of the nanoparticles did not change during thermal treatment.

4.7 Particle diameters

Particle diameter data, as measured by TEM imaging, is reported in *Table 4.7*.

Table 4.7:

Particle diameter, standard deviation and relative standard deviation of synthesized nanoparticles as determined by TEM

Sample	Particle diameter (nm)	Standard deviation (nm)	Relative standard deviation (%)
IONPs	10.2	2.4	23.1
Multi-core IONPs	62.6	12.5	19.9
Single-core particles	22.2	4.3	19.5
Thermally treated single-core particles	21.7	4.2	19.3

Even though the particle diameters differed, the relative standard deviation of the particle diameter is very similar for multi- and single-core nanoparticles synthesized using different reaction parameters. The measured decrease in particle diameter due to thermal treatment of the single-core nanoparticles is very small at 0.5 nm and lies well within the standard deviations of both thermally treated and untreated nanoparticles.

The WAXD diffraction pattern of IONPs was used to determine the particle diameter by making use of the Scherrer equation.[19] The particle diameter, as determined using WAXD, was 12.7 nm. The discrepancy between the WAXD result and that of TEM analysis is due to instrumental line broadening which was not compensated for, but nevertheless the values are reasonably close.

4.8 Iron oxide and silica content of nanoparticles

Results of gravimetric analysis of the silica coating reactions are shown in *Table 4.8*.

Table 4.8:

Silica coating reaction parameters of IONP concentration and TEOS concentration as well as percentage silica contained in the product

Sample	IONPs (wt.%)	TEOS (M)	Percentage silica (wt.%)
Multi-core silica-coated NPs	0.18	7.2×10^{-2}	72.2
Silica-coated IONPs_1	0.02	4.5×10^{-2}	76.4
Silica-coated IONPs_2	0.02	2.7×10^{-2}	90.6
Silica-coated IONPs_3	0.02	9.0×10^{-3}	94.1
Single-core silica-coated IONPs	0.02	2.3×10^{-3}	29.6

The analysis was done by weighing of the dried powder product and calculating the increase in mass during the reaction. This increase, as a percentage of the final weight, is the percentage silica present. A clear trend is seen as a higher amount of TEOS leads to a larger mass of silica in the product when all other parameters are kept constant. In this way the total mass of silica in the final product can be controlled in order to obtain a thin silica shell and thereby synthesize nanoparticles consisting mainly of magnetic iron oxide that will ensure a high magnetization.

Diffraction patterns of WAXD analysis are presented in *Figure 4.26* for all but the thermally treated nanoparticles.

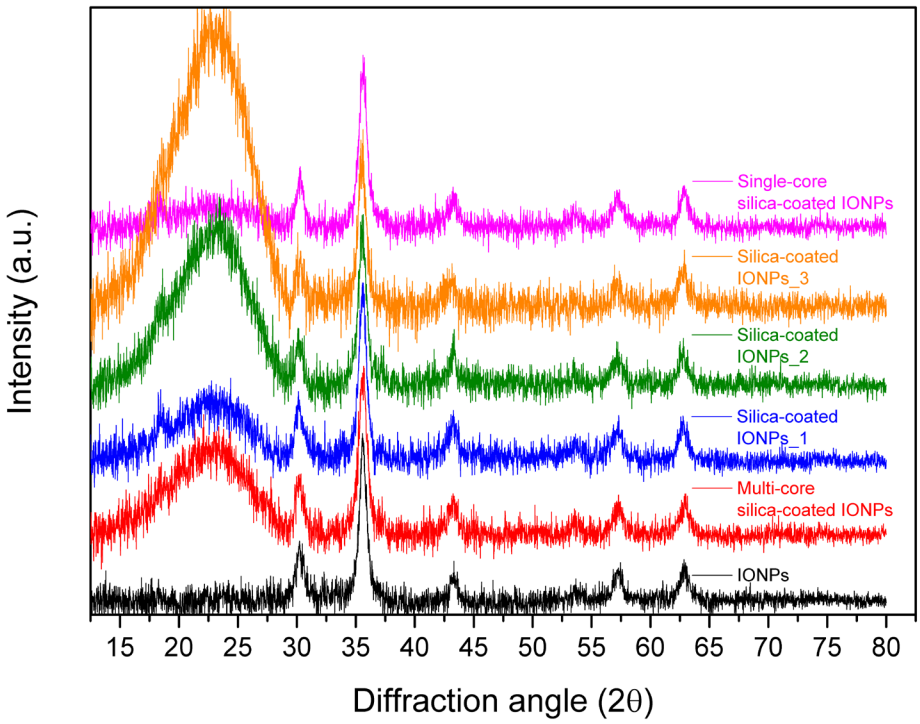

Figure 4.26: WAXD diffraction pattern overlay of IONPs (black) and silica-coated IONPs containing 72.2 wt.% (red), 76.4 wt.% (blue), 90.6 wt.% (green), 94.1 wt.% (orange) and 29.6 wt.% (pink) silica

Oxidation of the iron cores to iron oxide is inevitable due to the sample preparation inherent in WAXD analysis. The extent of oxidation during the time-frame of analysis is unknown and therefore WAXD of the thermally treated nanoparticles would not have given meaningful results in terms of iron oxide phases present. All the diffraction patterns show diffraction peaks corresponding to magnetite (Fe_3O_4) at 30.2° (2 2 0), 35.5° (3 1 1), 43.1° (4 0 0), 53.4° (4 2 2), 57.1° (5 1 1) and 62.6° (4 4 0) though the peak expected at 37.0° (2 2 2), which should be present in the diffraction pattern of magnetite, is not clearly visible.[20] Diffraction peaks of maghemite (γ-Fe_2O_3) are, however, very close to those of magnetite at 30.3° (2 2 0), 35.7° (3 1 1), 43.3° (4 0 0), 53.7° (4 2 2), 57.4° (5 1 1) and 63.0° (4 4 0).[20] It is, therefore, not clear whether magnetite, maghemite or both are present, though

it matters little. As discussed in *Chapter 2*, the high temperature employed during carbonization will cause phase transitions of the iron oxide after which the original phase is not of importance. Since the mass percentage of oxygen in magnetite and maghemite are similar at 27.6 % and 30.1 % respectively, the maximum amount of oxygen that can be released is very similar. All the silica-coated IONPs show a wide amorphous peak around 23.0° which is absent in the diffraction pattern of uncoated IONPs. This peak is due to the silica coating and has been observed in diffraction patterns of silica nanoparticles.[21]

4.9 Thermal stability of silica-coated nanoparticles

TGA was done on the single-core nanoparticles to investigate the mass loss during heating. The thermograms are shown in *Figure 4.27*.

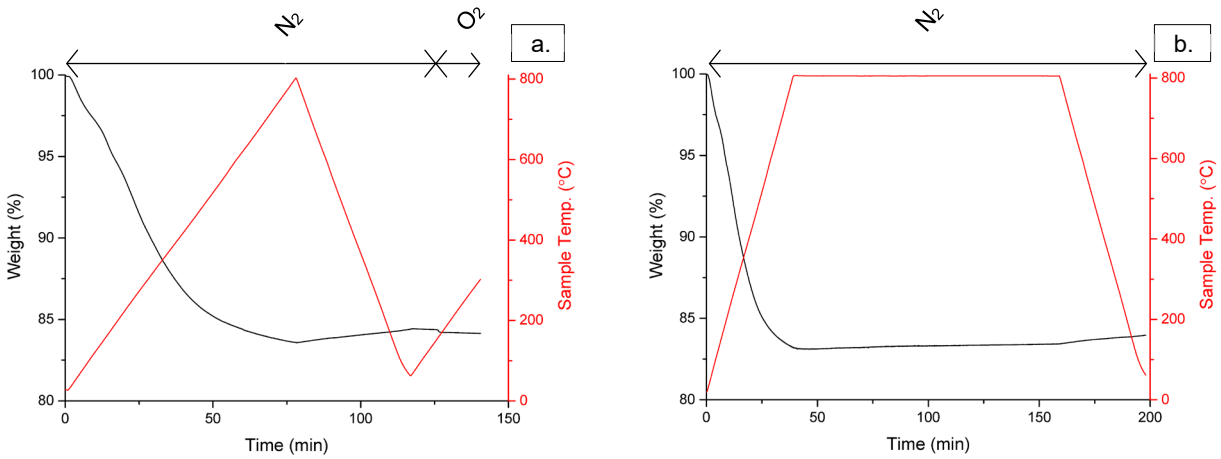

Figure 4.27: TGA thermograms of single-core nanoparticles heated to 800 °C followed by a) cooling to ambient temperature and subsequent heating to 300 °C in oxygen, b) an isothermal stage at 800 °C for 2 h

A gradual mass loss is seen up to 800 °C at which the total mass was 83.1 %. The mass loss is believed to be due to the evaporation of residual solvent not removed during drying in vacuo, i.e. water and ethanol, as well as the possible loss of oxygen from the iron oxide cores. During the first TGA run the atmosphere was changed to oxygen during the second heating cycle. No immediate gain in mass was noted which suggests a time-delay of oxidation of the nanoparticles. This time-delay was not investigated any further. The second TGA run was done in N_2 throughout and revealed a mass loss up to 800 °C at which the total mass was 83.6 %. The first and second TGA experiments essentially showed equal mass loss during heating. The mass loss does not increase over the following 2 h at 800 °C. This proves that the release of oxygen from the nanoparticles is immediate if it occurs at all. These results suggest that the synthesised single-core nanoparticles can be thermally treated, handled under an inert atmosphere and co-electrospun to prepare precursor nanofiber-nanoparticle composites.

ATR-FTIR spectra of the nanoparticles are shown in *Figure 4.28*.

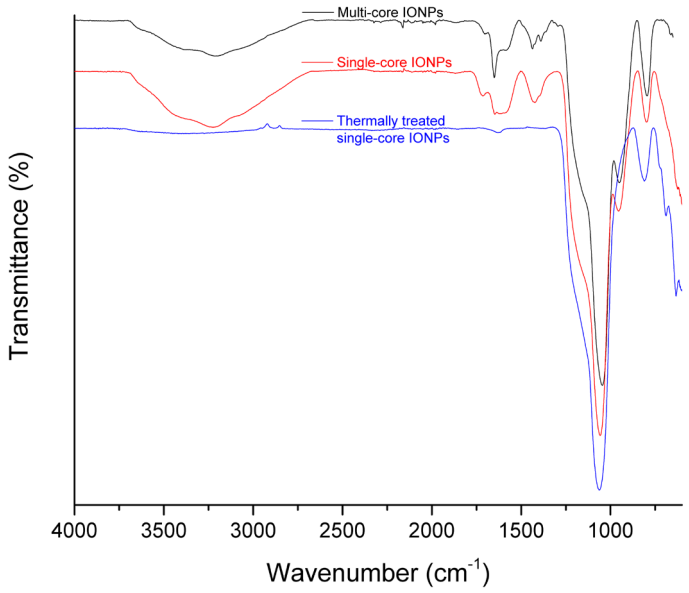

Figure 4.28: ATR-FTIR spectra of multi-core nanoparticles (black), single-core nanoparticles (red) and thermally treated single-core nanoparticles (blue)

A broad absorption peak is seen at 3215 cm^{-1} for the multi-core and single-core nanoparticles but not for the thermally treated single-core nanoparticles. This peak is associated with O-H stretch vibrations originating from residual water and ethanol used as solvent in the silica coating procedure.[21] The peak at 1650 cm^{-1} is associated with the O-H bending vibration in water.[22] The origin of the broad shoulder to the lower wavenumber region and the sharper, less intense shoulder in the higher wavenumber region of the peak at 1650 cm^{-1} is not known. An absorption associated with CH_2 bend vibrations is seen at 1440 cm^{-1} and another associated with CH_3 bend vibrations is seen at 1380 cm^{-1}.[3] This proves that water and ethanol are still present as residual solvents from the silica coating procedure. Disappearance of all these peaks after thermal treatment proves that the residual solvent not removed during drying in vacuo was removed during thermal treatment at 800 °C. This proves that the mass loss observed in TGA was at least in part due to the removal of residual solvent. The absorption peak at 1060 cm^{-1} and 800 cm^{-1} is due to silica Si-O-Si stretch vibrations.[22,20] The absorption peak at 960 cm^{-1} is due to Si-OH stretching vibrations of silanol groups.[23,24] The disappearance of this peak in addition to the disappearance of the O-H stretch absorption at 3215 cm^{-1} suggests that deprotonation of the silanol surface peaks occurred to a great extent during the thermal treatment. The absorption seen in the lowest wavenumber region of the spectra is believed to be part of an absorption peak that has reportedly been observed in IONPs.[24,25] The intensity of this absorption peak, being much greater for the single-core nanoparticles and thermally treated single-core nanoparticles than for the multi-core nanoparticles, is clearly proportional to the mass percentage iron oxide in the nanoparticles.

4.10 Nanoparticle aggregation

Results of zeta potential (ζ) measurements and DLS size measurements are shown in *Table 4.9*.

Table 4.9:

DLS results of zeta potential and size with respective standard deviations for synthesized nanoparticles

Sample	ζ (mV)	Standard deviation of ζ (mV)	Size (nm)	Standard deviation of size (nm)
Multi-core	-30.7	0.4	396.7	79.3
Single-core	-25.2	0.3	579.6	133.3
Thermally treated single-core	-25.7	0.9	870.9	117.5

Zeta potential measurements revealed large negative values as are expected of silica-coated nanoparticles.[11] This is to be expected as the surface charge originates from the silanol groups on the silica surfaces. Single-core nanoparticles as well as thermally treated single-core nanoparticles had similar values of zeta potential while that of the larger multi-core nanoparticles was greater negative. The concentration of the aqueous dispersion was 0.1 wt.%.

DLS size measurements do not correlate with size measurements done using TEM imaging. Measurements were done in triplicate. For all of the nanoparticles, DLS size measurements yielded values much greater than that obtained using TEM imaging. Considering different DLS measurements of the same sample, it is clear that the measured size is not stable. This suggests the formation of aggregates in solution. It is possible that the concentration of the samples, 1 % (g/ml), could have been above a critical aggregation concentration in water. This concentration is equal to that of the nanoparticles in the electrospinning solution of the nanocomposites, however, the solvent used during electrospinning was DMF and therefore a direct comparison would not be reasonable.

It has long been known that the zeta potential is a determining factor in the dispersion of nanoparticles in solution.[26] Even though the zeta potential of the larger multi-core nanoparticles is of a greater negative than the zeta potential of the single-core and thermally treated single-core nanoparticles, dispersion is not only dependent on electrostatic repulsions between particles in solution. Mackay *et al*. has demonstrated that the particle size also affects dispersion.[27] They have found that particles are better dispersed in a polymer matrix if their diameters are smaller than that of the surrounding polymer's radius of gyration.[27] From these arguments it is expected that smaller nanoparticles with a greater zeta potential will be better dispersed than larger nanoparticles with a

lower or equal zeta potential. It is therefore only by experiment that it can become clear which of the synthesized nanoparticles will be dispersed or agglomerated.

4.11 Polymer nanofiber-nanoparticle composites

4.11.1 Multi-core nanoparticle composites

TEM images of the electrospun homopolymer- and copolymer-based nanofiber-nanoparticle composites are shown in *Figure 4.29*.

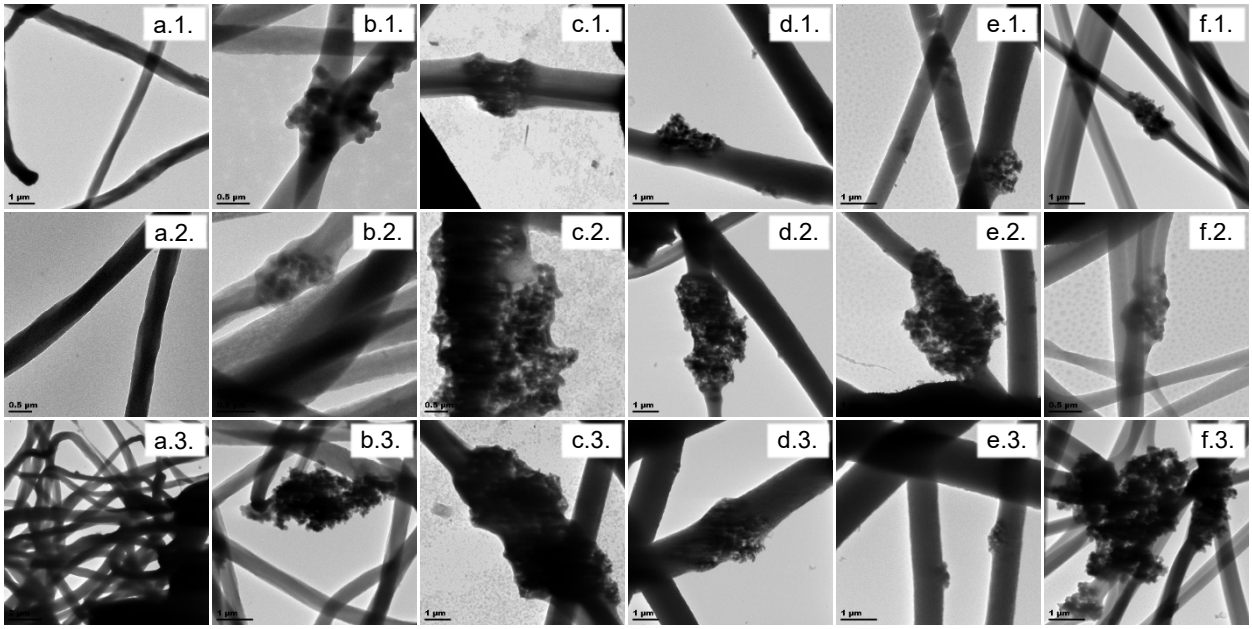

Figure 4.29: TEM images of precursor polymer nanofibers consisting of a) PAN homopolymer and precursor polymer nanofiber-nanoparticle composites consisting of b) PAN homopolymer and PAN-g-PDMS copolymers containing c) 3.7 wt.%, d) 8.4 wt.%, e) 13.5 wt.% and f) 18.5 wt.% 1 kDa PDMS grafts containing 10 wt.% multi-core nanoparticles

All nanofiber-nanoparticle composites were electrospun following the same procedure as that used in electrospinning of the pure polymer nanofibers with the exception that nanoparticles were added in a concentration of 10 wt.% w.r.t. the total solids content. The change in colour of the polymer-nanoparticle electrospinning solutions was clear: an opaque brown solution was obtained when nanoparticles were added compared to a transparent yellow colour of the pure polymer solution. TEM images show severe agglomeration of the nanoparticles. The nanoparticles are identified by their core-shell structure with the silica coating appearing as a lighter shade than the iron oxide cores. Very few nanoparticles can be observed in small clusters or in isolation outside the agglomerates. The agglomerates are often wider than the fiber diameter with the constituent nanoparticles. Constituent nanoparticles of the agglomerates appear to be covered by polymer. Although it is clear that the multi-core nanoparticles can be co-electrospun into nanofibers of PAN and PAN-g-PDMS copolymers, the low mass percentage of magnetic iron oxide in the nanoparticles make them less desirable for inducing magnetization.

4.11.2 Single-core nanoparticle composites

STEM images of the electrospun composites containing single-core nanoparticles are shown in *Figure 4.30.*

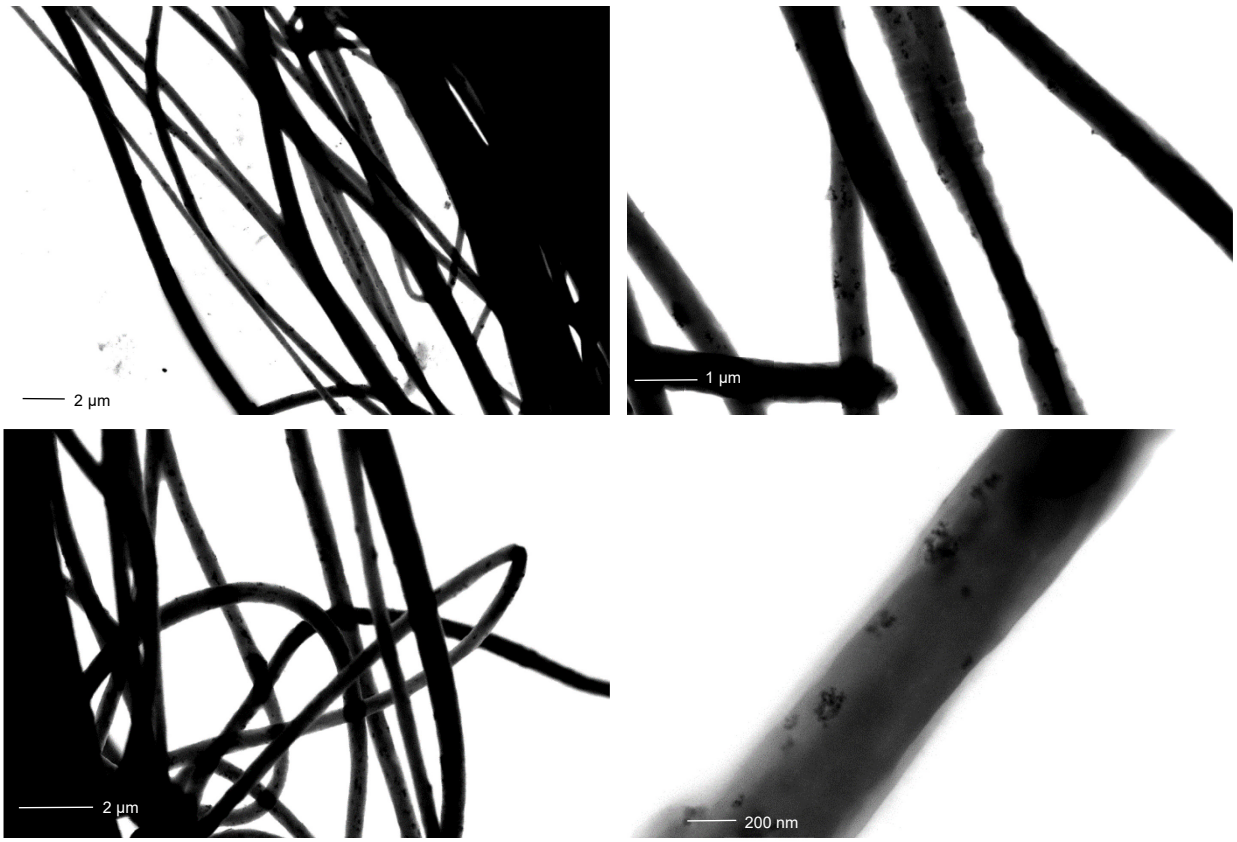

Figure 4.30: STEM images of precursor nanofiber-nanoparticle composites consisting of PAN homopolymer containing 10 wt.% single-core nanoparticles

Polymer solution preparation and subsequent electrospinning of nanofiber-nanoparticle composites containing single-core nanoparticles was carried out using 10 wt.% nanoparticles w.r.t. the total solids content as in the case of composites containing multi-core nanoparticles. STEM images of the fiber-particle composites revealed that nanoparticles are well-dispersed in the surrounding polymer matrix. Some small agglomerates can still be seen though none are wider than the fiber diameters. It is clear that nanoparticle dispersion is much better than in the case of the composites containing larger multi-core nanoparticles. Though the challenge of dispersion has been overcome by using nanoparticles with a diameter much smaller than that of the multi-core nanoparticles, the possibility of oxidation of the surrounding carbon matrix during the carbonization process still remains.

4.11.3 Thermally treated single-core nanoparticle composites

4.11.3.1 Dispersion

TEM images of nanocomposites containing thermally treated nanoparticles are shown in *Figure 4.31*.

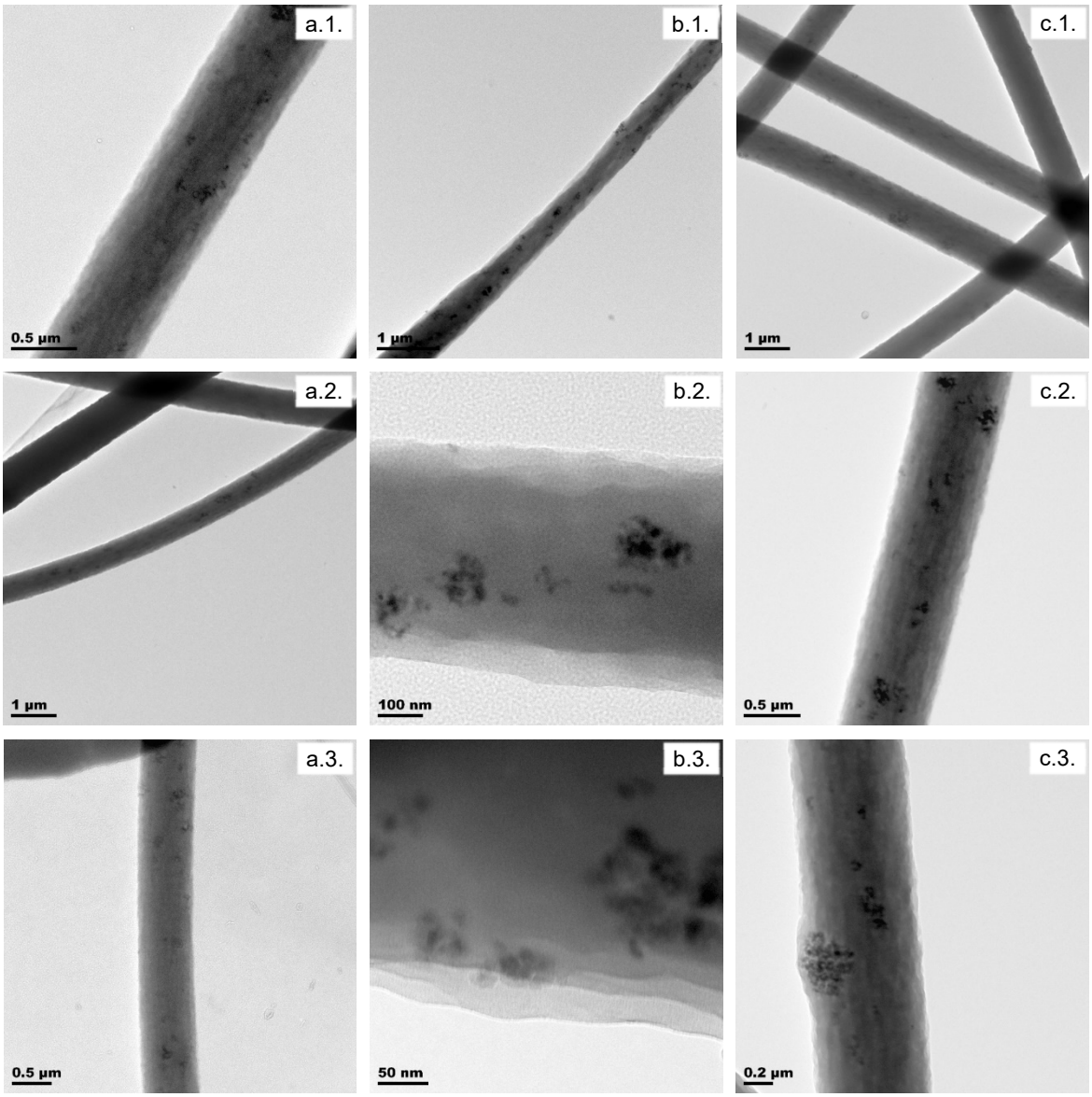

Figure 4.31: TEM images of precursor nanofiber-nanoparticle composites consisting of a) PAN homopolymer and PAN-g-PDMS containing 18.5 wt.% PDMS grafts electrospun b) immediately after solution preparation and c) 18 h after solution preparation containing 10 wt.% thermally treated single-core nanoparticles

After thermal treatment under argon at 800 °C for 2 h, electrospinning solutions were prepared under argon. Electrospinning was done in air, as all the previous electrospinning procedures, after which drying for 24 h in vacuo and subsequent carbonization were done immediately. TEM imaging of PAN homopolymer as well as PAN-g-PDMS copolymer nanofiber-nanoparticle composites electrospun without solution ageing (*a.* and *b.* in *Figure 4.33*) showed well-dispersed nanoparticles in the nanofibers. Some agglomerates and small clusters of nanoparticles were observed though not in abundance. PAN-g-PDMS copolymer fiber-particle nanocomposites electrospun after a solution ageing period of 18 h revealed some agglomerates comparable to the fiber diameter as well as

clusters of nanoparticles, yet most of the nanoparticles were well-dispersed in the polymer matrix. It is noteworthy that the aged electrospinning solutions showed precipitation of the nanoparticles at the bottom of the syringe used for electrospinning after the 18 h solution ageing period.

SEM images of the nanocomposites are shown in *Figure 4.32*.

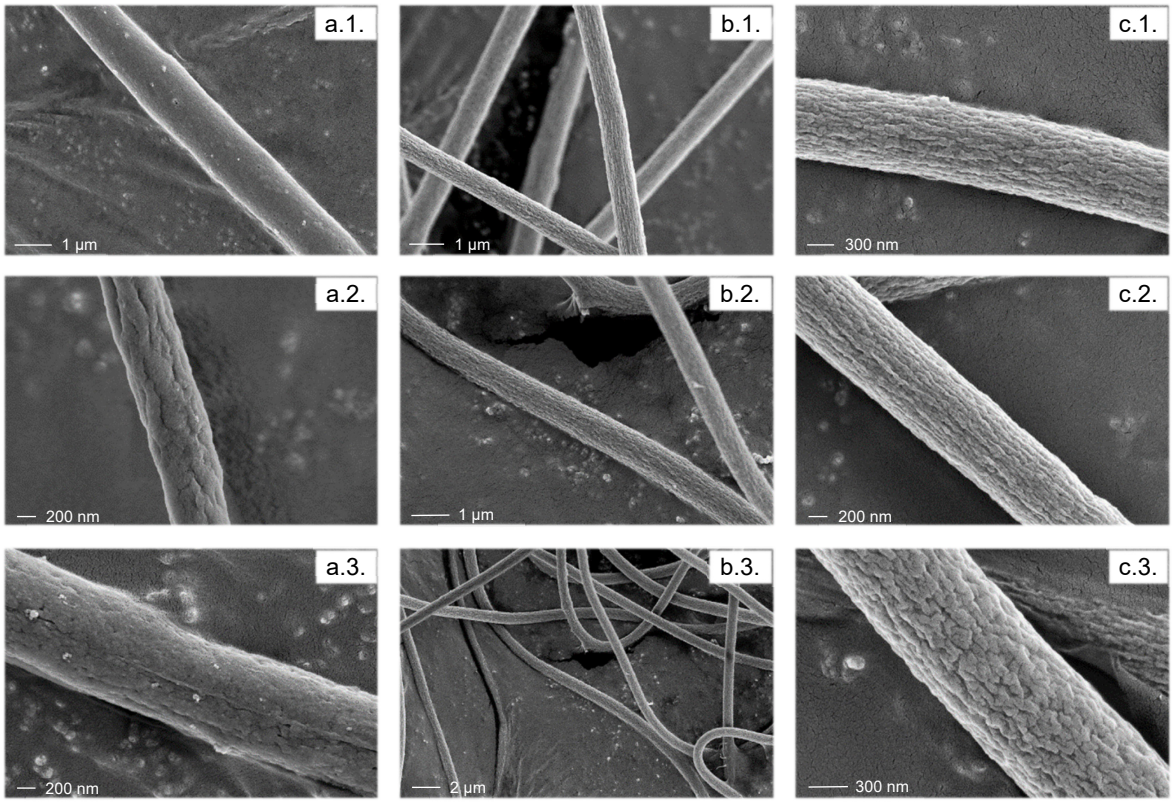

Figure 4.32: SEM images of precursor nanofiber-nanoparticle composites consisting of a) PAN homopolymer and PAN-g-PDMS copolymer containing 18.5 wt.% 1 kDa PDMS grafts electrospun b) immediately after solution preparation and c) 18 h after solution preparation containing 10 wt.% thermally treated single-core nanoparticles

SEM images revealed that the surface of the PAN-g-PDMS copolymer nanofiber composites are porous as in the absence of nanoparticles. Nanoparticles are seen on the surfaces only in the case of PAN nanofiber composites, although the surface roughness of the PAN-g-PDMS copolymer nanofiber composites makes it difficult to observe protruding nanoparticles.

As noted by Wojzik *et al*., IONPs will release oxygen at temperatures employed during carbonisation by means of phase transitions within the nanoparticle.[28] This process will lead to oxidation of the surrounding carbon material during carbonization of the polymer nanofiber-nanoparticle composites.

Thermal pre-treatment of the nanoparticles followed by solution preparation and electrospinning under an inert atmosphere is done in order to prevent the oxidation of iron oxide in the nanoparticles and thereby avoid the release of oxygen during carbonization of the nanocomposites.

4.11.3.2 ATR-FTIR of nanofiber-nanoparticle composites

ATR-FTIR spectra of the nanocomposites containing thermally treated nanoparticles are shown in *Figure 4.33*.

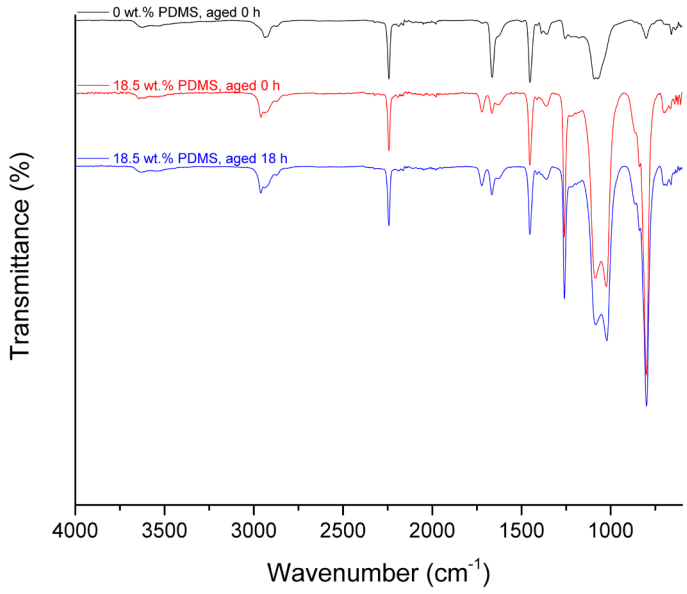

Figure 4.33: ATR-FTIR spectra of nanofiber-nanoparticle composites of a) PAN homopolymer (black) and PAN-g-PDMS copolymer containing 18.5 wt.% PDMS grafts electrospun b) immediately after solution preparation (red) and c) 18 h after solution preparation (blue) containing 10 wt.% thermally treated single-core nanoparticles

The sharp nitrile peak is seen at 2250 cm^{-1} for all three spectra.[3] The peaks at 1260 cm^{-1} and 800 cm^{-1} correspond to Si-CH_3 absorptions of the PDMS chains and is not seen for the PAN homopolymer nanocomposite.[29,30] Absorption peaks associated with silica are seen at 1080 cm^{-1} and 795 cm^{-1}, the second being immersed in a Si-CH_3 peak for the PAN-g-PDMS copolymers.[22,20] Two overlapping peaks, visible at 1090 cm^{-1} and 1025 cm^{-1} correspond to Si-O-Si stretch absorptions in PDMS.[30] Even though the absorption peaks associated with PDMS overlap severely with those associated with silica for the PAN-g-PDMS copolymer nanocomposites, silica peaks are clearly visible for the nanocomposite containing PAN homopolymer. A discussion of the rest of the peaks seen in the spectra can be found in *Appendix C*.

4.12 Carbonisation of polymer nanofiber-nanoparticle composites

4.12.1 Multi-core nanoparticle composites

TEM images of the carbonized products of the precursor nanocomposites containing multi-core nanoparticles are shown in *Figure 4.34*.

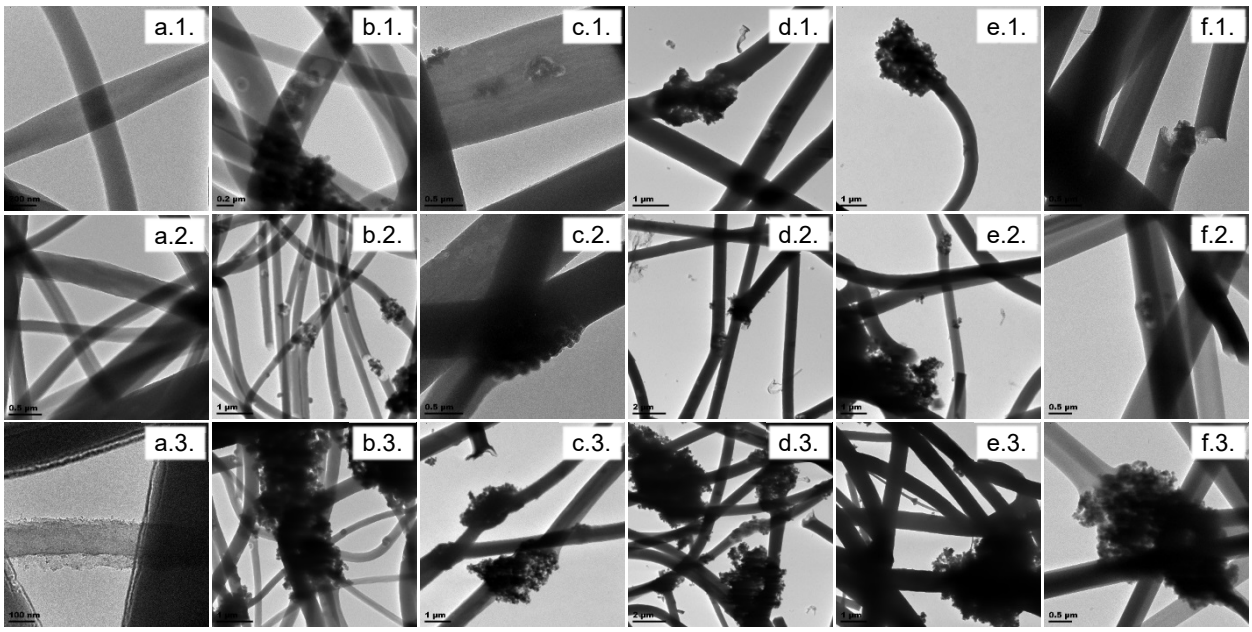

Figure 4.34: TEM images of a) carbon nanofiber prepared by carbonization of precursor nanofibers of PAN homopolymer and carbon nanofiber-nanoparticle composites prepared by carbonization of precursor fiber-particle nanocomposites consisting of b) PAN homopolymer and PAN-g-PDMS copolymers containing c) 3.7 wt.%, d) 8.4 wt.%, e) 13.5 wt.% and f) 18.5 wt.% 1 kDa PDMS grafts containing 10 wt.% multi-core nanoparticles

Carbonisation led to black fibrous membranes. TEM images revealed that severe agglomeration of the nanoparticles is still present in the carbonized nanofiber-nanoparticle composites as expected; the carbonization procedure does not seem to induce changes w.r.t. agglomeration of the nanoparticles. Silica-coated IONPs can still be identified. Cavities are formed around the nanoparticles that are seen in clusters. This suggests that the expected intra-particle reactions, reported by Wojzik *et al*., leading to the release of oxygen gas do occur.[28] At the high temperatures employed during the carbonization process, carbon material surrounding the nanoparticles is oxidized by the emitted oxygen and presumably forms gaseous decomposition products. TEM images showed fiber breakage and, in some cases, discharged nanoparticle agglomerates. The concave shape of fiber ends suggest that fiber breakage occurred around the nanoparticle agglomerates thereby discharging the nanoparticles from the encompassing fibers. Fiber breakage around an agglomerate might also occur due to stress caused by shrinkage of the nanofiber mat during carbonization or during subsequent handling of the samples. Agglomerates are expected to cause weak points in the fibers and thereby impair the structural integrity of the carbon fiber membrane. Nanoparticles do not act as binding material such as polymers in the precursor nanofibers or graphene in the carbon nanofibers. Additionally, the oxidation of binding material surrounding the nanoparticles, mentioned earlier, further weaken the carbon nanofibers. Even though fiber breakage does occur, the carbonized fiber membrane is still intact and can easily be handled.

A digital photograph of the carbon fiber membrane containing multi-core nanoparticles is shown in *Figure 4.35*.

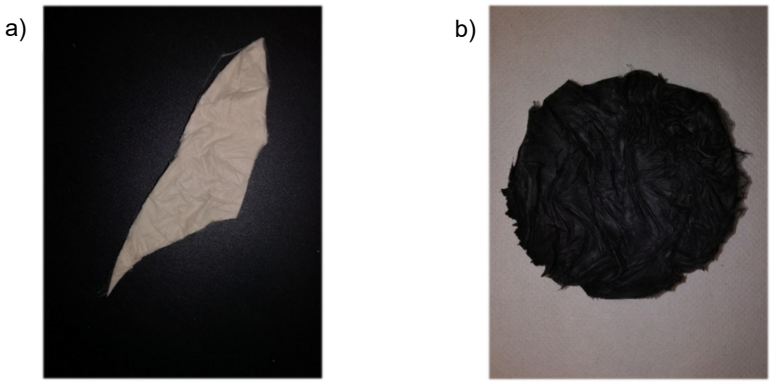

Figure 4.35: Digital photographs of a) electrospun precursor nanofiber-nanoparticle composites of PAN-g-PDMS containing 18.5 wt.% PDMS grafts and multi-core nanoparticles as well as b) carbonized product

Severe agglomeration causes weakening of the fiber membrane and, therefore, the necessity for nanocomposites containing well-dispersed nanoparticles is evident.

4.12.2 Single-core nanoparticle composites

STEM images of carbonized products of single-core nanoparticle composites are shown in *Figure 4.36*.

STEM images revealed very little intact fibrous material. Where nanofibers sections are seen intact, voids can be seen inside the nanofibers around incorporated nanoparticles. The observed voids are similar to those in the carbonized nanocomposites that contained multi-core nanoparticles. These voids are created by the release of oxygen from the iron oxide cores of the nanoparticles during the transition to different phases. The difference between the carbonized products of precursors of multi- and single-core nanoparticle composites is presumably due to the difference in dispersion of the nanoparticles. In the event that every nanoparticle is well-dispersed, immersed in the fiber and not in a cluster of particles, oxygen released from each particle will oxidize the surrounding carbon material during carbonization. In terms of oxidation, this will entail the most efficient use of released oxygen in oxidizing the surrounding carbon material. In contrast, nanoparticle agglomerates will be discharged from the nanofibers, as seen in the case of the larger multi-core nanoparticle composites, after which further oxygen release will have no effect. This explains why very little fibrous material remains intact in the case of single-core nanoparticles whereas multi-core nanoparticles, causing severe agglomeration, led to a mainly intact fiber membrane with various points of fiber breakage. It is noteworthy, however, that the amount of iron oxide present inside the nanofibers is greater in the

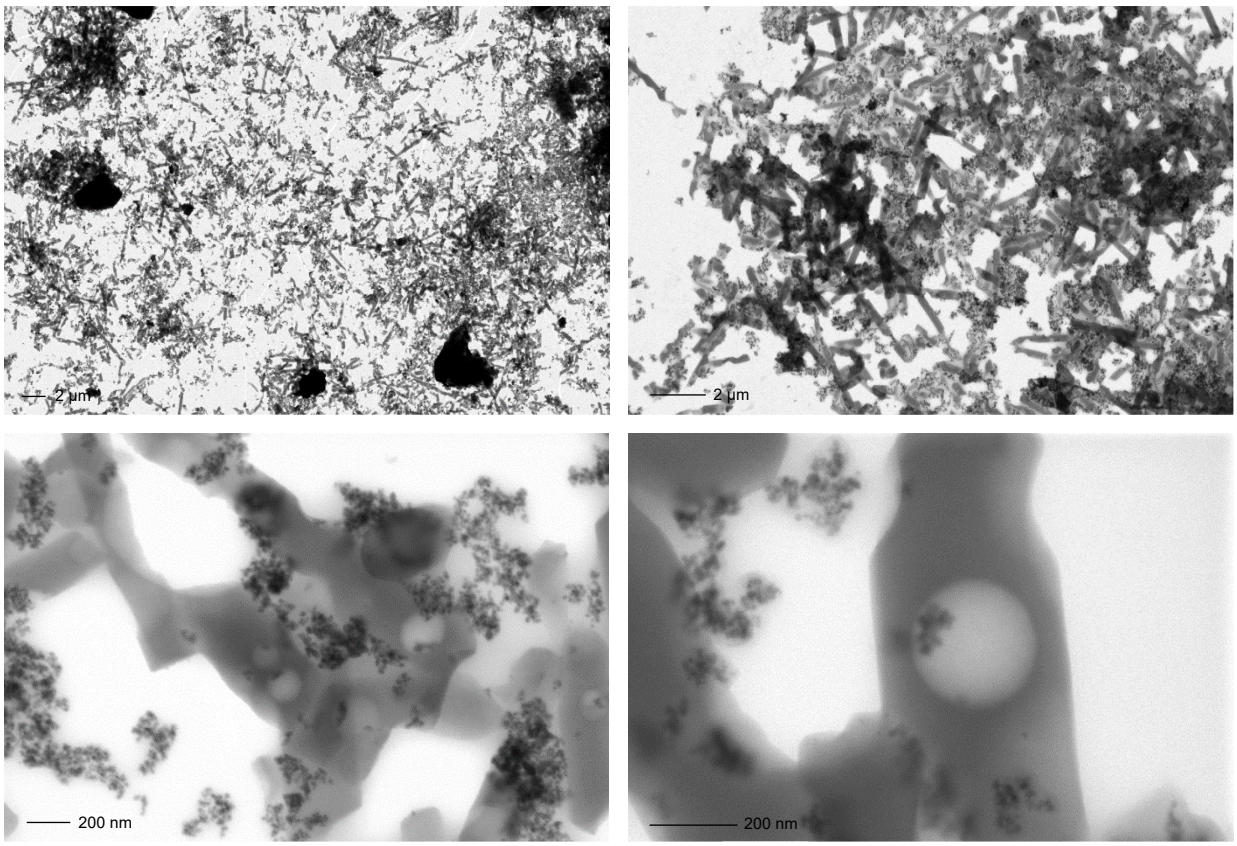

Figure 4.36: STEM images of carbonized products prepared by carbonization of precursor nanofiber-nanoparticle composites consisting of PAN homopolymer containing 10 wt.% single-core nanoparticles

case of the single-core nanoparticles due to the larger mass percentage of iron oxide because of the different reaction parameters of the silica coating procedure.

Carbonisation of single-core nanoparticle composites led to a black powder of which a digital photograph is shown in *Figure 4.37*.

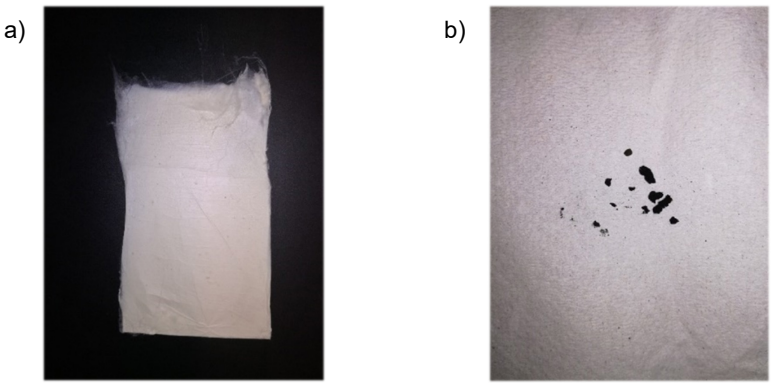

Figure 4.37: Digital photographs of a) electrospun precursor nanofiber-nanoparticle composites of PAN-g-PDMS containing 18.5 wt.% PDMS grafts and single-core nanoparticles as well as b) carbonized product

Evidently, well-dispersed silica-coated IONPs presents challenges of its own in terms of carbonization. Oxidation of the carbon material surrounding the nanoparticles must be prevented if carbon nanocomposites are to be produced.

4.12.3 Thermally treated single-core nanoparticle composites

TEM images of the carbonized products of thermally treated single-core nanoparticle composites are shown in *Figure 4.38*.

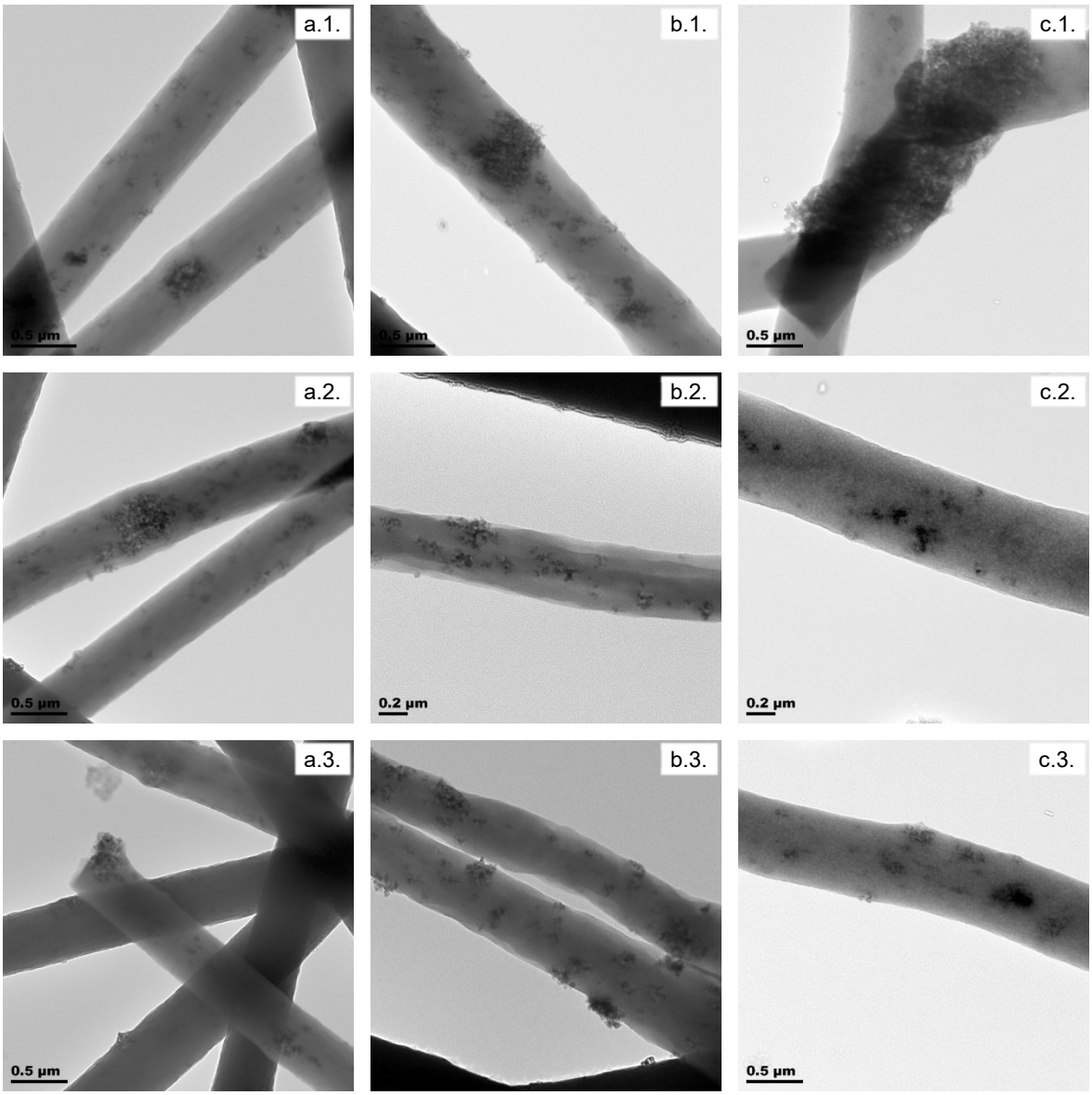

Figure 4.38: TEM images of carbon nanofiber-nanoparticle composites prepared by carbonization of precursor fiber-particle nanocomposites consisting of a) PAN homopolymer and PAN-g-PDMS containing 18.5 wt.% 1 kDa PDMS grafts electrospun b) immediately after solution preparation and c) 18 h after solution preparation containing 10 wt.% thermally treated single-core nanoparticles

TEM imaging revealed that the nanoparticles are still well-dispersed inside the nanofibers after carbonization. Some particle agglomerates are seen, yet they are still attached to the nanofibers. No evidence of oxidation of the nanofibers can be seen. This suggests that the nanoparticle cores did not oxidize to the original iron oxide phase during solution preparation, electrospinning, in vacuo drying of the electrospun fiber membrane or during the first step of the carbonization procedure which occurs in air.

Carbonisation of the nanocomposites containing thermally treated single-core nanoparticles led to black fibrous membranes of which a digital photograph is shown in *Figure 4.39*.

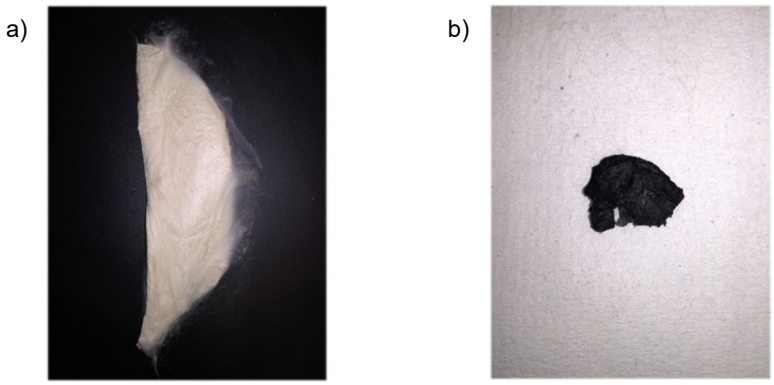

Figure 4.39: Digital photographs of a) electrospun precursor nanofiber-nanoparticle composites of PAN-g-PDMS containing 18.5 wt.% PDMS grafts and thermally treated single-core nanoparticles as well as b) carbonized product thereof

STEM images of the carbonized nanocomposites are shown in *Figure 4.40*.

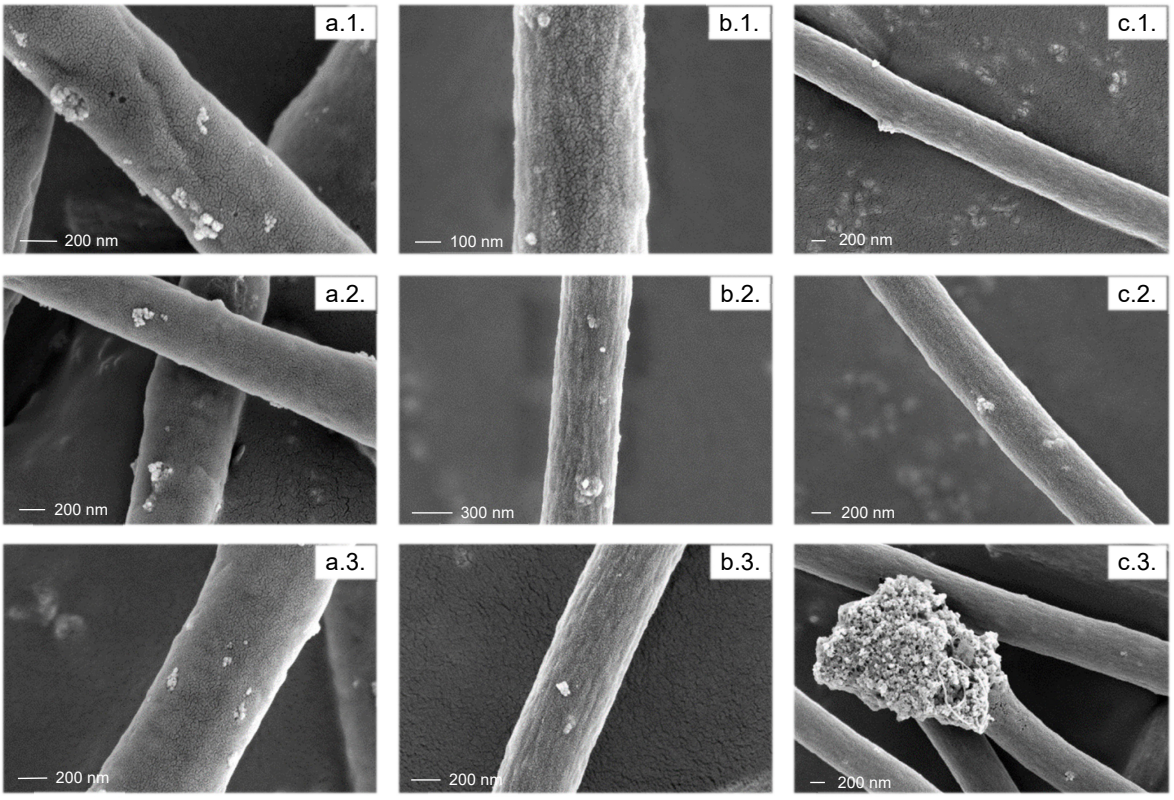

Figure 4.40: STEM images of carbon nanofiber-nanoparticle composites prepared by carbonization of precursor fiber-particle nanocomposites consisting of a) PAN homopolymer and PAN-g-PDMS containing 18.5 wt.% 1 kDa PDMS grafts electrospun b) immediately after solution preparation and c) 18 h after solution preparation containing 10 wt.% thermally treated single-core nanoparticles

The images revealed nanoparticles protruding from the surfaces of the nanofibers for composites of PAN homopolymer as well as for the PAN-g-PDMS copolymer containing 18.5 wt.% PDMS grafts electrospun immediately and after 18 h of solution ageing. The nanoparticles may be visible in the

case of the carbonized nanocomposites produced by carbonization of the copolymer-based precursors due to shrinkage of the fibers during carbonization that makes protruding nanoparticles more visible than in the case of the precursors. It is clear that thermal pre-treatment of the silica-coated IONPs followed by polymer solution preparation under non-oxidizing conditions, electrospinning and carbonization yield carbon nanofiber-nanoparticle composites by avoiding oxidation owed to oxygen released from iron oxide cores in the nanoparticles during carbonization.

4.13 Sorption capacity of carbon nanofiber-nanoparticle composites

The carbon nanofiber-nanoparticle composites produced by carbonization of precursor fiber-particle nanocomposites containing 18.5 wt.% 1 kDa PDMS grafts and 10 wt.% thermally treated nanoparticles were used for sorption capacity tests. Results are shown in *Figure 4.41* along with the initial absorption of a carbon nanofiber membrane without nanoparticles for comparison.

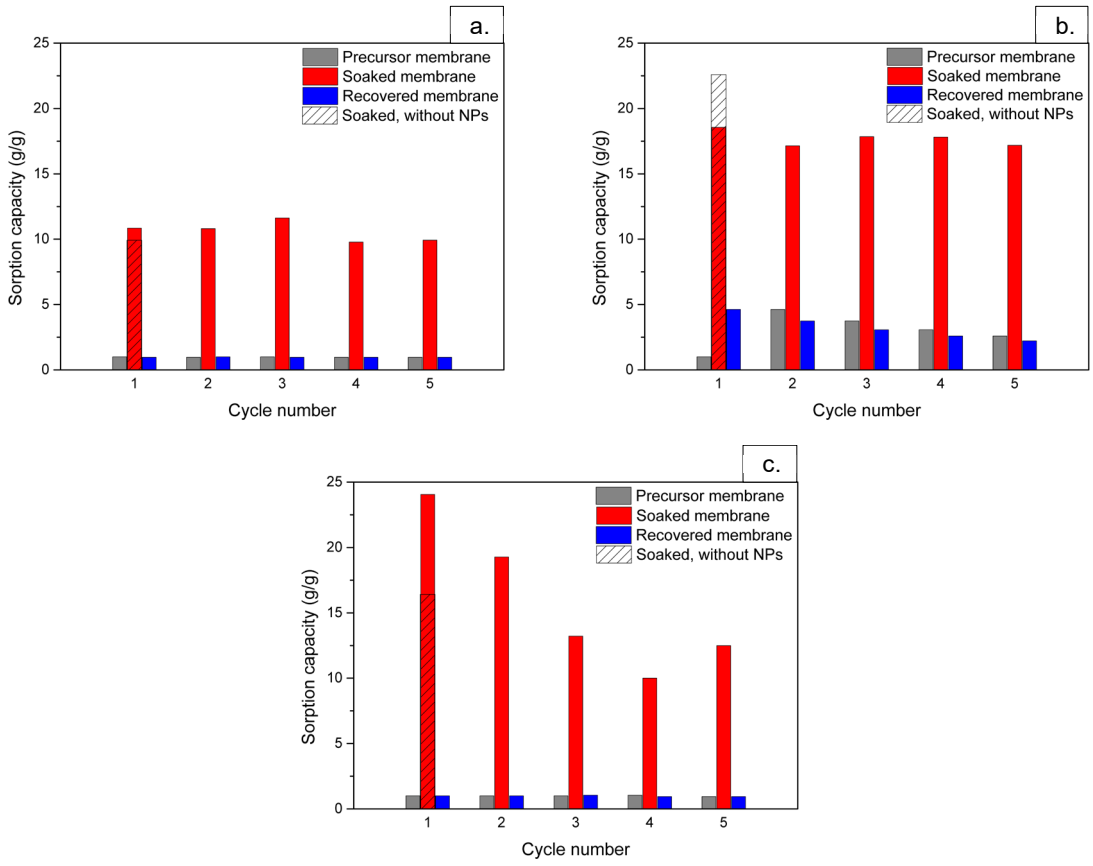

Figure 4.41: Sorption capacity of carbon nanofiber-nanoparticle composite membrane towards a) hexane, b) silicon oil and c) water calculated as a percentage of the initial fiber membrane. The striped bar shows absorption of the carbon nanofiber membrane during the first use

Water, hexane and silicon oil were tested for sorption. It is expected that the oleophilic nature of carbon nanofibers would induce capillary action through which the composite membrane will be filled with liquid.[1,31] The composite membrane showed the largest sorption capacity towards water followed by silicon oil and then hexane, initially absorbing respectively 24 times, 18 times and 10

times its own mass. This result is surprising, since carbon nanofibers are known to selectively absorb organic impurities from water by having a much lower sorption capacity towards water.[1] The fiber membrane did, however, show a much greater absorption of oil (23 g/g) and less absorption of water (16 g/g) while showing similar absorption of hexane (10 g/g). Clearly there is a difference between the material comprising these two membranes. While the fiber membrane is essentially fully recovered after sorption capacity testing of water and hexane, recovery after sorption testing of silicon oil is not as effective. This shows that even though evaporation of hexane and water was effective, the hexane wash of the fiber membrane after sorption of silicon oil was not effective in removing all of the absorbed silicon oil. Incomplete recovery of the fiber membrane has been reported by Human.[1]

The rate of absorption of red colored water from a capillary tube is demonstrated in *Figure 4.42*.

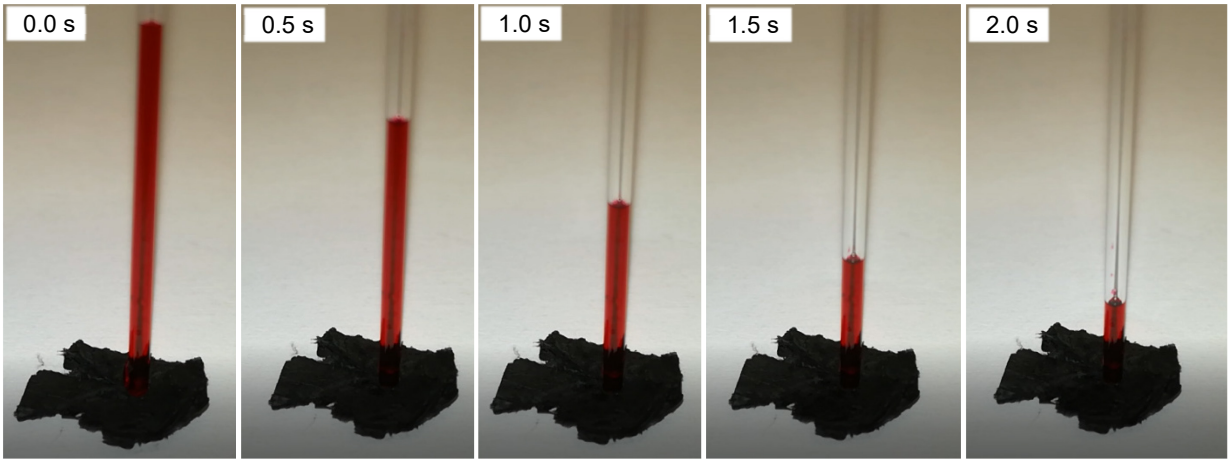

Figure 4.42: Demonstration of the rate of water (colored red) absorption of the carbon nanofiber-nanoparticle composite membrane

It is clear from the rate of absorption that capillary action must be involved in the absorption process. Therefore, the fiber membrane clearly has an affinity for water. This is in stark contrast to the results presented by Human for similar material produced in the absence of the silica-coated nanoparticles.

The rate of absorption of silicon oil from a capillary tube is demonstrated in *Figure 4.43*.

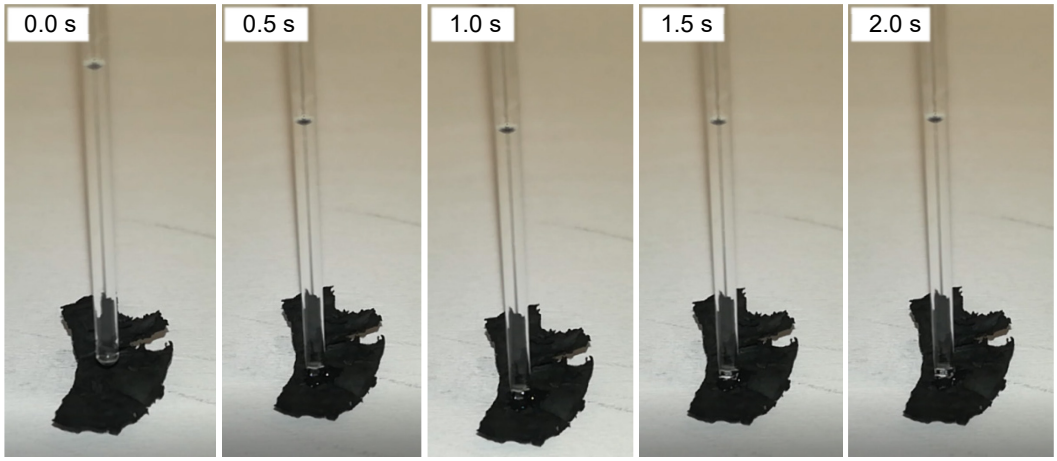

Figure 4.43: Demonstration of the rate of silicon oil absorption of the carbon nanofiber-nanoparticle composite membrane

Over the initial 2.0 s period, very little silicon oil is absorbed. Compared to the rate of water absorption demonstrated in *Figure 4.44*, the absorption of silicon oil is very slow.

To investigate the possibility of an increase in hydrophilic groups after carbonization, a section of the composite membrane and a section of the carbon fiber membrane were thermally treated at 800 °C for 2 h and analysed with ATR-FTIR immediately along with the untreated membranes.

ATR-FTIR spectra of the carbon fiber membrane, thermally treated carbon fiber membrane, carbon fiber-particle nanocomposites, and thermally treated carbon fiber-particle nanocomposites are shown in *Figure 4.44*.

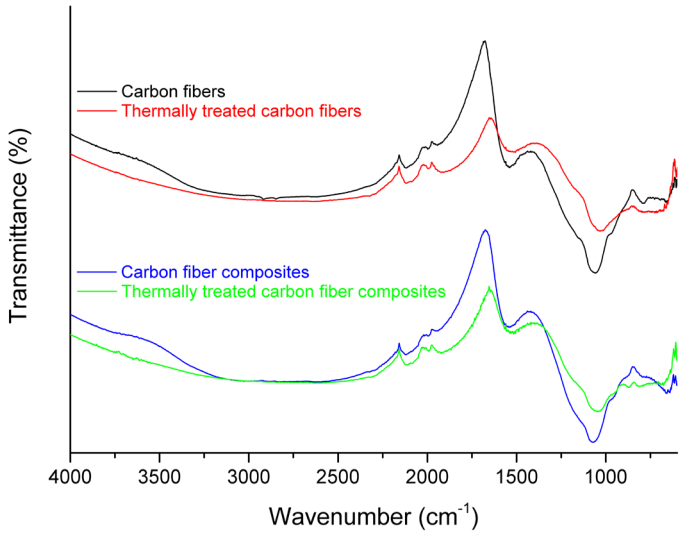

Figure 4.44: ATR-FTIR spectra of carbon nanofibers (black), thermally treated carbon nanofibers (red), carbon fiber-particle nanocomposites (blue), and thermally treated carbon fiber-particle nanocomposites (green)

The peak at 1535 cm^{-1} is believed to originate from aromatic C=C absorptions. An intense peak is seen at 1065 cm^{-1} for both the composite membrane and the carbon fiber membrane. This peak is associated with silica.[22] Considering work by Camino *et al.*, PDMS would have been decomposed into volatile products or would have formed silica during the thermal procedure.[9] Thus, both carbon fiber membranes contain silica after carbonization. Due to the incorporation of silica-coated nanoparticles, the carbon fiber composite is expected to contain a larger amount of silica since the same copolymer, containing 18.5 wt.% PDMS grafts, was used for the precursor nanofibers. This explains why the composite membrane has a larger sorption capacity towards water than the fiber membrane without silica-coated nanoparticles. The difference in PDMS graft content can possibly be the reason Human did not observe such hydrophilic properties since copolymers containing 12.1 wt.% PDMS grafts were used.[1] The difference in amount of PDMS graft content is not large, but due to the large mass loss of PAN sections inherent in the carbonization process, this difference of 6.4 wt.% might be much more significant in the carbonized product. The fact that the same peaks, though of different shapes and intensities, were seen in the as-carbonized and the thermally treated carbonized products shows that there are no additional functional groups forming after carbonization due to exposure to ambient conditions.

4.14 Magnetization of carbon nanofiber-nanoparticle composites

A demonstration of the magnetization of the carbon fiber-particle nanocomposite membrane containing thermally pre-treated nanoparticles is shown in *Figure 4.45*.

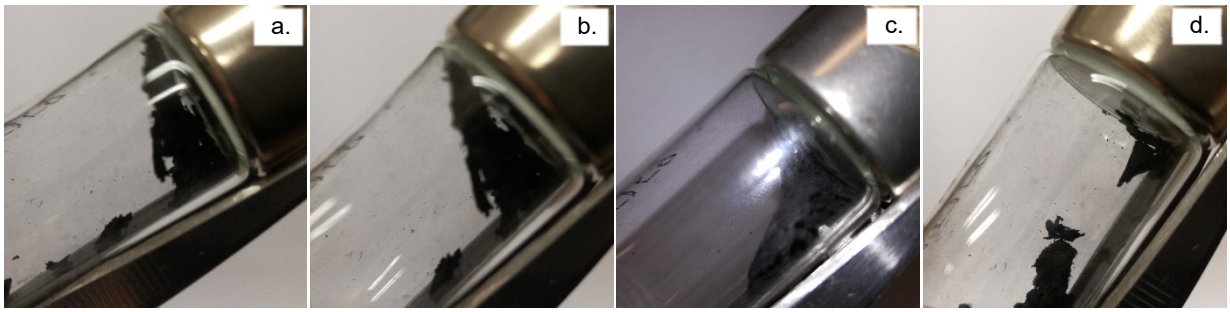

Figure 4.45: Demonstration of magnetism of carbon fiber-particle nanocomposite membrane

As can be seen from the inability of the carbon fiber-particle nanocomposite membrane to remain close to the magnet under influence of gravity, the fiber membrane clearly does not show a high magnetization.

Ultimately, hydrophilic carbon fiber-particle nanocomposite membranes with a low magnetization were produced. This was due to components of the precursor fiber membrane that did not carbonize but rather formed hydrophilic materials as well as intra-particle reactions in the iron oxide cores that led to nanoparticles with a low magnetization.

References

1. Human, C. Facile method for producing silicon containing porous carbon nanofibres from amphiphilic copolymers and controlling precursor fibre morphology, MSc Thesis. (Stellenbosch University, 2015).
2. Bayley, G. M. & Mallon, P. E. Porous microfibers by the electrospinning of amphiphilic graft copolymer solutions with multi-walled carbon nanotubes. *Polym. (United Kingdom)* **53**, 5523–5539 (2012).
3. Lampman, G. M., Pavia, D. L., Kriz, G. S. & Vyvyan, J. R. *Spectroscopy, 4th International Edition*. (Brooks-Cole, 2010).
4. Basson, N. Free volume of electrospun organic-inorganic copolymers, MSc Thesis. (Stellenbosch University, 2014).
5. Bayley, G. M., Hedenqvist, M. & Mallon, P. E. Large strain and toughness enhancement of poly(dimethyl siloxane) composite films filled with electrospun polyacrylonitrile-graft-poly(dimethyl siloxane) fibres and multi-walled carbon nanotubes. *Polym. (United Kingdom)* **52**, 4061–4072 (2011).
6. Shenoy, S. L., Bates, W. D., Frisch, H. L. & Wnek, G. E. Role of chain entanglements on fiber formation during electrospinning of polymer solutions: good solvent, non-specific polymer-polymer interaction limit. *Polymer (Guildf).* **46**, 3372–3384 (2005).
7. Eom, Y. & Kim, B. C. Solubility parameter-based analysis of polyacrylonitrile solutions in N,N-dimethyl formamide and dimethyl sulfoxide. *Polym. (United Kingdom)* **55**, 2570–2577 (2014).
8. Fitzer, E. *et al. Ullmann's Encyclopeida of Industrial Chemistry*. (Wiley-VCH Verlag GmbH & Co. KGaA, 2011).
9. Camino, G., Lomakin, S. M. & Lazzari, M. Polydimethylsiloxane thermal degradation Part 1. Kinetic aspects. *Polymer (Guildf).* **42**, 2395–2402 (2001).
10. Sun, Y., Ma, M., Zhang, Y. & Gu, N. Synthesis of nanometer-size maghemite particles from magnetite. *Colloids Surfaces A Physicochem. Eng. Asp.* **245**, 15–19 (2004).
11. Bumb, A. *et al.* Synthesis and characterization of ultra-small superparamagnetic iron oxide nanoparticles thinly coated with silica. *Nanotechnology* **19**, 335601 (2008).
12. Shen, L., Laibinis, P. E. & Hatton, T. A. Bilayer Surfactant Stabilized Magnetic Fluids: Synthesis and Interactions at Interfaces. *Langmuir* **15**, 447–453 (1999).
13. Fortuin, L. Modified chitosan nano-substrates for mycobacterial capture, MSc Thesis. (Stellenbosch University, 2015).
14. Lakay, E. M. Superparamagnetic iron-oxide based nanoparticles for the separation and recovery of precious metals from solution, MSc Thesis. (Stellenbosch University, 2009).
15. Vatta, L. L., Kramer, J. & Koch, K. R. Diethylenetriamine Functionalized Silica Coated Magnetite Nanoparticles for Selective Palladium Ion Extraction from Aqueous Solutions. *Sep. Sci.*

Technol. **42**, 1985–2002 (2007).

16. Deng, Y. H., Wang, C., Hu, J., Yang, W. & Fu, S. Investigation of formation of silica-coated magnetite nanoparticles via sol-gel approach. *Colloids Surfaces A Physicochem. Eng. Asp.* **262**, 87–93 (2005).

17. Tadyszak, K. *et al.* Spectroscopic and magnetic studies of highly dispersible superparamagnetic silica coated magnetite nanoparticles. *J. Magn. Magn. Mater.* **433**, 254–261 (2017).

18. Lu, Y., Yin, Y., Mayers, B. T. & Xia, Y. Modifying the Surface Properties of Superparamagnetic Iron Oxide Nanoparticles through A Sol-Gel Approach. *Nano Lett.* **2**, 183–186 (2002).

19. Patterson, A. L. The Scherrer Formula for X-Ray Particle Size Determination. *Phys. Rev.* **56**, 978–982 (1939).

20. Fajaroh, F., Setyawan, H., Nur, A. & Lenggoro, I. W. Thermal stability of silica-coated magnetite nanoparticles prepared by an electrochemical method. *Adv. Powder Technol.* **24**, 507–511 (2013).

21. Nandawar, R., Singh, P. & Haque, F. Z. Synthesis and Characterization of SiO2 Nanoparticles by Sol-Gel Process and Its Degradation of Methylene Blue. *Am. Chem. Sci. J.* **5**, 1–10 (2015).

22. Beganskienė, A., Sirutkaitis, V., Kurtinaitienė, M., Juškėnas, R. & Kareiva, A. FTIR, TEM and NMR Investigations of Stöber Silica Nanoparticles. *Mater. Sci.* **10**, 287–290 (2004).

23. White, L. D. & Tripp, C. P. Reaction of (3-Aminopropyl)dimethylethoxysilane with Amine Catalysts on Silica Surfaces. *J. Colloid Interface Sci.* **232**, 400–407 (2000).

24. Bini, R. A., Marques, R. F. C., Santos, F. J., Chaker, J. A. & Jafelicci, M. Synthesis and functionalization of magnetite nanoparticles with different amino-functional alkoxysilanes. *J. Magn. Magn. Mater.* **324**, 534–539 (2012).

25. Sahoo, S. K., Agarwal, K., Singh, A. K., Polke, B. G. & Raha, K. C. Characterization of γ- and α-Fe_2O_3 nano powders synthesized by emulsion precipitation-calcination route and rheological behaviour of α-Fe_2O_3. *Int. J. Eng. Sci. Technol.* **2**, 118–126 (2010).

26. Verwey, E. J. W. Theory of the stability of lyophobic colloids. *J. Phys. Colloid Chem.* **51**, 631–636 (1947).

27. Mackay, M. E. *et al.* General Strategies for Nanoparticle Dispersion. *Science (80-.).* **311**, 1740–1743 (2006).

28. Wojcik, M., Chmist, J., Przewoznik, J., Figiel, H. & Blazewicz, S. Magnetic properties of PAN-based carbon fibres modified with magnetite nanoparticles. *Carbon N. Y.* **50**, 1604–1613 (2012).

29. Flichy, N. M. B., Kazarian, S. G., Lawrence, C. J. & Briscoe, B. J. An ATR-IR Study of Poly (Dimethylsiloxane) under High-Pressure Carbon Dioxide: Simultaneous Measurement of Sorption and Swelling. *J. Phys. Chem. B* **106**, 754–759 (2002).

30. Sankir, M., Küçükyavuz, Z. & Küçükyavuz, S. Synthesis and Characterization of

Poly(dimethylsiloxane)– Polythiophene Composites. *J. Appl. Polym. Sci.* **87**, 2113–2119 (2003).

31. Tai, M. H., Tan, B. Y. L., Juay, J., Sun, D. D. & Leckie, J. O. A Self-Assembled Superhydrophobic Electrospun Carbon-Silica Nanofiber Sponge for Selective Removal and Recovery of Oils and Organic Solvents. *Chem. - A Eur. J.* **21**, 5395–5402 (2015).

Chapter 5: Conclusions and Recommendations for future work

Conclusions of the conducted research are summarized. Recommendations for future research are suggested based on results of the current study and those previously reported in the literature.

5.1 Conclusions

A range of PAN-g-PDMS copolymers were synthesised employing conventional free radical copolymerization of acrylonitrile monomer and PDMS macromonomers. PDMS macromonomers of three molecular weights were used: 1000 g.mol^{-1}, 5000 g.mol^{-1}, and 10 000 g.mol^{-1}. Size-exclusion chromatography showed no trend in either molar mass or molar mass dispersity of the synthesised copolymers. This is to be expected of polymers synthesised by conventional free radical polymerization methods. ^{1}H NMR spectroscopic analysis proved that the incorporation of PDMS macromonomer is lower than the amount in the feed and that incorporation is more efficient the lower the molecular weight of the macromonomer. A clear trend was seen as a plot of incorporation w.r.t. feed ratio produced a very good linear fit. The slope of the linear trendline is 0.956 for the 1000 g.mol^{-1} PDMS macromonomers, 0.571 for the 5000 g.mol^{-1} PDMS macromonomers and 0.383 for the 10 000 g.mol^{-1} PDMS macromonomers due to the lower incorporation of higher molecular weight PDMS macromonomers.

Electrospinning of the copolymers was done at three TCD's: 20 cm, 25 cm and 30 cm. Interpretation of fiber diameter results was not trivial. No trends were seen w.r.t. PDMS graft content. Some fiber diameter data could, however, be explained by considering both the PDMS graft content and the molar mass of the constituent copolymer. The effects of electrospinning solution ageing was studied. SEM images show an initial increase in surface roughness of the electrospun nanofibers up to 18 h after which a gradual smoothening of the surface ensued. Fiber diameter analysis showed a strong dependence on ambient conditions. The observed independence of the fiber surface morphology on ambient conditions suggests that the process of self-assembly is not strongly dependent on an immediate change in the environment.

All electrospun nanofiber precursors consisting of PAN-g-PDMS copolymers have roughly textured surfaces as observed by SEM imaging. Carbonisation of the fiber membranes produced black fibrous membranes consisting of nanofibers with more smoothed surfaces.

Co-precipitation of iron oxide nanoparticles and subsequent silica coating following a modified version of the Stöber method were employed to obtain silica-coated iron oxide nanoparticles. It was found that the amount of TEOS silicating agent used dictates whether multi-core or single-core nanoparticles are formed. Whether the concentration of IONPs in the reaction mixture plays a role in forming either multi- or single-core nanoparticles is not clear from the current results. TGA showed a mass loss of 17 % for the single-core nanoparticles when heated to 800 °C. No immediate increase in mass was seen after switching to an oxygen atmosphere directly after the cooling stage. ATR-FTIR analysis proved that thermal treatment in an inert atmosphere at 800 °C for 2 h was effective

in removing residual solvent still present after drying in vacuo. Zeta potential measurements in water showed that the synthesised multi-core, single-core and thermally treated single-core nanoparticles have surface charges of -30.7 mV, -25.2 mV and -25.7 mV respectively. Strongly negative zeta potentials are to be expected of silica-coated IONPs.[1] DLS size measurements showed signs of particle agglomeration in water at the concentration used for electrospinning, though the DLS experiments were not repeated in DMF (spinning solvent).

Electrospun precursor polymer nanofiber-nanoparticle composites revealed severe agglomeration of the multi-core nanoparticles. Single-core nanoparticles as well as thermally treated single-core nanoparticles, having much smaller particle diameters than that of the multi-core nanoparticles, showed good dispersion inside the electrospun nanofibers.

Carbonisation of composites containing multi-core nanoparticles produced black fiber membranes for PAN homopolymer precursors as well as all PAN-g-PDMS copolymer precursors. TEM imaging revealed that nanoparticles are still present mainly in the form of agglomerates as in the case of the precursor composites. Fiber breakage was observed around nanoparticle agglomerates that could lead to the loss of nanoparticles from the carbon nanofiber membrane and weakening of the carbon fiber membrane. Carbonisation of composites containing single-core nanoparticle did not produce a fibrous membrane but instead a black powder residue. STEM imaging revealed very little intact fiber sections and a large amount of nanoparticles isolated from the fragmented fiber sections. Intact fiber sections showed voids surrounding incorporated nanoparticles in the fiber material. These voids were formed due to the release of oxygen from the iron oxide cores during carbonisation. Carbonised composites containing thermally treated single-core nanoparticles produced black nanofiber membranes for fiber-particle precursors consisting of PAN homopolymer, PAN-g-PDMS copolymers as well as PAN-g-PDMS copolymer precursors electrospun after 18 h of solution ageing. No voids could be seen as in the case of untreated single-core nanoparticles.

The results of this study indicate that it is possible to produce porous magnetic carbon nanofibers using PAN-g-PDMS copolymer precursor materials, but in order to ensure the fibers remain intact during carbonization, it is necessary to include the silica-coated IONPs only after thermal treatment.

Sorption studies of the carbon nanofiber-nanoparticle composite membrane prepared using PAN-g-PDMS copolymer fiber-particle nanocomposite precursors and thermally treated single-core nanoparticles electrospun after 18 h of solution ageing showed a higher sorption capacity towards water than towards hexane and silicon oil. This is in stark contrast to literature results on carbon fiber materials.[2,3] ATR-FTIR spectroscopy revealed an absorption peak associated with silica for both the carbon nanocomposite and the carbon fiber membrane without nanoparticles. Clearly, PDMS

sections in the constituent copolymers decompose to form silica. This explains the hydrophilic nature of the membrane as opposed to the very hydrophobic nature of carbon nanofibers.

5.2 Recommendations for future work

Kinetic aspects of the electrospinning solution ageing of PAN-g-PDMS copolymers is not yet fully understood. The reasoning behind the solution ageing is to increase the porous surface morphology and thereby enhance the total surface area. Time-dependence of an increase in the surface area is an important parameter that must be optimized in order to fully utilize the effects of solution ageing. This can be done by nitrogen surface area analysis to determine the surface area of the resultant nanofibers as a function of electrospinning solution ageing time. Human has already proven that the surface area of carbon nanofibers produced by carbonisation of PAN-g-PDMS copolymer precursor nanofibers have a non-linear dependence on the PDMS graft content.[2]

The effect of thermal treatment on the magnetization of the silica-coated IONPs is of importance. SQUID magnetometry could be used to quantify the loss of magnetization of the nanoparticles due to the thermal treatment and the process of carbonisation.

Nanoparticle dispersion has been a crucial element of the current study. To understand the dispersion of nanoparticles during electrospinning of PAN-based nanofibers, an extensive study is required employing methods that produce nanoparticles of controllable size in order to thoroughly investigate the effect of particle size on the dispersion or agglomeration in the composites. Ideally, such a study should include the use of both silica nanoparticles and silica-coated IONPs to determine whether or not the magnetic cores have an effect on the dispersion of the nanoparticles. A critical particle size might exist above which severe agglomeration takes place. Particle concentration will most likely affect such a critical particle size.

More streamlined methods have been reported to induce magnetization in carbon nanofibers by electrospinning of PAN homopolymer solutions containing iron precursors that, upon carbonization, produce well-dispersed IONPs incorporated into the carbon matrix.[3,4] This procedure entirely circumvents the challenges related to dispersion of the IONPs in the precursor nanofibers as well as those related to oxidation of the carbon matrix surrounding the nanoparticles. The use of porous nanofibers consisting of PAN-g-PDMS copolymers containing such iron precursors will most likely lead to porous magnetic carbon nanofibers produced by a method which is faster and simpler than that currently employed.

References

1. Bumb, A. *et al.* Synthesis and characterization of ultra-small superparamagnetic iron oxide nanoparticles thinly coated with silica. *Nanotechnology* **19**, 335601 (2008).

2. Human, C. Facile method for producing silicon containing porous carbon nanofibres from amphiphilic copolymers and controlling precursor fibre morphology, MSc Thesis. (Stellenbosch University, 2015).

3. Tai, M. H., Tan, B. Y. L., Juay, J., Sun, D. D. & Leckie, J. O. A Self-Assembled Superhydrophobic Electrospun Carbon-Silica Nanofiber Sponge for Selective Removal and Recovery of Oils and Organic Solvents. *Chem. - A Eur. J.* **21**, 5395–5402 (2015).

4. Panels, J. E. *et al.* Synthesis and characterization of magnetically active carbon nanofiber/iron oxide composites with hierarchical pore structures. *Nanotechnology* **19**, 455612 (2008).

Appendix A

Figure A.1 shows an overlay of ^{1}H NMR spectra of copolymers synthesized using 20 wt.% of the respective PDMS macromonomers.

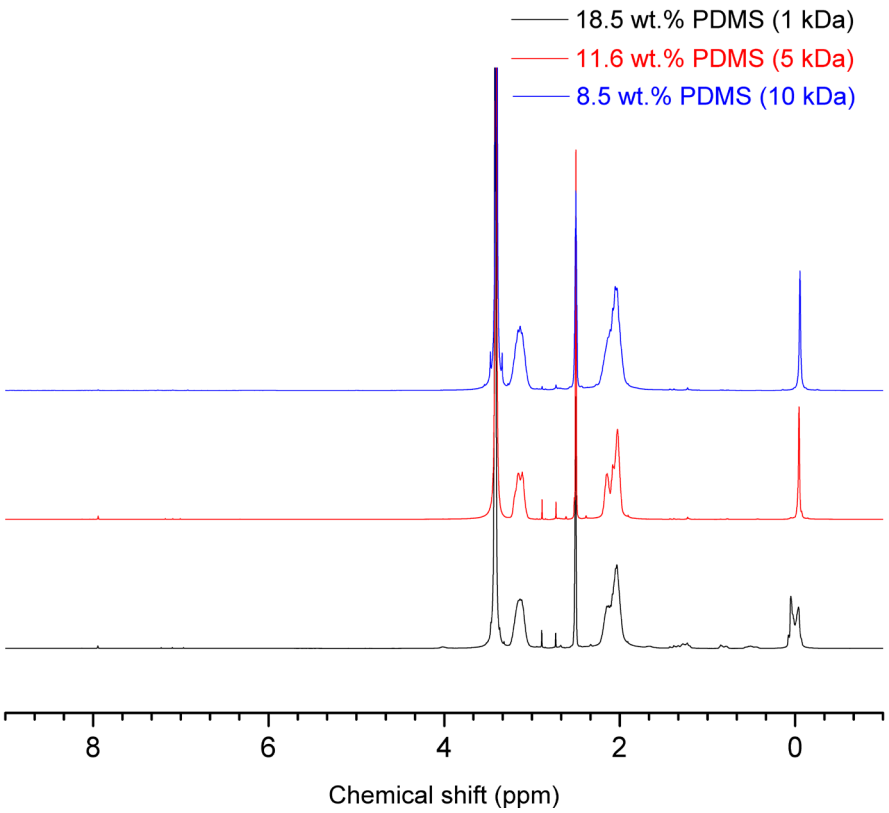

Figure A.1: ^{1}H NMR spectra of PAN-g-PDMS copolymers synthesized using 20 wt.% of 1 kDa, 5 kDa 10 kDa PDMS macromonomers

Appendix B

The peak maxima and corrected exotherm enthalpy w.r.t. 5 kDa PDMS graft content for the powders and electrospun fibers of copolymers synthesized using 0.15 wt.% AIBN is shown in *Figure B.1*.

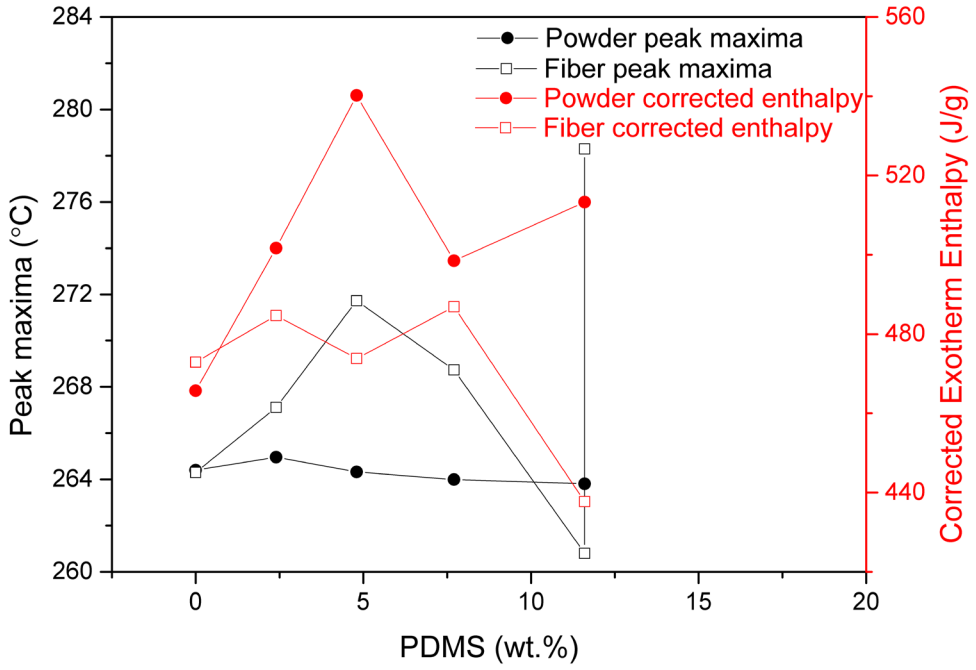

Figure B.1: Peak maxima (black) and corrected exothermic enthalpy (red) w.r.t. PDMS graft content of powders (solid dots) and electrospun nanofibers (open squares) consisting of copolymers containing 5 kDa PDMS grafts synthesized using 0.15 wt.% AIBN

The peak maxima and corrected exotherm enthalpy w.r.t. 5 kDa PDMS graft content for the powders and electrospun fibers of copolymers synthesized using 0.20 wt.% AIBN is shown in *Figure B.2*.

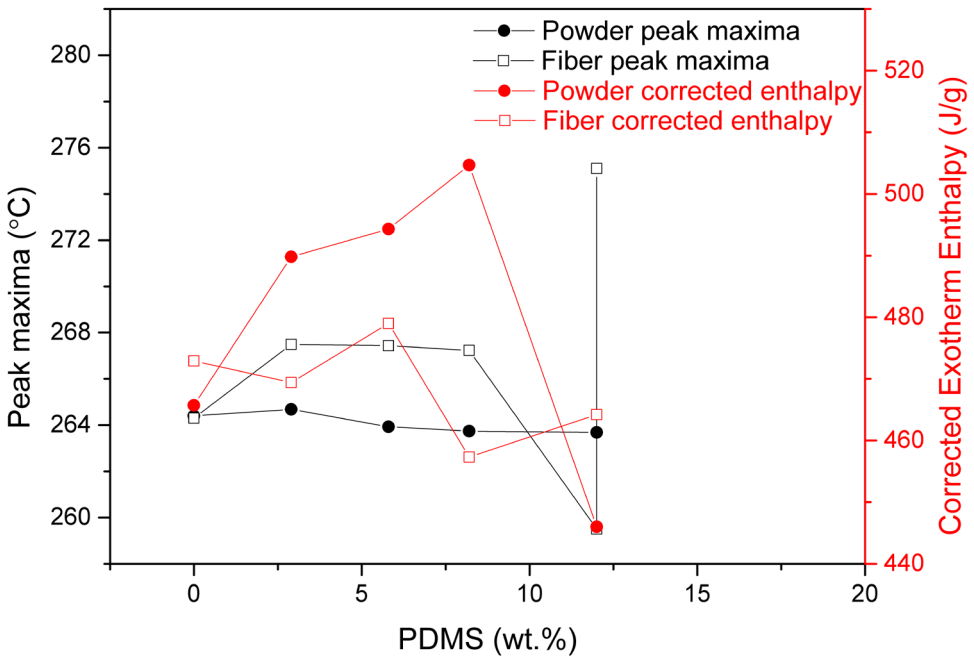

Figure B.2: Peak maxima (black) and corrected exothermic enthalpy (red) w.r.t. PDMS graft content of powders (solid dots) and electrospun nanofibers (open squares) consisting of copolymers containing 5 kDa PDMS grafts synthesized using 0.20 wt.% AIBN

Table B.1 shows the DSC peak maximum, exotherm enthalpy and corrected exotherm enthalpy for thermograms of 5 kDa PDMS graft copolymers synthesised using 0.15 wt.% AIBN.

Table B.1:

DSC peak maximum, exotherm enthalpy and corrected exotherm enthalpy for thermograms of 5 kDa PDMS graft copolymers

	PDMS (wt.%)	Peak maximum (°C)		Exotherm enthalpy (J.g)	Corrected exotherm enthalpy (J/g)
		T_{m1}	T_{m2}		
Powders	0	264.4		465.7	465.7
	2.4	265.0		489.7	501.7
	4.8	264.3		514.3	540.2
	7.7	264.0		460.1	498.5
	11.6	263.8		453.8	513.3
Fibers	0	268.5		463.1	474.5
	2.4	267.1		473.1	484.7
	4.8	271.7	261.8	451.1	473.8
	7.7	268.7	260.3	449.4	486.9
	11.6	260.8	278.3	386.9	437.7

Table B.2 shows the DSC peak maximum, exotherm enthalpy and corrected exotherm enthalpy for thermograms of 5 kDa PDMS graft copolymers synthesised using 0.20 wt.% AIBN.

Table B.2:

DSC peak maximum, exotherm enthalpy and corrected exotherm enthalpy for thermograms of 5 kDa PDMS graft copolymers

	PDMS (wt.%)	Peak maximum (°C)		Exotherm enthalpy (J.g)	Corrected exotherm enthalpy (J/g)
		T_{m1}	T_{m2}		
Powders	0	264.4		465.7	465.7
	2.9	264.7		475.6	489.8
	5.8	264.0		465.6	494.3
	8.2	263.7		463.3	504.7
	12.0	263.7		392.5	446.0
Fibers	0	268.5		463.1	474.5
	2.9	267.5		455.8	469.4
	5.8	267.4		451.2	479.0
	8.2	267.2	258.8	419.8	457.3
	12.0	259.5	275.1	408.5	464.2

Appendix C

ATR-FTIR spectra of pure polymer nanofibers

ATR-FTIR spectra of the electrospun nanofibers are shown in *Figure B.1*.

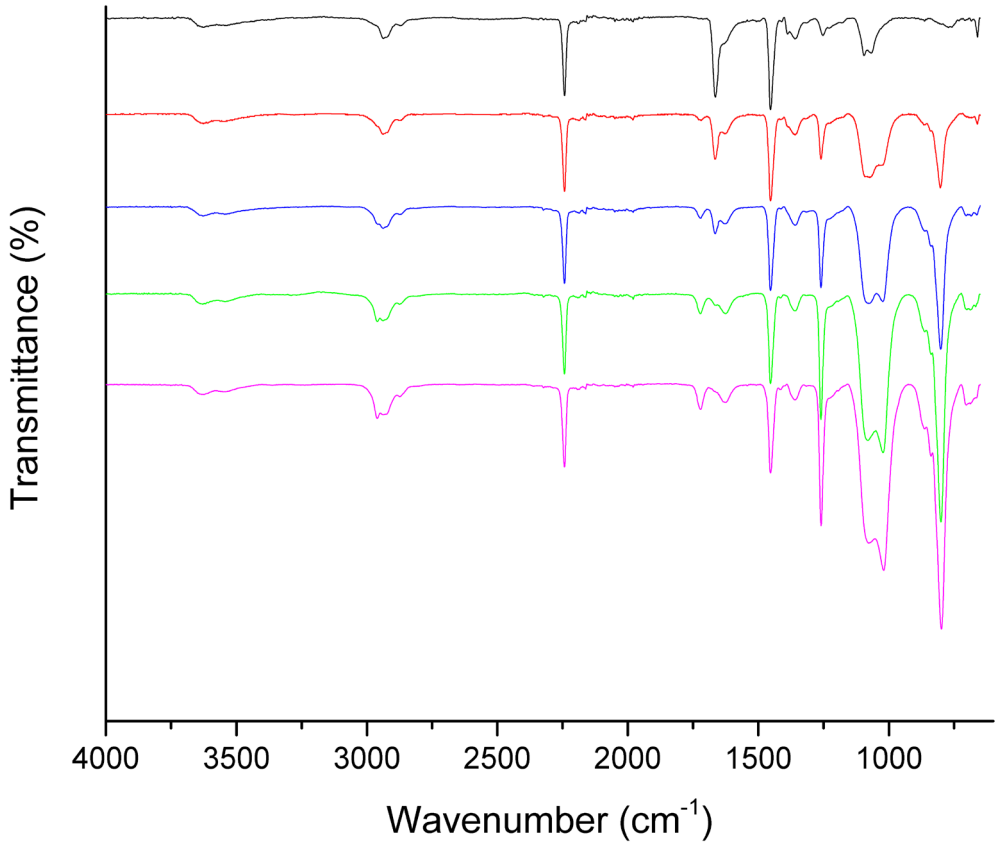

Figure C.1: ATR-FTIR spectra of electrospun nanofibers consisting of PAN homopolymer (black) and PAN-g-PDMS copolymer containing b) 3.7 wt.%, c) 8.4 wt.%, d) 13.5 wt.% and e) 18.5 wt.% PDMS grafts

The PAN sections of the copolymers lead to absorptions in all the spectra. The peak at 2250 cm^{-1} is ascribed to C-N stretch of the nitrile group on the PAN polymer sections.[1,3] A CH_2 bend absorption can be seen at 1460 cm^{-1} .[3] This originates in methylene groups on the polymer backbone. The peaks at 2870 – 2970 cm^{-1} correspond to sp^3 C-H stretch vibrations.[3] The absence of peaks in the region 3000 – 3100 cm^{-1}, corresponding to sp^2 C-H stretch vibrations, suggest that no unreacted monomer is present.[3]

The PDMS grafts consists of a PDMS chain, an aliphatic chain-end and a MMA-type insertion group that links the graft to the polymer backbone. The aliphatic group contributes to the CH_2 bend absorption at 1460 cm^{-1} and the CH_3 bend absorption at 1360 cm^{-1} from methylene and methyl groups respectively.[3] Peaks are seen at 1260 cm^{-1} and 800 cm^{-1} that correspond to Si-CH_3 absorptions of the PDMS chains.[29,30] Two overlapping peaks are visible at 1090 cm^{-1} and 1025 cm^{-1} corresponding to Si-O-Si stretches in PDMS.[30] A small peak appears at 1730 cm^{-1} that corresponds to the C-O double bond stretch originating in the MMA-type insertion group of the PDMS grafts and

residual DMF solvent.[3] The intensity of the peaks at 1730 cm^{-1}, 1260 cm^{-1}, 800 cm^{-1}, 1090 cm^{-1} and 1025 cm^{-1} are clearly seen to increase with an increase in PDMS content. The C-O stretch from the ester group in the MMA-type insertion group is believed to appear as a shoulder at the lower wavenumber region of the 1260 cm^{-1}.[3]

Residual DMF will appear in the FTIR spectrum.

Amide group C-O peaks can be seen at 1660 cm^{-1} .[3] DMF methyl groups are believed to contribute to the peak at 1360 cm^{-1} along with the CH_3 groups of the PDMS grafts. The C-N amide stretch, expected around 1400 cm^{-1} is not visible presumably due to overlap with either the CH_2 bend absorption at 1460 cm^{-1} or the CH_3 bend absorption at 1360 cm^{-1} .[3]

ATR-FTIR of nanofiber-nanoparticle (multi-core) composites

ATR-FTIR spectra of the precursor nanofiber-nanoparticle composites are shown in *Figure B.2*.

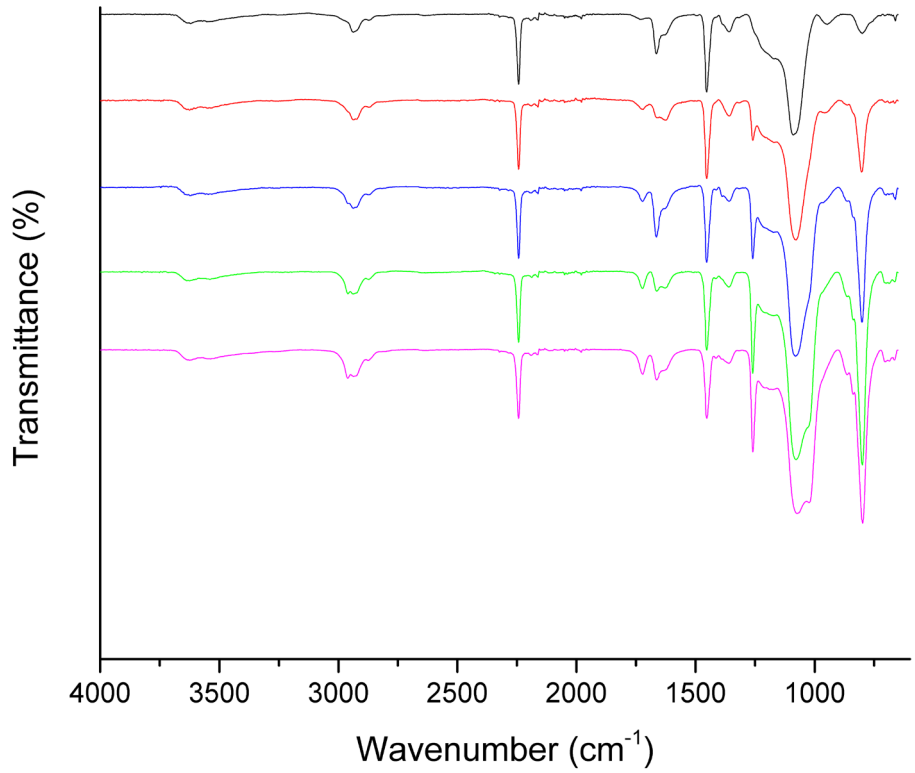

Figure C.2: FTIR spectra of precursor nanofibers-nanoparticle composites consisting of a) PAN homopolymer and PAN-g-PDMS copolymers containing c) 3.7 wt.%, d) 8.4 wt.%, e) 13.5 wt.% and f) 18.5 wt.% PDMS grafts and 10 wt.% silica-coated multi-core iron oxide nanoparticles

Though there are several peaks corresponding to silica that are expected to appear in the spectra of the nanocomposites, severe overlap with PDMS absorptions obscure the visibility of many of these peaks. Nevertheless a peak at 1080 cm^{-1} corresponding to a Si-O-Si stretch absorption is visible in the homopolymer fiber-particle nanocomposites and changes the shape of the peaks of the copolymer fiber-particle nanocomposites compared to that of the pure polymer nanofibers.[20] This

peak is not seen in the pure polymer nanofibers. It has been observed previously in silica-coated IONPs.[20] A small peak can be seen at 960 cm^{-1} in the spectra of the homopolymer-nanoparticle composites which is believed to originate from a Si-OH stretch previously reported in silica nanoparticles.[23] This was not observed in the spectra of the pure polymer nanofibers. The peak at 960 cm^{-1} is, however, immersed in the Si-O-Si PDMS stretch absorption peak at 1025 cm^{-1} in the copolymer nanofiber-nanoparticle composites. A Si-O stretch absorption associated with silica is observed at 800 cm^{-1} in the homopolymer nanofiber-nanoparticle composites.[22] This absorption is obscured in the copolymer composites by the Si-CH_3 absorption of the PDMS graft chains at the same wavenumber. The peak at broad absorption peak centered around 3550 cm^{-1} corresponds to O-H stretch vibrations while the peak at 1630 cm^{-1} corresponds to H-O-H bend vibrations of adsorbed water.[22,32] This might be due to water vapour absorbed during electrospinning due to the miscibility of DMF and water, due to water adsorbed in the nanoparticles or a combination thereof. Comparison of these ATR-FTIR spectra with those of the pure polymer nanofibers shown in *Figure 4.10* proves that the silica-coated IONPs were incorporated into the precursor nanofibers.